Pulse Shape Analysis for Heavy Element Spectroscopy

M. Sc. Thesis

Ulrika Forsberg
Division of Nuclear Physics
Department of Physics, Lund University

November 2010

Supervisors: Dirk Rudolph and Pavel Golubev

Abstract

This thesis describes the investigation of whether a new type of ADCs - sampling ADCs - can be used to improve the experimental setup TASISpec, which contains an array of silicon strip detectors and germanium detectors. TASISpec aims at spectroscopic studies of super-heavy elements. The performance of sampling ADCs was tested by passively splitting the detector signals from the double-sided silicon strip detector of the setup into one branch with conventional electronics and one branch with sampling ADCs. The data was recorded using both a 3-line α source and an in-beam experiment in which ^{253}No was implanted into the detector. The 100 MHz sampling ADCs allow for a recording of the actual form of the pulse from the preamplifier. For each event, the digitised pulse from a time window of 2.56 μs was read out. The recorded traces were analysed with respect to height, arrival time, rise time and slope of the rise. The energy resolution of the sampling ADCs was tested by applying various algorithms to the data, and the resolution was found to be equally good as from the standard electronics. The resolution may be improved further by considering a longer fraction of the pulse than was recorded in this experiment. The possibilities of particle identification from the shapes of the pulses were investigated, and a method based on integration of different parts of the derivative of the pulse gave results that imply that particle information is available in the pulses and that identification might be possible.

Contents

List of Abbreviations

SHE	Super-Heavy Elements
DSSSD	Double Sided Silicon Strip Detector
SSSSD	Single Sided Silicon Strip Detector
TASCA	TransActinide Separator and Chemistry Apparatus
GSI	Gesellschaft für Schwerionenforschung
FPGA	Field Programmable Gate Array
HPGe	High Purity Germanium
LINAC	LINear ACcelerator
TDC	Time-to-Digital Converter
ADC	Analog-to-Digital Converter
NIM	Nuclear Instrument Module
VME	A computer hardware bus standard

Acknowledgments

I would like to thank my supervisors Dirk and Pavel for allowing me to work with their fascinating creation TASISpec in so many different ways; not only in detector laboratory at the university, but also "in action" at GSI during several different experiments. Thank you for allowing me to come with you to GSI, for good discussions and for all your help. My gratefulness also goes to all the people at GSI, and from collaborating universities, who participated in making the experiments very inspiring experiences.

I would also like to thank all the people at the Nuclear Physics Department for the great hospitality that has made me feel very welcome. Special thoughts go to Maria, Maciek, Pico, and Robert, who have made the time at the department, and outside it, very enjoyable. Additional thanks go to Pico for the help with programming and for being such a good office mate.

Finally, I would like to thank Daniel for always helping me out and supporting me whenever I need it the most.

Chapter 1

Introduction

The production and study of super-heavy elements (SHE) is one of the most interesting and challenging topics in nuclear structure research today. The term SHE usually refers to nuclei that are heavier than the actinides, which implies proton numbers Z $\geq$ 104. SHE do not, as far as one knows, occur naturally on Earth. The periodic table of chemical elements is shown in Figure 1.1. Elements present on Earth comprise up to $Z = 92$ (uranium). Heavier, artificially produced elements reach up to $Z = 118$ according to [1] are also displayed.

Studies of nuclei have led to theoretical models of how nucleons interact in order to form nuclei. No single theory can explain all the known features of nuclei, and several different sets of parameters for the various theoretical models have been suggested to give the best explanation of the experimental data available. However, many of the theories indicate that there will be nuclei with considerably enhanced stability at proton numbers somewhere in the region of $Z = 114$-120 and neutron numbers of $N = 184$, compared to those nuclei that are somewhat lighter. This is due to the shell structure that arises from the non-equidistant energy levels of the nucleons bound by the nuclear potential. Not only would it be a fascinating discovery to find that there are SHE that are long-lived, which may open up for still unknown fields of research, but it would also yield important data to test and refine the current models of nuclei.

During the last years, SHE research has made great advances. Several new super-heavy elements have been discovered recently at GSI, Darmstadt, Germany ($Z = 107$-112), RIKEN, Japan ($Z = 113$) and at FNLR, Dubna, Russia ($Z = 114$-118). The heaviest element that has been claimed so far has $Z = 118$ [1]. The last time a new element was claimed was in April 2010, when the likely discovery of element 117 was published [2].

The successful production of SHE needs to be followed by a characterisation of the properties of the nuclei, e.g. ground state spin and parity, decay schemes and characteristic X-rays. For this purpose, several setups have been created. Some setups are designed for in-beam spectroscopy where the detection of relevant particles take place at to the production site, and some are designed to be placed after the products have been separated according to, for instance, mass-to-charge ratio A/q, after which they detect the subsequent decay of the nuclei [3]. At FLNR, the detector system GABRIELA [4] has been developed for measuring the decays of heavy elements at the focal plane of a vacuum recoil separator. The GREAT spectrometer [5] is another detector array constructed

1												13	14	15	16	17	18
1 H	2																2 He
3 Li	4 Be											5 B	6 C	7 N	8 O	9 F	10 Ne
11 Na	12 Mg	3	4	5	6	7	8	9	10	11	12	13 Al	14 Si	15 P	16 S	17 Cl	18 Ar
19 K	20 Ca	21 Sc	22 Ti	23 V	24 Cr	25 Mn	26 Fe	27 Co	28 Ni	29 Cu	30 Zn	31 Ga	32 Ge	33 As	34 Se	35 Br	36 Kr
37 Rb	38 Sr	39 Y	40 Zr	41 Nb	42 Mo	43 Tc	44 Ru	45 Rh	46 Pd	47 Ag	48 Cd	49 In	50 Sn	51 Sb	52 Te	53 I	54 Xe
55 Cs	56 Ba	57-* La	72 Hf	73 Ta	74 W	75 Re	76 Os	77 Ir	78 Pt	79 Au	80 Hg	81 Tl	82 Pb	83 Bi	84 Po	85 At	86 Rn
87 Fr	88 Ra	89-" Ac	104 Rf	105 Db	106 Sg	107 Bh	108 Hs	109 Mt	110 Ds	111 Rg	112 Cn	113 ---	114 ---	115 ---	116 ---	117 ---	118 ---

*	58 Ce	59 Pr	60 Nd	61 Pm	62 Sm	63 Eu	64 Gd	65 Tb	66 Dy	67 Ho	68 Er	69 Tm	70 Yb	71 Lu
"	90 Th	91 Pa	92 U	93 Np	94 Pu	95 Am	96 Cm	97 Bk	98 Cf	99 Es	100 Fm	101 Md	102 No	103 Lr

Figure 1.1: *The periodic table of elements. The actinides are shown in the last row, marked with a ".*

for the focal plane of the RITU separator at JYFL, Jyväskylä, Finland. This detector array is not primarily aimed at decay spectroscopy but acts as a tagger for in-beam spectroscopy, meaning that coincidences between an identification of a SHE in the focal plane of the separator can be correlated to radiation detected at the production site.

A newly built array of detectors for studying the decays of SHE is TASISpec (Tasca Small Image mode Spectroscopy), which is first and foremost designed to be used at the focal plane of TASCA (TransActinide Separator and Chemistry Apparatus) at GSI. The heavy ions to be studied are produced in fusion-evaporation reactions between a beam of ions that collide with a target consisting of heavy atoms. The ions of interest are separated from the rest of the collision products in the gas-filled recoil separator TASCA, and the particles are focused into the detector setup.

Due to the unique "Small Image Mode" of TASCA, the ions are focused into a rather small spot, only about 3 cm in diameter, onto a double-sided silicon strip detector (DSSSD) divided into 32 strips on each side. The ions are implanted into the p-side of the detector with energies of tens of MeV resulting in implantation depths of a few micrometers. Subsequently emitted α or β particles, very low energy γ-rays, conversion electrons, and fission fragments can be detected in the DSSSD in case of decay products moving into the detector. Electromagnetic radiation, γ rays of X-rays, with energies in excess of some 30 keV are detected in surrounding germanium detectors. In order to get a higher efficiency for particle detection, there are four single-sided silicons strip detectors placed like the sides of a box upstream of the DSSSD. The TASISpec setup is shown in Figure 1.2.

The readout of the silicon detectors is done using a conventional chain of analog electronics; preamplifiers are followed by shaping amplifiers, and energy

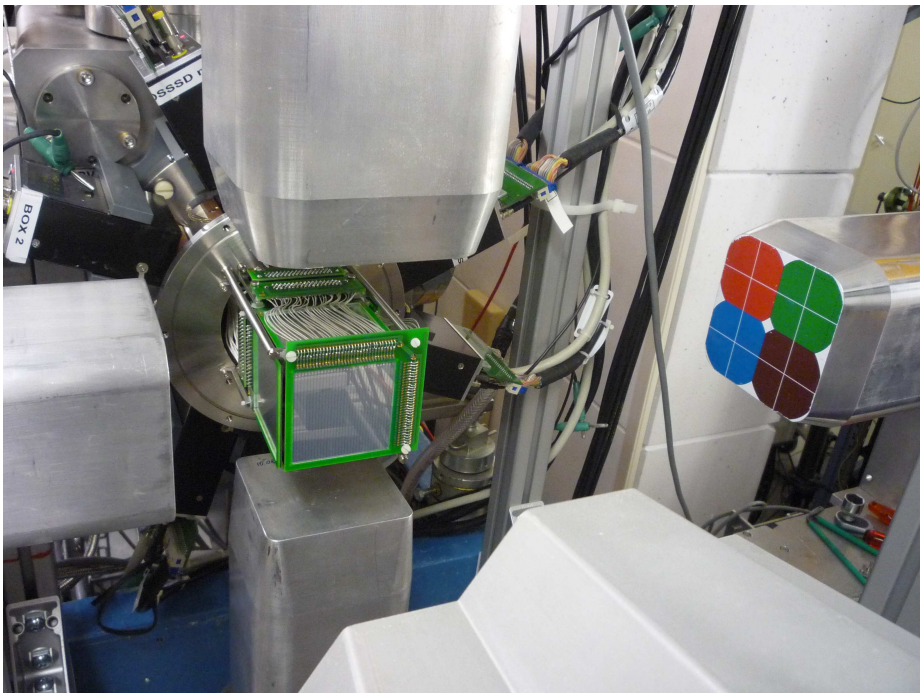

Figure 1.2: *The TASISpec setup: The ions enter the "box" of silicon detectors seen in the left part of the figure. The DSSSD is the detector that is facing the camera, and the other two detectors that are seen to form the sides of a box upstream of the DSSSD are SSSSDs. During normal operation, there is a cap that covers the silicon detectors. The three detectors on the left, top and bottom of the silicon detectors are germanium detectors of CLOVER type. The coloured detector to the right shows how the four Ge crystals are arranged inside a CLOVER detector. The lower part of the photo shows the CLUSTER germanium detector, which contains 7 crystals. This detector is placed behind the DSSSD.*

and timing signals are digitised by ADCs and TDCs, respectively. With the newly developed sampling ADCs, which can digitise samples from the incoming signal with typical rates on the order of 50-100 MHz, it is possible to access the actual shape of the pulse from the preamplifiers connected to silicon-strip-detectors. The use of sampling ADCs could give a more compact readout-system, as shaping of the pulses becomes superfluous, and as both time and energy can be extracted using the same module. The use of sampling ADCs also opens up for many new exciting possibilities. The energy and time resolution of the data may be improved with the use of specific software algorithms for treatment of the pulses from the detectors, and accessing the whole pulse allows for the determination of more parameters than just height and time of a pulse. For example, additional information from the pulse shapes can be relevant for separation of different types of events. In the case of TASISpec, it would be of special interest to be able to distinguish implanted ions from particles from their subsequent decays.

For the TASISpec setup, the use of sampling ADCs is useful primarily for the read-out of the DSSSD. As this detector is subject to both implantations of heavy ions and α-decays, both of which may be in the same energy regime for certain reactions, it would be very useful to be able to separate the particles according to type. Since the ionisation tracks of α particles and heavy ions in silicon are different, it seems likely that it should affect the charge collection inside the detector and hence produce different pulse shapes. The aim of this work is to investigate the possibilities of using sampling ADCs in the TASISpec setup, and the possible benefits from this.

The first step towards the use of sampling ADCs for the TASISpec setup is to establish their function in comparison to standard electronics. The energy information that is extracted from the new modules should have equal, or better, resolution compared to conventional electronics, and the timing information should be of the same quality. Next, the new information from the pulse shapes should be investigated with respect to particle identification.

For this purpose, an experiment was performed with TASISpec in which the output of the preamplifiers from parts of the DSSSD was split into two different electronics chains - one was processed by conventional electronics and the other was fed into sampling ADCs which digitise the pulse shape. An α source was used for irradiation of the detector, in order to get a straight-forward comparison of the two different chains. To allow for testing of the possible particle identification, an experiment utilising an ion beam was performed.

In a real experiment, it may not be possible to separate α decays from implanted ions, scattered beam or target-like particles by means of energy, and in those cases it would be useful to have a different approach to the particle identification. With such an identification process, it would be possible to access also the information that is hidden by the large background that is created during the time of the experiment that the beam is irradiating the target. Currently, this data, which accounts for 25% of the total time at the UNILAC at GSI, cannot be properly accessed.

Sampling ADCs are used today in several experimental setups. For readout of germanium detectors, it is common to use sampling ADCs. For these purposes, algorithms for extraction of the time and energy have been developed and are integrated parts of the sampling ADCs. Used in this way, the main benefits are a more compact readout system and the resolution that can be

achieved. Previous attempts to use pulse shape techniques to discriminate between different particles have been made for different experimental setups. One such experiment is reported in [6], where pulse shape discrimination in silicon detectors is applied in order to determine the type of particle. In this investigation, analog electronics was used. This seems to be the case for several similar investigations that are done in this field even today (see e.g. [7]). These investigations show that indeed there is information in the pulses from silicon detectors that can, in principle, be used for particle discrimination. However, there are limitations to the process. It was shown in [8] that for the silicon detectors available for their investigation, the non-homogeneity of the silicon crystals imposed serious problems for the particle identification. For the TASISpec setup, such problems may be possible to overcome, because of the pixellation of the DSSSD in conjunction with the use of sampling ADCs, as the pixels can then be treated individually.

The best side to irradiate the crystals from has been shown to be the n-side, which imposes boundaries on the energy in the sense that the energy of the incoming particles cannot be too low, because they have to pass through the dead layer, which is thicker for the n-side than for the p-side. For the TASISpec setup it is necessary to irradiate the detector from the p-side, which can make the particle identification an even more intricate task.

Chapter 2 of this report describes some of the technical aspects of DSSSDs and sampling ADCs, as well as techniques for digital processing of pulses. Chapter 3 contains the experimental setup used for the investigation, and chapter 4 is a comparison of the two electronic setups with respect to the extraction of energy information. Chapter 5 describes the development of procedures for extracting parameters from the rise of the pulse, and the application of these to investigate the possibilities of particle separation. Chapter 6 presents a summary and an outlook.

Chapter 2

Technical Details

2.1 Double Sided Silicon Strip Detectors

2.1.1 Principles of operation

DSSSD detectors are semiconductor devices, in which free charge carriers are produced when the material is subject to radiation. They consist of one p-doped and one n-doped semiconductor part, over which an electric field is applied. When radiation passes the device, free holes and electrons are created and collected by the applied voltage, thus giving a signal that is proportional to the energy deposited into the detector.

Figure 2.1 shows a schematic picture of a semiconductor detector. A so-called pn-junction is formed between two materials with different doping - one side contains impurities mainly of atoms that have five electrons (n-doping) as compared to the semiconductors which are tetravalent. The other side is doped with atoms with three valence electrons. The crystalline structure of pure silicon enables each atom to form covalent bonds with its four nearest neighbours. When an impurity atom with more than four electrons is present, the excess electron is only very loosely bound to its nucleus, as the surrounding structure allows for the impurity atom to participate in four covalent bonds leaving the last electron unnecessary for the formation of the crystal. When an impurity with fewer electrons are present in the crystal, an electron "hole" is created, as the lack of electrons disables saturation of the bonds. The hole is bound to the corresponding impurity due to the non-uniform electric field that is created by the impurity, but only loosely. The excess electrons and the holes are the most important charge carriers in semiconductors.

When a pn-junction is formed, the excess electrons and the holes migrate over the junction. The electrons that were unnecessary for the bonding on the n-side move over to the p-side, where they saturate the covalent bonds. This forms a so-called depletion region, in which there are no free charge carries, neither electrons nor holes; they are all part of covalent bondings. However, this process also makes the material charged, as the p-side will have more electrons than positive charges, and the n-side will have fewer electrons than the corresponding charge of the ions in the material. This electric field stops the net process of electron and hole migration leading to a distinct depletion area. It is this area that is used for detection - when ionising radiation enters this area, the bonds

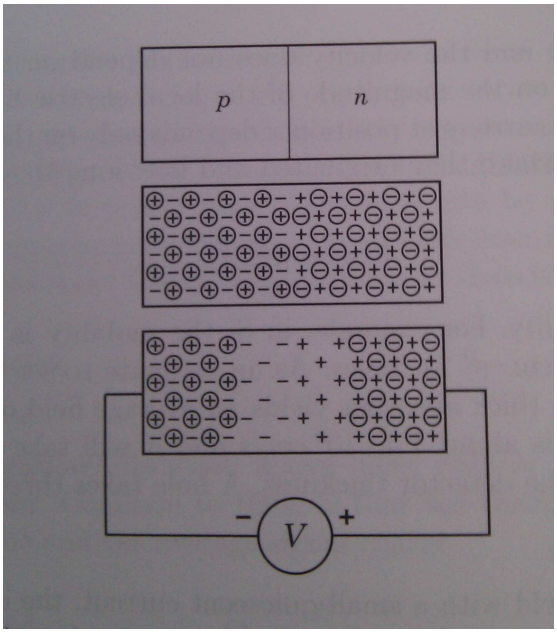

Figure 2.1: *The principle of a semiconductor detector. The detector consists on one p-doped and one n-doped material, as shown in the upper part of the figure. The n-side contains electrons that are almost free, shown in the middle and lower figure as minus signs in circles. The p-side contains free holes, shown as plus signs in circles. The plus signs and minus signs that are not encircled are the doping atoms, which are fixed to the lattice. The lower figure shows the effect of an external, reverse bias: The depletion region is extended. Figure from [9].*

are broken. The electrons, and the holes that they leave behind, are the free charge carriers that indicate the presence of radiation.

The charge carriers are collected by an externally applied voltage. This is done with reverse bias, meaning that the p-side has a lower potential than the n-side. If the potential had been added in the opposite direction, the pn-junction would become a conductor, but with reverse bias, the resistivity is high. Only when radiation enters the depletion region and creates free electrons and holes, the pn-junction can conduct current. This is how radiation is detected; whenever radiation causes free charge carriers, a current flows through it.

Adding an external voltage also increases the width of the depletion region further, as electrons are attracted from the n-side and holes from the p-side by the external voltage. The number of free charge carriers decrease on both sides as illustrated in the lower part of Figure 2.1.

Semiconductor detectors can be fabricated in different materials and in different shapes and configurations. The detectors that are relevant for this work, are silicon strip detectors. These are thin detectors, often less than 1 mm, that are segmented into narrow strips. The pn-junction itself is not separated into different parts, but the detector is biased in a way that makes the energy deposited in a strip of the detector being collected by a corresponding electrode. In case of DSSSDs, the electric fields are constructed such that a separation in both x- and y-direction is possible. On one side, the strips are oriented in one direction, and one the other side the strips are in the other direction. This gives a pixellation of the detector which allows for a 2D positioning of incoming radiation.

An important feature of semiconductor detectors is the dead layer, which consists of the non-depleted part of the detector together with metalization and oxide layers, and regions of highly doped silicon. This is important to take into account, since the energy that is deposited in the dead layer does not take part in the formation of the pulse. Therefore, the detected energy needs to be compensated for this in order to achieve the true value of the energy.

2.1.2 Formation of pulses

The electrons and holes are separated into free charge carriers when radiation enters a semiconductor detector. With time, they recombine unless they are extracted from the detector. The electric field that is applied over the detector causes the holes to drift towards the p-side of the detector, and the electrons to drift towards the n-side. This charge is collected on electrodes, which are connected to charge-sensitive preamplifiers.

The charge carriers drift through the silicon at a velocity of about 10^7 mm/s in a detector over which an electric field is applied with sufficient strength in order to give a saturation of the velocity [10]. If energy is deposited close to one side of the detector, the drift time is different for the different sides. The drift time is usually referred to as the *transient time*. During the time it takes for the charge carriers to drift through the material, they diffuse by thermal motion into a distribution that is wider than originally. This causes not only an increase in the rise time of the formed pulse, but might also lead to some fraction of the pulse being collected in neighbouring strips. The spread of the charge cloud increases with drift time, and hence it may be possible to note a

difference between the p-side and n-side in those cases where the charge carriers are freed close to one of the detector sides.

In principle, particles of the same amount of energy should cause the same charge to be collected on the electrodes. However, this is not the case. For lighter particles, the detected energy is proportional to the actual energy of the particle, but for heavier particles the situation is somewhat more complex. These particles have a higher tendency to undergo other interactions (such as nuclear collisions) than just electronic collisions. As those do not result in the creation of electron-hole pairs to the same extent as electronic collisions, the total energy that is detected is decreased. Heavy particles also create a very dense track of free electron-hole pairs. This high density of charge carriers increases the probability for recombination, which reduces the total charge in the pulse. The very dense tracks of heavy particles also induce somewhat longer collection times for the pulses. This is due to a screening of the charge carriers that are inside the charge cloud by the outer part of the distribution. This increases both the time it takes before the pulse is collected and the rise time of the pulse. The increase in the time before the pulse is collected is called the *plasma time*, which refers to the plasma-like conditions in the charge could. The plasma time depends on the electric field in the part of the detector in which the ionisation is taking place, and on the denseness of the ionisation track according to the formula given in [11]:

$$\tau_{pl} = \frac{\beta}{F}\sqrt{|\frac{dE}{dx}|} \tag{2.1}$$

where β is a proportionality factor, F is the electric field strength, and $\frac{dE}{dx}$ is the energy deposited per unit length along the track. The electric field strength is larger close to the p-side than it is on the n-side, and hence it is favorable to irradiate the detector from the n-side if a large difference in the plasma time is wanted between different types of ionisation tracks.

2.1.3 Standard read-out chain

Signals from semiconductor detectors are usually read out through charge sensitive preamplifiers. A schematic picture of such a device is shown in Figure 2.2. Using an operational amplifier (shown as the triangle in the figure), the charge is integrated on the capacitor. This creates a voltage difference on the output. The voltage first increases quickly, as the charge from the detector arrives to the preamplifier. Then, the capacitor is drained over a resistor, which causes an exponential drop of the voltage. The height of the output pulse, before it starts to decay exponentially (denoted by A in the Figure 2.2) is proportional to the total charge of the detector pulse.

The preamplifier signal is, conventionally, sent to a shaping amplifier. Such modules amplify the pulse if necessary and transform the pulse into another shape, from which the energy information can be extracted using peak-sensing ADCs (Analog-to-Digital Converters). A long shaping time means that a larger fraction of the pulse is considered, which, up to some extent, can give better energy resolution. The shaping time is usually on the order of a few μs for commonly used silicon strip detector/preamplifier combinations.

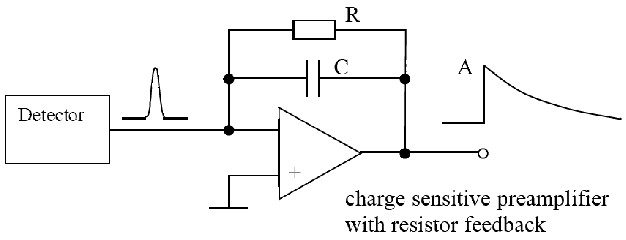

Figure 2.2: *The principle of a preamplifier. The incoming pulse is integrated on a capacitor. This creates a voltage difference on the output that is proportional to the charge of the incoming pulse. Figure from [12].*

2.2 Sampling ADCs

2.2.1 Principles of operation

During the last years, techniques for fast and high precision digitising of analog pulses have been developed into the sampling ADCs of today. Sampling ADCs are also known as flash ADCs, waveform digitizers or transient recorders, and are very similar to digital oscilloscopes. The sampling ADC digitises samples of the signal at a certain rate, and the digital values are stored in a local memory buffer.

When running the sampling ADC in "oscilloscope" mode, and an external trigger is provided, a number of pulses before and number of pulses after a trigger arrives are stored in a memory buffer which can be accessed externally. As long as the size does not exceed an upper limit set by the size of the memory buffer, any time window can be chosen. Using this mode, the actual pulse shape can be stored. As long as the Nyquist criteria, which relates the highest components of the Fourier transform of the pulse to the sampling rate that is necessary in order to capture the true form of he pulse, is fulfilled, there is no loss of information except for that introduced by possible disturbances in the digitising, and electronic noise. One of the drawbacks of running the sampling ADCs in this mode is that it very often gives large amounts of data, which can be complicated for setting up the data acquisition and data storage.

Therefore, many sampling ADCs feature an on-line processing of the data, made in on-board FPGAs (Field Programmable Gate Arrays). The FPGA operates on the continuous stream of digitised samples, and whenever a pulse is detected, which is signaled by a threshold that is exceeded in one part of the algorithm of the FPGA, the features of the pulse are extracted and read out. This reduces the data output significantly, as only a few parameters are read out. The most common existing algorithms are able to extract the energy and the time of the pulse, but more sophisticated ones are able to extract other relevant features of the pulses, for example features that can give information about particle type.

2.2.2 Characteristics and usage of sampling ADCs

The use of sampling ADCs (that have sufficient sampling rate) has great advantages over conventional electronics. As the pulse can be digitised early in the read-out process, it allows for less degradation of the pulse during transport and treatment. It is also gives a compact read-out system, as all the necessary information of the pulse can be extracted from algorithms applied to the data already inside the sampling ADC. The digital processing is also indifferent to, for example, different pulse heights, which gives a uniform treatment of the data compared to analog systems, which may give somewhat different responses to different pulses (thermal noise, discrepancies from component specifications etc.). The flexibility of the system is another advantage that can be exploited - after investigating the properties of the pulses by studying the pulse shapes, new algorithms can be programmed in order to extract the useful information of the pulses directly on the FPGA, which would be impossible using the standard approach. This allows for a customisation of the modules so that each user can store and read out the information relevant for the experiment.

Sampling ADCs are today available with several different sampling rates, ranging up to several GSamples/s (GHz sampling rate). The sampling rate is inversely related to the achievable resolution of the digitised samples, and for high-resolution spectroscopy it may be more relevant to have a high-resolution digitising than a high sampling rate. For the use of sampling ADCs together with silicon strip detectors, a sampling rate of 100 MHz (10 ns between the samples) is considered enough in order to resolve the interesting features of the pulse from the charge sensitive preamplifier. The sampling ADCs that are used for our experiment are of the type CAEN V1724 [13], which have a maximum sampling rate of 100 MHz and 14 bit resolution. The full scale range can be set to either ± 1.125 V or ± 5 V, depending on the specific detector/preamplifier setting that is used.

2.2.3 Algorithms for extraction of the energy

The algorithms employed for the extraction of interesting parameters is preferably of recursive form, so that the stream of data can be handled sample by sample. The main challenge is to find efficient and practically implementable algorithms that extract the parameters with good reliability.

According to theoretical models, trapezoidal filters are good energy filters that can compensate for ballistic deficit (which means that the rise time is not infinitely short, which would be preferable for energy extraction) and also reduce the effects of noise in the detectors [14]. The trapezoidal filter transforms the pulse from the preamplifier (a quick rise and a long exponential tail) into a trapezoid with a height that corresponds to the deposited energy. The filter also shortens the pulses to reduce pileup and restore the baseline.

Start out by assuming that the shape of the pulse is such that the rise time is infinitely short and the function is zero before the rise. Then it takes on an exponential form with one fixed time constant τ:

$$x(t) = A \cdot exp(-t/\tau) \tag{2.2}$$

An exponential slope with the different parameters used in Eq. 2.2 is shown in Figure 2.3. The height of the pulse can be extracted at any time after the

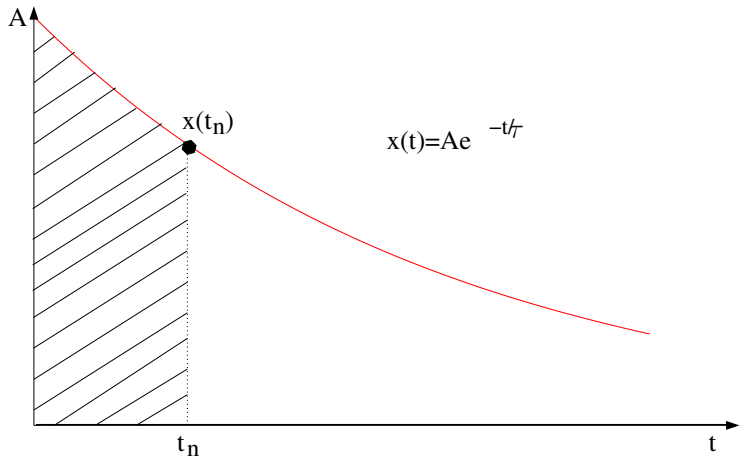

Figure 2.3: *A purely exponential slope with the height A and the time constant τ. The height A can be found as a function of any point on the curve and the integral of the part of the pulse that comes before this point.*

rise if the time constant of the decay, and the time at which the function is evaluated, is known; the height A can be found as

$$A = x(t_n) + \frac{1}{\tau}\int_0^{t_n} x(t)dt \tag{2.3}$$

where $x(t_n)$ is the instantaneous value of the function and the sum goes from the beginning of the pulse until the current time at which the function is evaluated. The above relation can be verified by the following argument:

The form of the exponential function fulfills the differential equation

$$\frac{dx(t)}{dt} + \frac{1}{\tau}x(t) = 0,\ x(0) = A \tag{2.4}$$

Integration of this equation yields, because of the fundamental theorem of calculus,

$$\int_0^{t_n} (\frac{dx(t)}{dt})dt + \int_0^{t_n} (\frac{1}{\tau}x(t))dt = 0 \tag{2.5}$$

$$x(t_n) + \frac{1}{\tau}\int_0^{t_n} x(t)\,dt = C \tag{2.6}$$

where the constant C must be equal to A because the equality must hold also for $t_n = 0$.

In discrete form, equation 2.3 takes the form

$$A = x(n) + \frac{T_0}{\tau}\sum_{k=0}^{n} x(k) \tag{2.7}$$

where the different n:s refer to the number of the samples with respect to the beginning of the pulse, and T_0 is the time step between two consecutive samples.

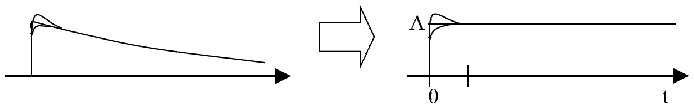

Figure 2.4: *Left: An exponential pulse with short rise time. The height of the pulse is A, and the time constant of the decay is τ. The beginning of the pulse is not decaying exponentially, and hence the result of the deconvolution (right) is not constant in the beginning of the pulse. However, after some time, the value stabilises around A. Figure from [12].*

This equation can also be written in a recursive form, in which the latest value is calculated using the previously calculated values:

$$A(n) = A(n-1) + x(n) - (1 - \frac{T_0}{\tau}) \cdot x(n-1) \tag{2.8}$$

When the function really is an exponential, then the calculated A will be a constant. It will not depend on the time at which it is calculated. In a real situation the pulse is, however, not a true exponential. The ballistic deficit gives the pulse a finite rise time, and in some cases additional time constants may have been added in the circuitry of the preamplifier. There is also noise in a real signal which destroys the purely exponential behaviour. Therefore, the pulses are not necessarily exponential, especially not in the beginning. In those cases, the output of this algorithm is not a constant, but a function that depends on the previous shape of the pulse. During the rise time, the output is not a meaningful quantity, but as the pulse starts to decay exponentially, the output value will stabilise around A.

The previously described process to extract the constant A is called deconvolution. The reason for this is that the effect of the algorithm is to separate out the pulse from the detector from the preamplifier output, which is a convolution of the detector signal and the intrinsic preamplifier response function. The deconvolution process is illustrated in Figure 2.4.

The next step in the treatment of the data is to make the pulses shorter and to restore the baseline to the original value. This is done by taking the difference between the value at hand and a previous value, that is taken from M steps back in time:

$$\Delta A(n) = A(n) - A(n-M) \tag{2.9}$$

The process is illustrated in Figure 2.5. During the first part of the pulse, which comes before the value M is reached, the pulse is unaffected by the subtraction of the previous value since this value is zero or at least a small number. When the duration of the pulse is longer than M, the values from the first part of the pulse are starting to be subtracted from the current value, and the output pulse will decrease in height until it reaches a point where the values cancel each other

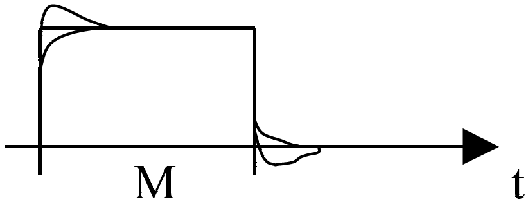

Figure 2.5: *Illustration of the "differentiation", showing the result of the process applied to the deconvolved pulse in Figure 2.3. Before the width of the differentiation parameter M is reached, the pulse is unaffected by the process. After time M, the pulse is canceled by the contributions from the beginning of the pulse. If there was an overshoot in the beginning of the pulse, there will be an undershoot in the end of the differentiated pulse and vice versa. Figure from [12].*

completely. The parameter M is the digital correspondence to the shaping time of an analog shaping amplifier.

Re-writing Eq. 2.9 as a function of the initial samples, the equations turns into

$$\Delta A(n) = x(n) - x(n-M) + \frac{T_0}{\tau} \sum_{k=n-M}^{n-1} x(k), \tag{2.10}$$

which in turn can be written in recursive form as

$$\Delta A(n) = \Delta A(n-1) + x(n) - (1-\frac{T_0}{\tau})x(n-1) - x(n-M) + (1-\frac{T_0}{\tau})x(n-M-1). \tag{2.11}$$

The deconvolution and differentiation process does not improve the signal-to-noise ratio, but an averaging will. Therefore, the last step is to calculate averages using a so-called moving window average. This means that every new point is calculated as the average of a number of previous points. The term "moving window" arises because this process can be described as moving a time window over the data and calculating the average of the contents within the time window for each time it is moved one step. The procedure is illustrated in Figure 2.6. The resulting output of such a treatment of a square pulse is a trapezoidal function with the length of the flat top being the length of the input pulse (in this application approximately M) minus the length of the moving window, which is denoted by L. Due to the final shape of the pulse after the processing, the moving window deconvolution is also called a trapezoidal filter. The process of averaging reduces the problems with noise, as fluctuations are canceled. In the ideal case, the top of the pulse is completely flat which means that the energy can be extracted at any point on the flat top and give the same value.

The very last step of the algorithm is to take out a value on the flat top of the resulting pulse, which will be the measure of the energy of the pulse. The position at which the flat top of the pulse is evaluated can be chosen as a point that comes a certain number of samples after some threshold is passed.

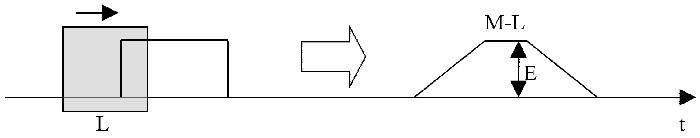

Figure 2.6: *Illustration of the moving window average. The average value is calculated from an interval of points, which is moved over the data. Starting from a square pulse, the output is a trapezoidal with a flat top of length M-L, where M is the length of the pulse and L is the length of the interval used for the averaging. Figure from [12].*

In order to get good energy resolution, the parameters must be carefully considered. Firstly, the time decay constant τ must be known. Secondly, the parameter M, which describes how large a fraction of the pulse that is kept, must be sufficiently long in order for the value to stabilise. Also, the width of the moving window average must be chosen in such way that the noise is canceled in a satisfactory way.

Chapter 3

Experimental Setup

3.1 Overview of TASISpec

The TASISpec setup consists of one DSSSD and four SSSSDs which are surrounded by five composite germanium detectors, as pictured in Figure 1.2. The device is specifically made to be operated together with the TASCA separator at GSI, which is capable of focusing heavy ions with kinetic energies of a few tens of MeV towards the DSSSD. The heavy ions are implanted into the detector, and their subsequent decays can be detected with high efficiency - a large fraction of the decay products that escape backwards out of the DSSSD are instead captured by the four SSSSDs placed upstream of the implantation detector like the sides of a box.

The silicon detectors can be surrounded with up to five germanium detectors. A so-called CLUSTER detector [15], which consists of seven separate crystals, covers the back side of the implantation detector. On the four remaining sides, behind the SSSSDs, CLOVER detectors [16] with 4 crystals each can be placed.

The heavy ions to be studied are produced in fusion-evaporation reactions between nuclei in a thin target foil and a beam of heavy ions. The ions are extracted from an ion source and are accelerated through the linear accelerator UNILAC at GSI to energies of a few MeV per nucleon. This energy can be finely tuned to give the highest production cross sections for the reaction of interest.

The beam hits a thin foil on a rotating target wheel, and several reactions can take place. In order to produce SHE, it is necessary to use fusion-evaporation reactions. The primary fusion process does, generally, have smaller cross sections than competing processes like nucleon-transfer reactions. There is also a large possibility for beam particles to pass through the target unaffected. Therefore, a separation process is needed to separate hence purify the different reaction products from each other. The TASCA separator, which is placed after the target wheel, consists of a magnetic dipole in which particles of a certain momentum-to-charge ratio are selected. The dipole is followed by two quadrupole magnets which focus the selected ions towards the focal plane of TASCA.

An interesting feature of TASCA is that the polarity of the TASCA quadrupoles can be exchanged to give two different modes - the "Small Image Mode" focusing the ions towards a spot of less than 3 cm in diameter, and the "High Transmission Mode" which has a higher transmission factor but a broader focal plane

of about 14 cm $\times$ 4 cm. TASISpec employs TASCA in Small Image Mode. This enables a very tight detector geometry that provides a very high detection efficiency [17].

The ions are implanted in the DSSSD with energies of typically tens of MeV, which means that they travel a few micrometers into the detector. The particles that are emitted backwards from the DSSSD are captured in the surrounding SSSSDs with an absolute efficiency of 30% for, for example, α particles. The emitted γ rays are detected mainly in the surrounding germanium detectors.

The TASISpec setup has been and will be used for various spectroscopic measurements. So far, the main experiment has been focused on studies of isomeric states in ^{253}No. A coming future flagship experiment aims at X-ray fingerprinting of element $Z = 115$ decay chains.

3.2 Detectors relevant for the experiment

The DSSSD used as an implantation detector is segmented into 32 strips on each side, with a total active area of 58 mm $\times$ 58 mm. Each strip is separated from neighbouring strips by an inactive area of 60 μm. The detector is positioned such that the p-side faces the beam. The dead layer is only about 0.5 μm on the p-side whereas the dead layer of the n-side is about four times thicker, which would make it more difficult to properly detect the heavy implanted ions that only reach a few μm into the detector. The strips on the p-side are oriented such that this side determines the position on the y-axis and the n-side determines the position along the x-axis. The detector used for this experiment has a thickness of 0.52 mm.

The SSSSDs have an active area of 60 mm $\times$ 60 mm and are segmented into 32 separate strips, oriented along the beam axis. The thickness of these detectors is 1.0 mm. The geometrical coverage for particles emitted from the center of the DSSSD is 81%, and the detection efficiencies for α particles and conversion electrons are similar to this value.

The silicon detectors are positioned inside a detector chamber. The thickness of the sides of this structure facing the surrounding germanium detectors are only about 0.5 mm thick in order to cause as little scattering or absorption of photons as possible.

3.3 Electronics

The read-out of the DSSSD is normally made in a classic analog electronics chain. In order to investigate the characteristics of the new electronics, the signals from the DSSSD preamplifiers were passively split into two identical signals - one of those was processed by the conventional chain and one by the digital sampling ADCs. The electronics scheme for the read-out of the DSSSD is shown in Figure 3.1.

As only four V1724 sampling ADCs with 8 channels each were available, only the 16 central strips of the p- and n-side of the DSSSD were processed. The detector signals were read out by 32-channel preamplifiers built at Cologne University. Special preamplifier connectors were constructed in order to select

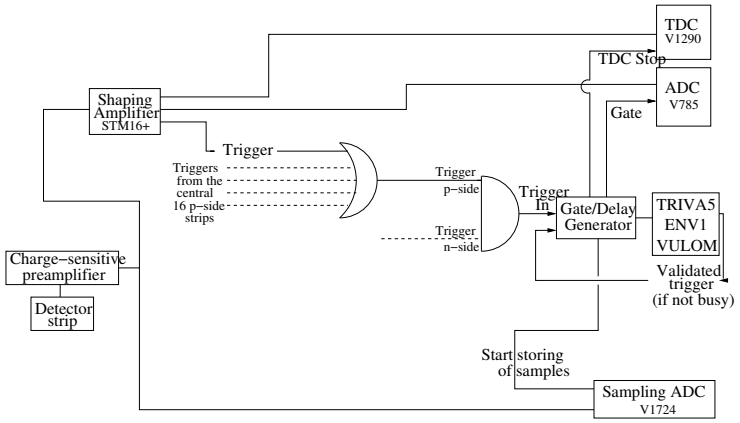

Figure 3.1: *The electronics scheme for the DSSSD read-out.*

the respective 16 central strips of each side only. The signals were passively split into two branches.

The conventional electronics chain is displayed in the upper part of Fig. 3.1. The 16 outputs from the p-side of the detector are processed by one shaping amplifier of type Mesytec STM16+ [18], and the output of the n-side goes to another STM16+ module. The STM16+ modules provide two output signals; a shaped energy signal and a logic ECL timing signal. The shaped analog energy signals are digitised by 32-channel VME ADCs of the type CAEN 785. The timing output goes to VME TDCs of the type CAEN 1290A.

The shaping amplifiers also produce a trigger signal if any of the channels detect a pulse that is above a pre-set threshold. In order to get only those events that contain signals on both p- and n-side of the detectors, the trigger signals from the two amplifiers were joined in a logic coincidence module, set to AND mode, which produced the final trigger.

The trigger is validated using the GSI VME-modules ENV1, TRIVA5 and VULOM. If the system is busy with reading out the previous event, the trigger will be rejected. If not, the trigger is sent to the gate and delay generator, which sends out signals that are required for the VME-modules in order to acquire and digitise the relevant data.

The trigger output also starts the storing of the samples that are continuously being digitised by the sampling ADCs. The system was set up such that 256 samples were stored for each event. This corresponds to a total time of 2.56 μs per event. The delays were set so that the rise time of a pulse which triggered the system is positioned approximately 80 samples into the stored array. This array of digitised samples is commonly called the "trace" of the event.

3.4 Data collection

The experiment to investigate the performance of the sampling ADCs was made using both an α source and an in-beam measurement. A triple α source containing ^{240}Pu, ^{241}Am, and ^{244}Cm was used for irradiation and calibration of

the DSSSD in order to get a measurement with well-defined peaks to be used for a straight-forward comparison between the resolution of different energy filters. The source was mounted on a holder that was inserted into the TASISpec chamber, so that the source itself was placed near the center of the DSSSD, a few centimeters away from it.

For the in-beam measurement, the fusion-evaporation reaction between a beam of ^{48}Ca and a target of ^{207}Pb was chosen. The ^{48}Ca beam was accelerated to energies of 4.83 MeV/nucleon in the UNILAC accelerator, and was incident on a rotating target wheel with ~ 0.5 mg/cm^2 ^{207}Pb on a backing foil of $\sim 2\mu$m Ti. The reaction of interest is a fusion-evaporation between beam and target in which two neutrons are evaporated: ^{207}Pb(^{48}Ca,$2n$)^{253}No.

The products of the collisions are purified in the gas-filled TASCA separator, depicted in Figure 3.2. The first section is a 30° magnetic dipole which directs the particles into different directions depending on the momentum-to-charge ratio. The radius of the trajectory in the magnetic field is

$$r = \frac{mv}{qB} \tag{3.1}$$

where m, v and q denote the mass, velocity, and charge of the ions, respectively. B is the strength of the magnetic field. The kinematics of the fusion reaction is strongly forward focused, and has only a small spread in velocity which is due to the evaporation of neutrons and scattering in the target. Hence, the momentum of the particles of interest is known. Also the approximate mass of the fusion-evaporation residues is known. Therefore, the only unknown parameter is the charge state of the ions.

After leaving the target, the ions have a broad distribution of atomic charge states. Ions in different charge states follow separate trajectories inside the separator, and thus, a strong focusing of all ^{253}No charge states is difficult to achieve. In order to select not only one but all charge states of the ions, the separator is filled with a low-pressure gas. This leads to an equilibration of the charge states because the ions constantly exchange electrons with the gas. They will take on an average charge state and, hence, all atoms of the same mass and velocity will follow the same *average* trajectory through the separator. This allows for a selection of all the ions of interest regardless of the initial charge state.

The average charge state depends on the charge of the nucleus, its velocity, the gas pressure and the gas composition. Empirical formulae for the average charge state exist for some gases, including He [20] which was used in our experiment. The ions within the accepted span of velocity and mass will then pass through two quadrupole fields; one that focuses the beam in the vertical direction (Q_v) and one in the horisontal direction (Q_h). A special feature of the TASCA quadrupoles is the capability of operation in two different modes which makes it possible to switch between the two configurations DQ_hQ_v and DQ_vQ_h. The transmission and focusing properties of the separator are different in those two modes. TASISpec employs the Small Image Mode (SIM) configuration, DQ_vQ_h. This results in the beam spot on the DSSSD being less than 3 cm in diameter.

The time structure of the UNILAC beam is such that the beam is on for 5 ms and then off for 15 ms. This means that the data that is collected during the periods with beam on target contains a mixture of implantations of ^{253}No,

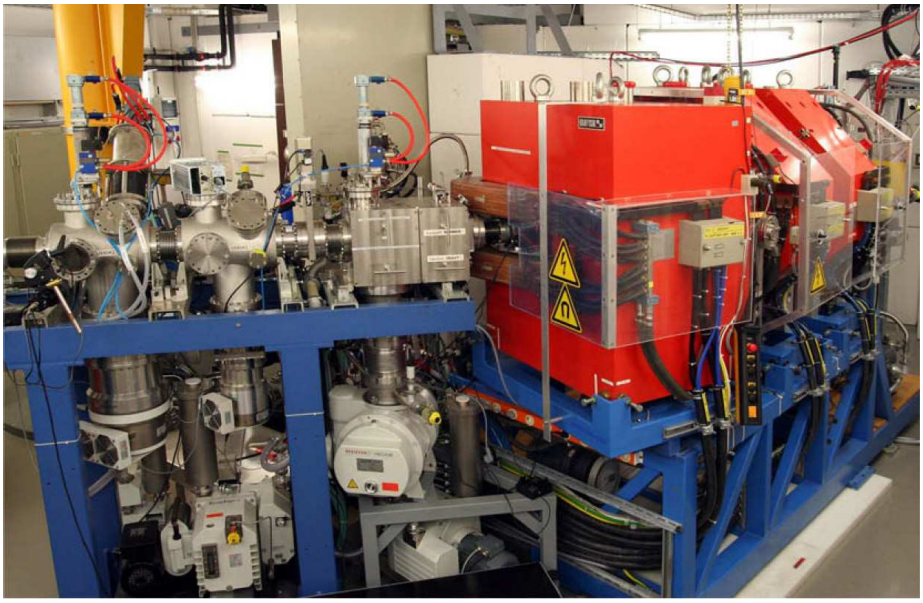

Figure 3.2: *The TASCA recoil separator. The beam enters the beamline from the left. The target section is seen in the middle. The first orange-painted magnet is the dipole and to the right the two quadrupole magnets are seen. Picture taken from [19].*

decay of ions that have been implanted, and scattered background. During the periods when there is no beam on target only decays of previously implanted ions are seen. In order to separate the two different situations, a flag which indicates whether the beam is on or off is added to the information that is read out for each event, which allows for an offline separation of the two cases. The in-beam data collected for this experiment covers about 8 hours of beam-time.

Chapter 4

Experimental Results: Energy Extraction

The relevant output of the experiment consists of the traces from the DSSSD and the information from the ADC from each event. Each proper event contains 32 traces; 16 from the central strips of the p-side of the DSSSD and 16 from the central strips of the n-side, and the energy information from the same 32 strips from the conventional electronics. In our experiment the count rate of the DSSSD was kept low and the time during which the system is open for recording events is short (2.56 μs for the sampling ADCs and $\sim$ 5 μs for the standard electronics) which means that most events will contain a hit in only one pixel while the rest of them are empty. In the case of standard electronics, there is no output from the empty strips if nothing above threshold is detected, while the traces are recorded regardless of the contents.

4.1 Standard electronics

Energy spectra

A raw energy spectrum from a strip of the p-side of the DSSSD from the standard electronics is shown in Figure 4.1. The spectrum is from irradiation with the 3-line α source. The hardware threshold is set such that pulses below approximately 90 units are discriminated, which corresponds to around 0.5 MeV.

The data was calibrated using the first and the last peak of the 3-line α source. These two lines correspond to the decay of ^{240}Pu with an alpha energy of 5.14 MeV and ^{244}Cm with an alpha energy of 5.80 MeV. The dead layer of the DSSSD being approximately 0.5 μm, and the average energy loss of an α particle of these energies being approximately 140 keV/μm, lead to recordable energy depositions of 5.07 and 5.73 MeV, respectively, in the detector. Gaussian functions were fitted to the peaks, and a two-point calibration was made using the peak positions. The resolution of the lowest and the highest peak were determined by fitting Gaussian functions to the peaks and multiplying with the factor 2.35, which gives the resolution in FWHM (keV). The resulting resolutions were 61 keV for both peaks, which will from now on be taken as the reference values to which the other energy resolutions will be compared.

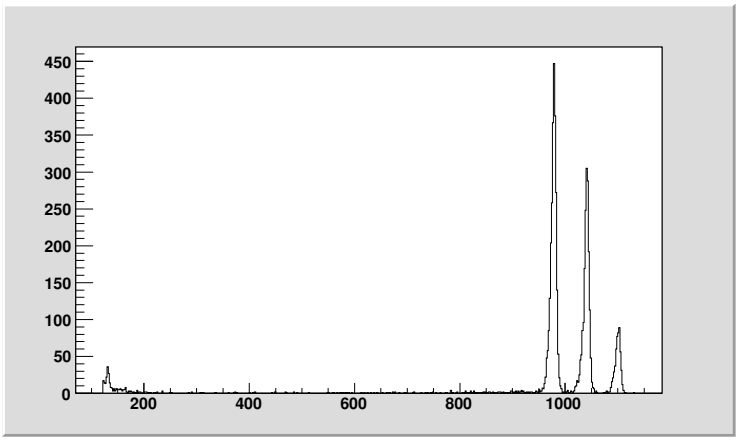

Figure 4.1: *Energy spectrum from the standard electronics, created by irradiation using an α source.*

DSSSD multiplicity

One relevant feature of the data is the multiplicity of the DSSSD, which is the number of strips that contain a valid hit for every time there is a trigger. To quantify this, the multiplicity was calculated as the number of strips that contained energy in excess of 1 MeV. Multiplicity spectra from the p-and the n-side, respectively, are shown in Figure 4.2 from the measurement with the 3-line α source. The multiplicity for most events is 1, and only a few events have a higher multiplicity. This low multiplicity depends on both the settings of the electronics and the strength of the source. The events with multiplicity equal to 0 are events that were inconsistently interpreted by the electronics modules; even though the pulses passed the discriminator in the shaping amplifier so as to trigger the system, the ADCs still did not record any energy above the inherent threshold of the ADC. Those events will not be further considered. For some parts of the following analysis, only those events that have multiplicity equal to 1 will be used.

Correlations between p-side and n-side

In order to establish the relation between the energies that are recorded from the p-side and the n-side, the events with multiplicity equal to 1 on both sides were plotted in a 2D histogram shown in Figure 4.3. The x-axis shows the energy recorded in the strip on the p-side, and the y-axis represents the energy recorded in the strip on the n-side.

The three peaks from the source can be clearly distinguished in the plot. They are positioned along a line with unit slope, as expected due to the calibration of the peaks. All events along this line are those giving a signal fully absorbed inside a pixel and properly analysed in the read-out on both p- and n-side. What is more interesting are those events that do not fall upon the line which corresponds to a one-to-one relation between the p- and n-side. The vertical lines below the three peaks correspond to events where the energy detected

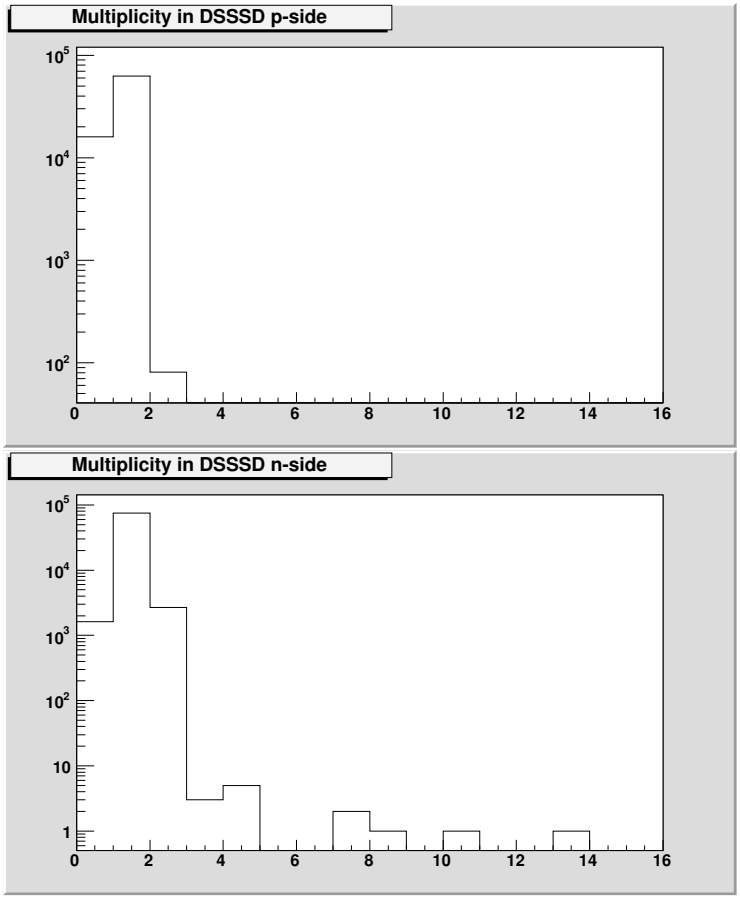

Figure 4.2: *The DSSSD multiplicity of the p- and n-side, respectively. The multiplicity is the number of strips for each side that contains energy in excess of 1 MeV. The strips number 4, 8 and 14 have been excluded (on both sides) from the calculations. The most common multiplicity is 1, meaning that only one of the strips of each side contained a hit for those events.*

by the pixel on the n-side is less than that of the p-side of the pixel. This is probably due to the diffusion of the distribution of charge carriers as they travel through the detector, which causes some part of the distribution to be absorbed by another strip than the one that was originally hit. Since the only events displayed in the figure are those with multiplicity 1 in both sides, and the multiplicity is counted only for pulses that are above 1 MeV, the events that have an energy split so that a fraction of less than 1 MeV ended up in a neighbouring strip, are seen in the figure. Those events are seen in a band with a width of 1 MeV below the main line. This explanation also accounts for why there is no corresponding structure on the other side of the peaks - the radiation enters the detector from the p-side and therefore the chances for having absorption in more strips on the p-side but just one, is small since the drift time for the charge carriers on the p-side is smaller. The line of events downwards to the left from the peak with the lowest energy is a feature so far unexplained.

The events that do not leave all their energy in one strip but in two, can, in principle, be used for a better determination of the position of impact compared to the actual pixellation due to the size of the strips. An analysis of these events on a pulse shape basis may be of interest for future use of sampling ADCs, since it may be the case that e.g. some features of pulses in the neighbouring strips to the one being hit could show some extractable features useful for positioning of the event.

4.2 Digital energy filtering

The processing of the traces from the sampling ADCs was performed partly in the ROOT-based program Go4 and partly using LabVIEW. The first step is to investigate the extraction of energy information from the raw samples. Some energy filters that could be implemented in Go4 were constructed, and the use of a so-called Moving Window Deconvolution (MWD) was implemented using LabVIEW.

4.2.1 Raw samples

Three unprocessed traces from each side of the detector, centered around the pixel in which an α particle from the source was detected, are shown in Figure 4.4 and 4.5.

The first set of figures is from the p-side of the detector. The middle trace shows the characteristic shape of the output from a preamplifier - a fast rise time and then an exponential decay as the capacitor is discharged. The sampling ADCs digitise the signals at a rate of 100 MHz, which gives a spacing between consecutive data points of 10 ns. From the figure, it can be seen that the rise time of the slope is approximately 60-70 ns, which is a typical value for detectors of this type and geometry and for the preamplifiers used.

The exponential decay of the pulse depends only on the electronics components in the preamplifier, and is hence not an important feature of the pulse shape when it comes to possible characterisation of the event. However, in order for the energy extraction algorithms to work, it is necessary to know some fraction of the exponential decay. Therefore, a part of the decay slope was recorded, but not all of it.

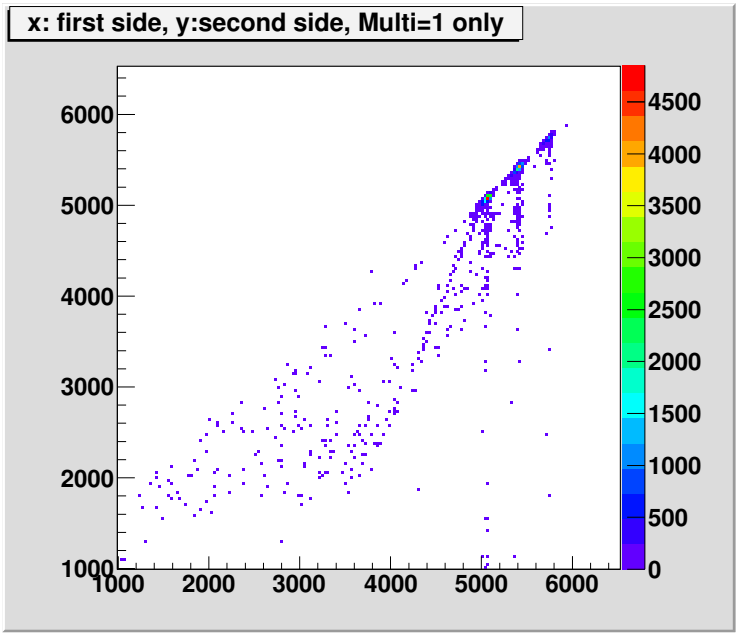

Figure 4.3: *2D histogram showing the events with multiplicity equal to one in both p- and n-side. The x-axis is the energy deposited in the strip on the p-side, and the y-axis is the energy recorded in the strip on the n-side. Note that the histogram contains information from all strips on p- and n-side, not just from one pixel. The scale to the right shows the number of counts that the different colours correspond to.*

The output pulse from the preamplifiers connected to the n-side of the detector has negative polarity, as opposed to that of the p-side. This is shown in the second set of traces in Figure 4.5. The inherent noise is approximately on the same level in all the four displayed traces that do not contain a real pulse; two from the p-side and two from the n-side.

4.2.2 Digital filtering

In order to investigate the properties of the traces and the different methods that can be applied in order to extract the energy in the best possible way, several different digital energy filters were coded. The first three versions were programmed in Go4/ROOT/C++ as pure "offline" treatment of the data, since they require the knowledge of the whole trace beforehand. However, it may be possible to construct online versions that are based on the same principles that are investigated in these filters. Different versions of the MWD were programmed in LabVIEW, and are algorithms that can be directly used for online extraction of the energy, as they are implemented using recursive formulae.

Energy filter version 1

The first and simplest energy filter that can be constructed is to calculate the height of the pulse by taking the difference between the maximum and minimum value of the pulse, as illustrated in Figure 4.6. Clearly, this will not be the final choice for an energy filter - the extracted values are going to be somewhat higher than the real ones due to the noise, and the spread of the resulting energies will be large.

Two of the resulting energy spectra are shown in Figure 4.7 (red), together with the corresponding spectra from the standard electronics (black). All spectra are calibrated using the method described in section 4.1. The top spectra represent data from strip number 10, which is on the p-side of the detector. As expected, the resolution that resulted from the digital energy filtering is not as good as the one of the standard electronics, as can be seen directly in the figure by looking at the α peaks. However, considering the trivial approach, the resolution is surprisingly good. For the peak with the highest intensity, it is 99 keV compared to 61 keV for the standard electronics for this strip. The resolutions of all the different energy filters for two different strips are summarised in Table 4.2.

The other prominent difference between the spectrum from the digital filtering and the spectrum from the standard electronic is is the low-energy noise peak in the spectrum from the traces. Since the traces are recorded regardless of the contents, the vast majority will contain noise only, due to the low DSSSD multiplicity that was used. For the following energy filters, a software threshold was set so that only those events that gave an energy of above 0.8 MeV in this version of the energy filter were considered further.

Another noticeable feature is that the number of events with energies below that of the peaks but above the noise, is larger for the filtered energies than for the standard electronics. This may be due to noise with very high amplitudes that is captured by the sampling ADCs but not by the standard electronics, in which some filtering has already taken place when the peak-sensing ADC receives the pulse.

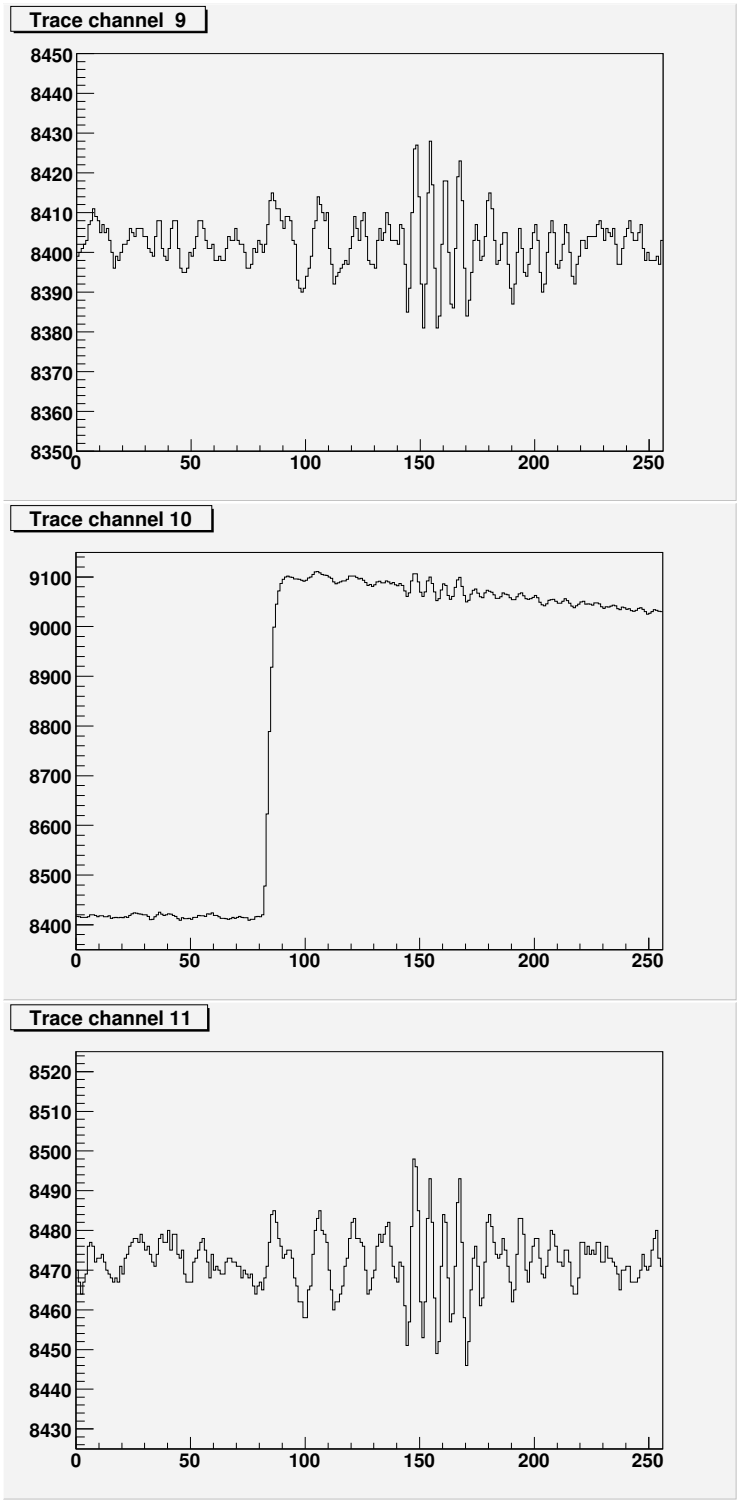

Figure 4.4: *Three traces from the p-side of the detector. The middle trace contains the pulse from the detection of an α particle. The time interval between each sample is 10 ns. The top and bottom figures show traces from the surrounding strips that were not hit by α particles, which means that they contain noise only. The noise levels in those two traces seem to be very similar. All three traces exhibit noise spikes around sample $\sim$150, which are probably caused by the external trigger signal arriving to the trigger input of the sampling ADC.*

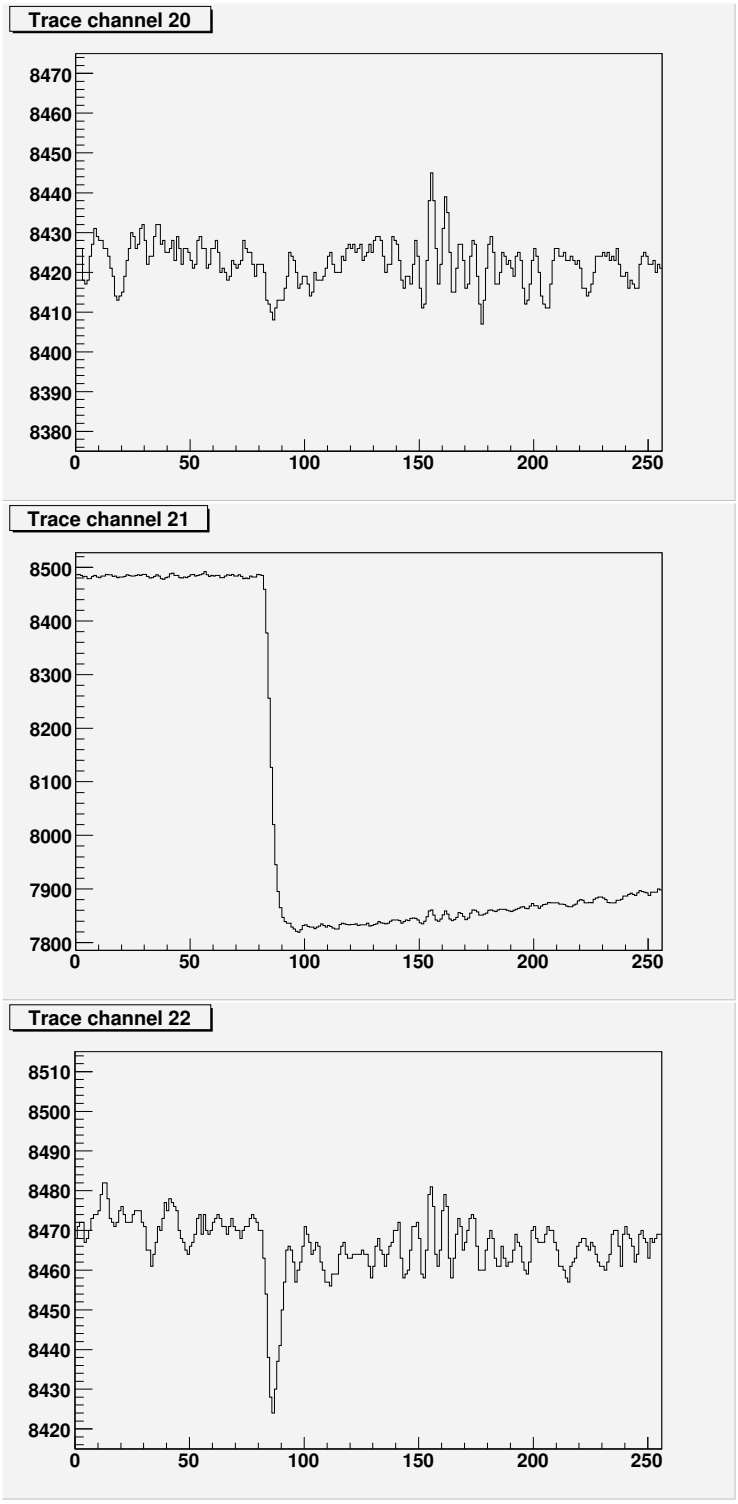

Figure 4.5: *Three traces from the n-side of the detector. The pulse of channel 21 has a clear signal with negative polarity.*

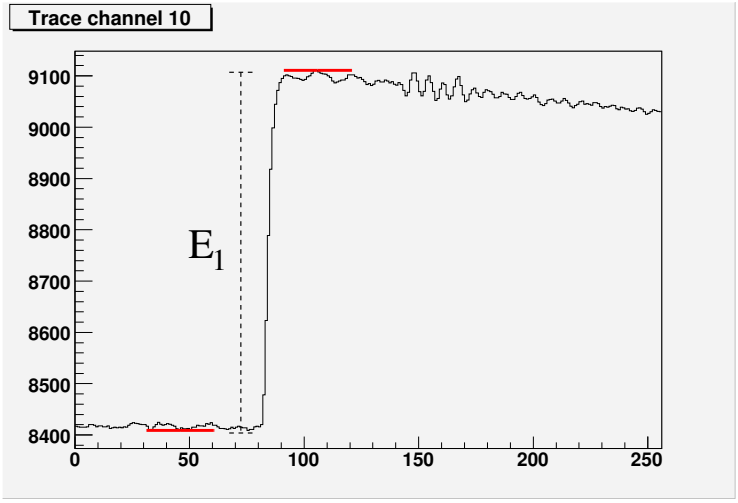

Figure 4.6: *The first version of the energy filter, E_1, takes the difference between the maximum and the minimum as the height of the pulse. The maximum and minimum are marked by horisontal red lines.*

The second part of Figure 4.7 shows the energy spectrum resulting from a strip on the n-side of the detector compared to the standard electronics. The resolution is less good also in this case, as is displayed in Table 4.2.

Energy filter version 2

In a second version of the offline energy filter, the baseline is calculated as the average of the first 70 samples of each trace. The baseline varies a little in time, and therefore the baseline is calculated for each trace, and not only once for each strip. To extract the energy, the difference between the extremum point, (the maximum in case of the p-side and the minimum in case of the n-side) and the baseline. The method is illustrated in Figure 4.8.

The resulting calibrated energy spectrum is shown in Figure 4.9. This version of the filter gives slightly lower energies than the first filter, since the average instead of the extremum point is used for the baseline. Therefore, the calibration was re-done. The resolution is improved compared to the first energy filter; for the peak with the highest intensity the resolution is 82 keV, whereas it is 99 keV for the first version of the energy filter.

Energy filter version 3

A third version of the energy filter was constructed using an extrapolation of the exponential slope. The principle is illustrated in Figure 4.10. The function that was fitted to the exponential slope was of the form

$$a_0 \pm e^{a_1} \cdot e^{a_2 \cdot x} \tag{4.1}$$

The +(-) sign is applied for the traces with positive (negative) polarity. The function was fitted to the slope with the condition that the constant a_0 is within

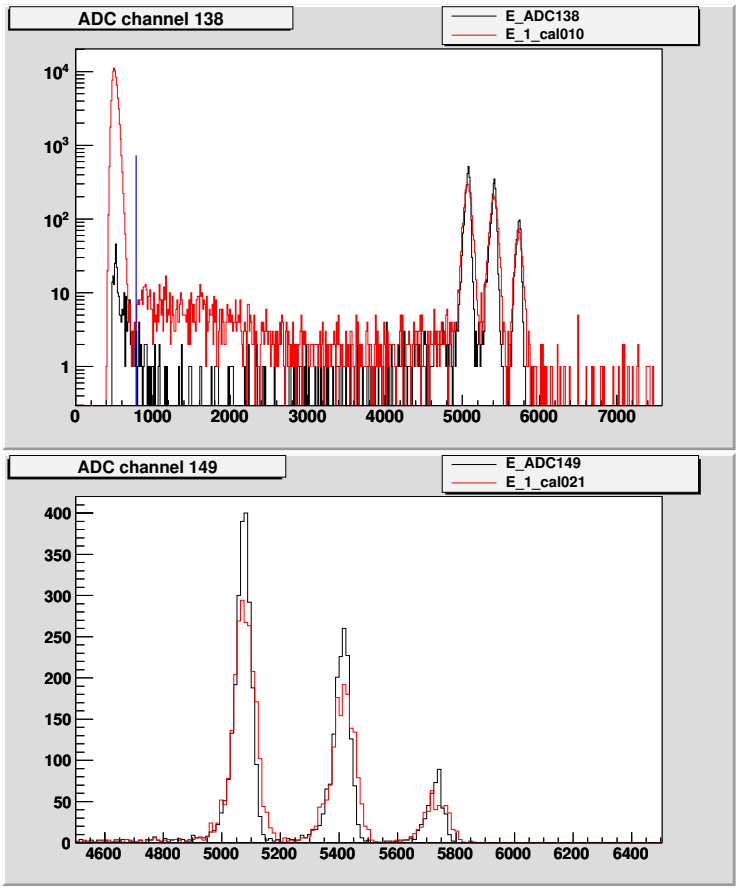

Figure 4.7: *Calibrated energy spectra from energy filter version 1. The top spectra show the entire energy spectra from strip number 10 on the p-side of the detector (red) and the energy spectrum from the same strip from the standard electronics (black). The three peaks from the 3-line α source are high-lighted in the bottom spectra, which represents a strip on the n-side of the detector.*

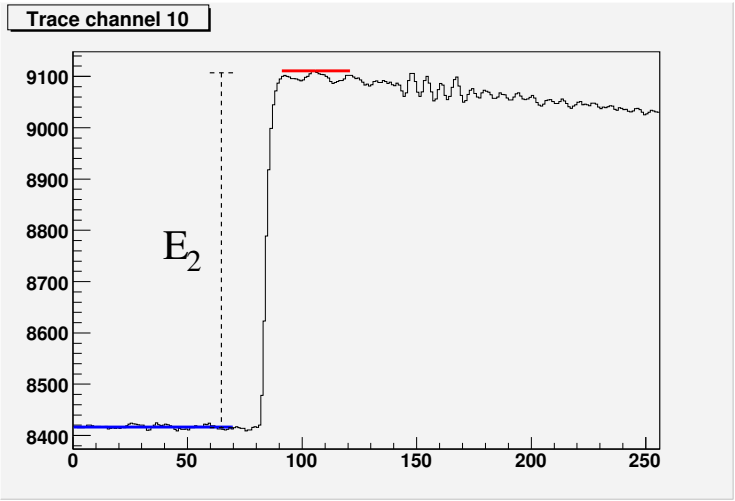

Figure 4.8: *The second version of the energy filter, E_2. The baseline (blue) is calculated as the average of the first 70 samples of each trace. The energy is calculated as the difference between the extremum point (marked in red) and the baseline.*

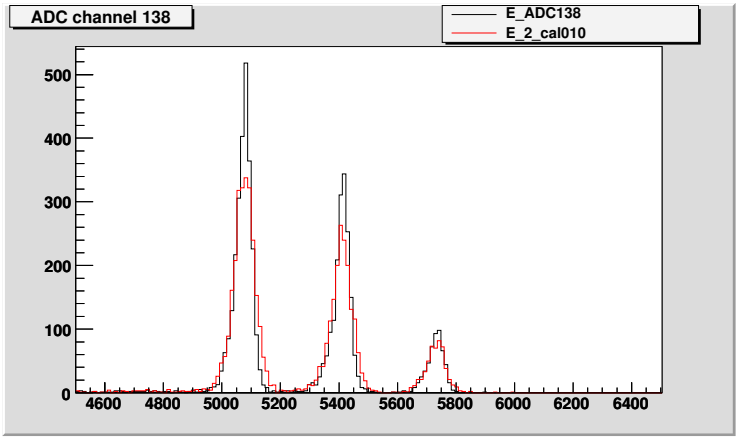

Figure 4.9: *Calibrated energy spectra from the second filter (red) and from standard electronics (black) from strip 10 of the p-side.*

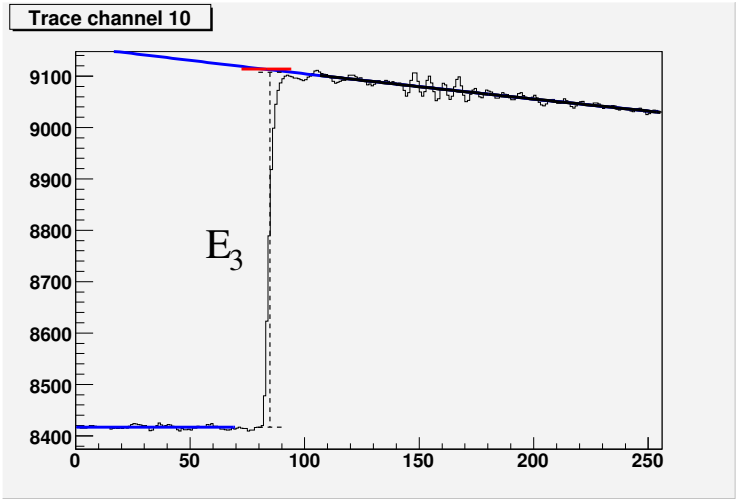

Figure 4.10: *Third version of the energy filter, E_3. An exponential function is fitted to the slope (black), and extrapolated (blue line). The red line marks the height of the extrapolated function at the middle of the rise of the pulse. The energy is calculated as this number minus the baseline (blue).*

a span of $\pm$ 5 from the baseline that was calculated from the first 70 samples. The region used for the fitting extends from the bin which holds the maximum (minimum) bin until the end of the trace. The exponential function is then extrapolated towards the beginning of the trace. The energy was calculated as the difference between the exponential function at the middle of the rise and the baseline. The middle of the rise was calculated as the mean of the derivative of the pulse, as will be described more thoroughly in section 5.1.2 where the characteristics of the rise time will be discussed.

This energy filter reduces the noise-induced fluctuations of both baseline and extremum values, and hence is expected to have an improved energy resolution compared to the previous filters. The resulting energy spectrum from a strip on the p-side is shown in Figure 4.11. The resolution is 66 keV for the peak with the highest intensity, which in fact is a considerable improvement from the earlier filters. For the standard electronics the corresponding value is 61 keV. Therefore, this version of the filter gives a resolution that is comparable to what can be achieved conventionally.

The stability of the fitting procedure was tested by plotting the value of the decay parameter (a_2) as a function of energy per event. This is shown in the top spectrum of Figure 4.12. For the α peaks and the higher energy part of the spectrum, the parameter stays approximately constant. This is seen more clearly in the bottom part of the figure, in which the distribution of the parameter, separated according to the different peaks of the α source, are displayed. The mean value was determined to be $-7.78 \cdot 10^{-4}$ for this strip. This shows a good consistency with expectations, since the slope should depend only on the combination of detector and preamplifier and not on the energy of the pulse. The spread in the values indicates that either (i) the preamplifier suffers

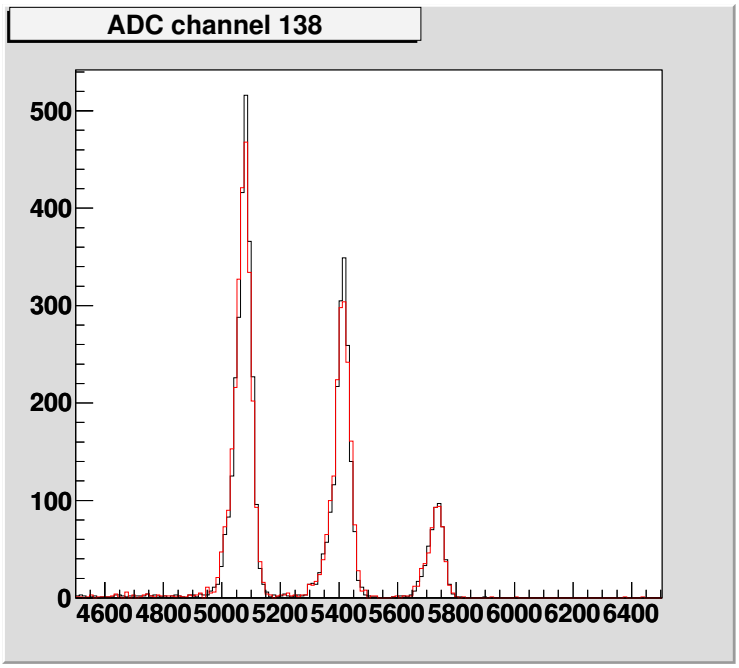

Figure 4.11: *Calibrated energy spectra from the third energy filter (red) and from standard electronics (black), from strip number 10 of the p-side.*

from some inherent instability, or (ii) the fitting procedure does. It seems more likely that the uncertainty arises from the fitting procedure. Consequently, a fixing of the slope parameter to the mean value of the slope was made. The mean value depends on the channel of the preamplifier, and was found by fitting a Gaussian function to the distribution of parameters, as those provided in Figure 4.12.

A new energy spectrum was extracted using the same procedure as illustrated in Figure 4.10, with the only difference that the slope is now fixed to the mean value from the previous fitting procedure, and the only parameter completely free is the constant that describes the height of the pulse compared to the baseline. The resulting energy spectrum is shown in Figure 4.13. The resolution for the peak with the highest intensity is 61 keV, which is the same as for the standard electronics. This implies that this method could be used for extraction of energy information from recorded traces without losing energy resolution compared to standard electronics.

Another version of this filter was tried as well - the average was calculated for groups of 10 samples before the fitting procedure was carried out as described above. The averaged trace is shown in Figure 4.14. The noise on top of the exponential slope has now been removed, as can be seen by comparison with the central part of Figure 4.4, which shows the very same trace before averaging. The functions were fitted on the regions indicated in the figure, i.e. the baseline is calculated from the beginning of the trace to four bins less the maximum (minimum) bin, and the exponential function is fitted from the maxi-

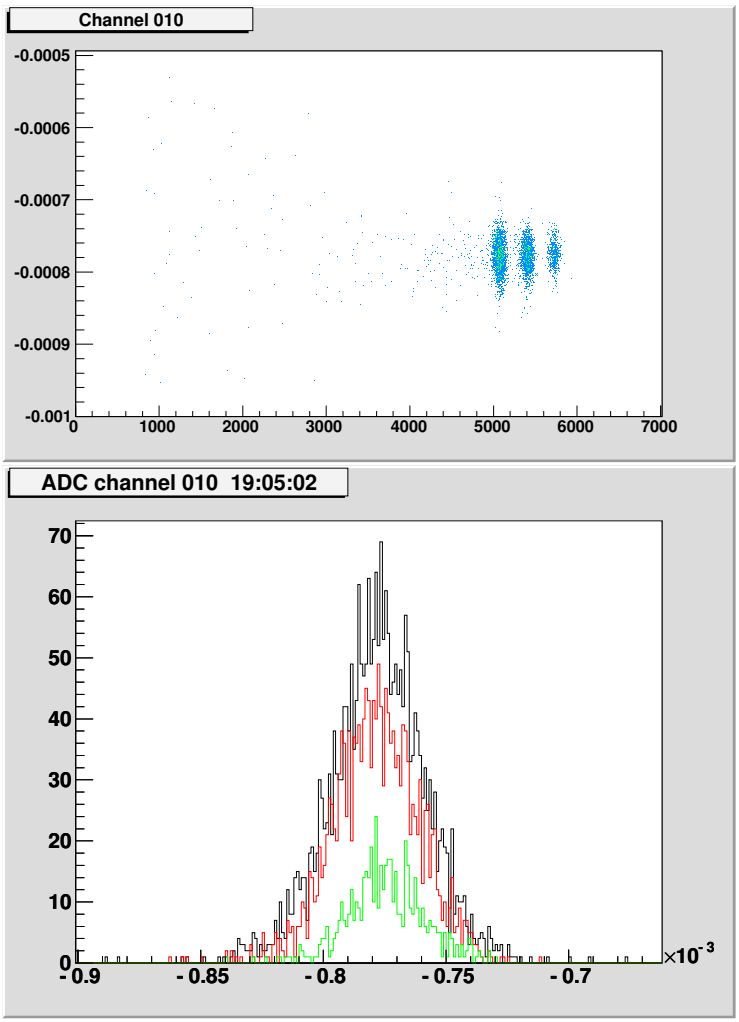

Figure 4.12: *Top: The distribution of the parameter a_2 of the fit (cf. eq. 4.1), shown for strip number 10, as a function of energy. Bottom: The distribution of the parameter separated into the three different peaks. The mean value is determined to be $-7.78 \cdot 10^{-4}$ for this strip.*

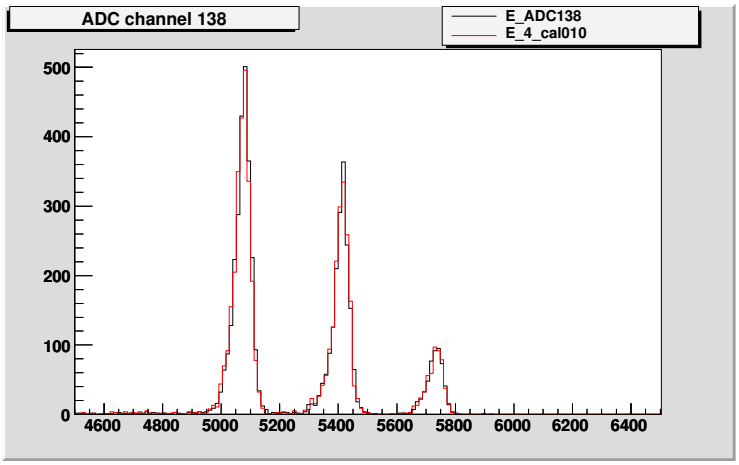

Figure 4.13: *Calibrated energy spectra from the third energy filter with a fixing of the decay parameter of the exponential slope (red) and from standard electronics (black), from strip number 10 of the p-side. The energy resolution of the highest peak actually exceeds the resolution of the standard electronics.*

mum (minimum) bin to the end of the averaged trace. The time at which the exponential function is evaluated is one tenth of the time that was calculated and used for the non-averaged trace. The energy resolution that results from this procedure does not show any large improvements over the previous method - the resolution is basically the same as displayed in Table 4.2, implying that the fitting procedures are not severely affected by the noise, or by having fewer points to fit. It may be possible to gain a little resolution by, for example, making a moving-window average instead, or by using another length of the interval over which the averages are calculated, even though the improvements are most likely not very large.

Moving window deconvolution

A moving window deconvolution algorithm, as described in Section 2.2.3, was applied to all those traces that had energies in excess of 0.8 MeV according to the first version of the energy filter. The sampled values from these events, from one strip, were stored after each other in a text file that was taken as the input of a LabVIEW program. The program reads and processes one sample at a time, and can hence be directly used for online, real-time processing of data.

Figure 4.15 shows an instant picture of how the pulses are treated in the LabVIEW program. The uppermost part of the figure shows the raw samples that enter the program one by one, with a shift of the baseline towards 0 (the same value is subtracted from all samples). The middle window shows the output of the deconvolution and differentiation process, for each sample that enters the recursive algorithm. The last window shows the result of the moving window averaging.

The main effect of the deconvolution is to extract the height of the pulse. In the figure it can be seen how the curve in the middle first rises quickly and

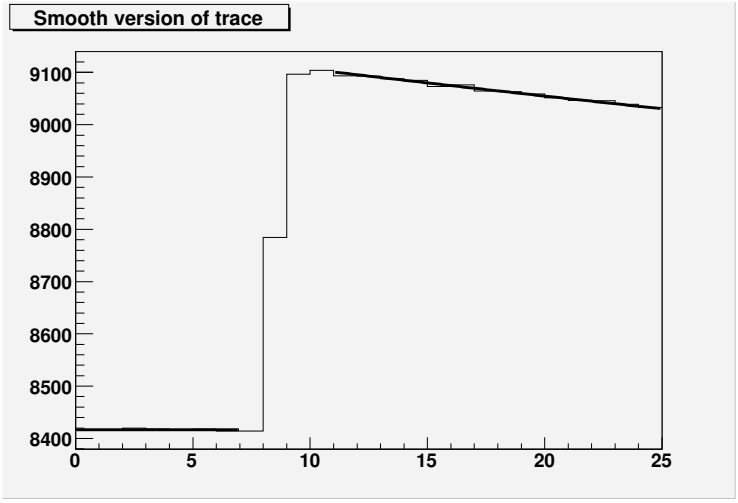

Figure 4.14: *An averaged version of the trace - the average of groups of 10 samples have been calculated. The two lines represent the two functions that were fitted to the data; one for the baseline and one for the exponential slope.*

then stabilises around a value which is the same as the height of the incoming pulse. The value for the time constant, τ, is chosen to be 50 μs in the displayed figure.

The second effect seen in the middle figure is the effect of the "differentiation". The value of the function at a given point is the value that results from the deconvolution operation, minus the result of a previous deconvolution operation at a point that is M samples before. This means that for the first part of the pulse, the value subtracted is a small number (0 if the baseline is perfectly compensated), as it is taken from a point that is earlier than the arrival of the pulse. However, when the difference between the two points that are being subtracted is such that both of them are from times after the arrival of the pulse, the values cancel each other. This gives the effect of cutting the pulse after a time span that is (almost) equal to the time difference M between the two samples to be subtracted.

The last curve shows the final outcome of the algorithm. In the last step, a moving window average is applied. For every point, an average is calculated over the previous L samples, where L is a constant. As the input pulse is approximately rectangular, the result of a moving window average is a trapezoid with a flat top of length $M - L$. The height of this function does, for adequately chosen constants τ, M and L, give an accurate measure of the energy. The height is extracted by taking an average over some fraction of the flat top, and from this subtracting the average of some fraction of the baseline. The regions over which the function is averaged are determined from when some threshold is passed.

Several different parameter settings were tested, and an energy spectrum from the one giving the best resolution is shown in Figure 4.16 together with the corresponding energy spectrum from the standard electronics. A selection

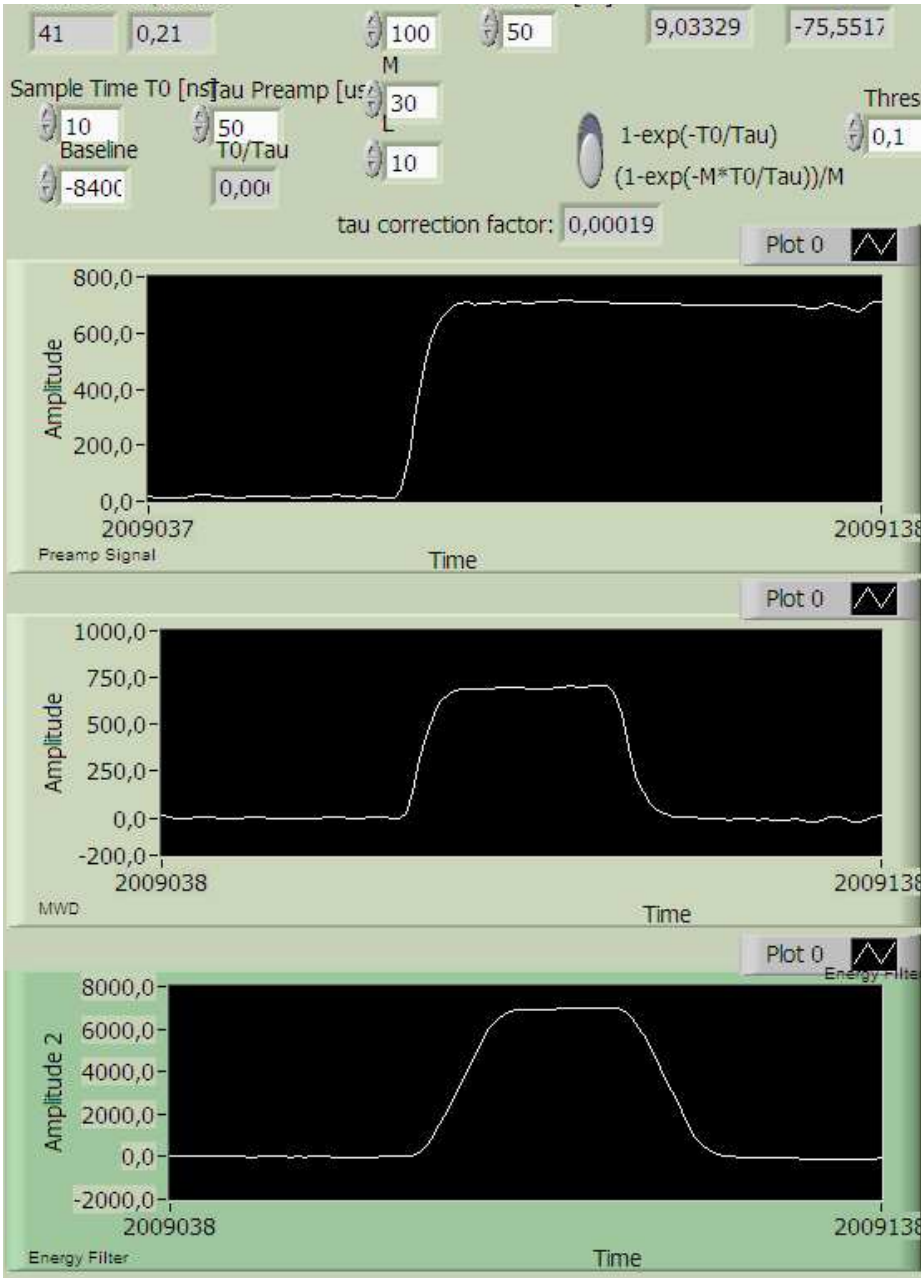

Figure 4.15: *The moving window deconvolution acting on a pulse. The uppermost window shows the raw trace, the second window shows the result of the deconvolution and differentiation and the last window shows the final output after the moving window average has been applied.*

of the parameter settings are displayed in Table 4.1. First, some attempts with a time constant of $\tau = 50$ μs were tried, as they seemed to flatten out the exponential part of the pulse to a straight line, at least when the first part of the pulse was considered. This is illustrated in the Figure 4.15, and the achieved energy resolution was approximately the same at that for the second version of the energy filter ($\sim$80 keV). As the resolution was reasonably good, it was first believed that a region of parameters that would give the best resolution had been reached, and that small variations around these settings would give the optimal resolution. Therefore, several different attempts to fine tune the parameters were made. However, the resolution stayed the same for small variations in both τ and M variations.

It was also noted that changing τ and M a lot did not change the resolution very much either, as displayed in the second row in Table 4.1. The reason for trying $\tau = 13$ μs was that this is the time constant that can be extracted from fitting exponential functions to the traces (a_2 from Eq. 4.1 being -7.78 $\cdot$ 10^{-4} is equivalent to τ being 13 μs). This did not, however, agree with any expectations - the time constant for the preamplifiers is specified to be 27 μs, and the first attempt with the MWD seemed to indicate that 50 μs gave the best treatment of the pulse.

Since the resolution stayed the same almost regardless of the parameters chosen, something was clearly wrong. A completely different setting, in which a much larger fraction of the pulses was considered, was tried a well. The pulses were processed with parameters that took into account the entire pulse, which means that the M value was increased as much as possible, and the L value was increased accordingly. Doing this, it was noted that the dependence of τ was now clearly visible, and a value of about 13 μs gave the best flat top. Also the averaging done in the last step of the algorithm, when the values of the flat top and the baseline are picked out, was made over larger regions that became available when the entire pulse was used. In order to make the algorithm work properly, the recorded pulses were not put directly after each other, but the baseline was artificially prolonged so that the algorithm had time to stabilise after the abrupt change between the concatenated traces.

The first attempts to use the MWD algorithm, where the dependence on τ was hardly visible, point towards the beginning of the pulse being more or less independent of the time constant. This might well be true, as the beginning of the pulse can still be affected by the rise, and also that the algorithm needs longer time in order to stabilise (see Chapter 2/Figure 2.4).

The last versions of the MWD that were tried, using as much as possible of the exponential decay, are displayed in the last rows of the table. The resolution achieved using these parameters was the same as that for the standard electronics, i.e. about 60 keV. A minor variation to $\tau = 12$ μs was also tested, but this gave the same resolution.

As was seen in the tests of the different parameters, the resolution could be greatly enhanced by considering the entire traces that were recorded. Since the shaping time of a conventional shaping amplifier is analogous to the M value of the MWD algorithm, and commonly used shaping times used for silicon detectors are on the order of several μs, it is possible that the resolution can be increased even further by considering a longer period of the exponential decay.

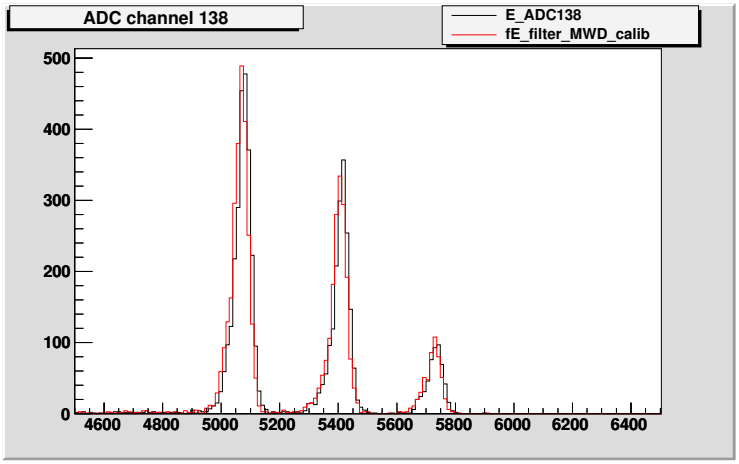

Figure 4.16: *Calibrated energy spectra extracted using the MWD algorithm with the parameters τ = 13 μs, M = 1.6 μs, L = 0.6 μs, and an average over 0.7 μs on the flat top and an average over 0.35 μs for the determination of the baseline (red) and from standard electronics (black).*

τ	M	L	Baseline	Flat top	Peak 1	Peak 2	Peak 3
50	0.3	0.1	0.3	0.06	80	78	75
13	0.6	0.1	0.3	0.06	82	85	75
13	1.6	0.6	0.35	0.7	61	59	61
12	1.6	0.6	0.35	0.7	61	59	61

Table 4.1: *The energy resolution of the MWD algorithm using different sets of parameters. The column "Baseline" refers to the length of the period over which the baseline was averaged, and the column "Flat top" refers to the time over which the flat top was averaged. The MWD parameters are given in the unit μs and the resolution is given in keV.*

4.3 Comparison of standard electronics and digital filtering

4.3.1 Agreement between different methods

Figure 4.17 shows the correlation between the standard electronics and the first version of the energy filter; the x-axis is the value of the energy extracted from the standard electronics and the y-axis is the corresponding value, for the same event, from the digital filter using the difference between the maximum and the minimum value.

The requirement on the events shown in the top spectrum is that they must have a non-zero energy according to the standard electronics. This spectrum shows that all those events that according to the standard electronics had a high energy, also gave a very similar energy in the energy filter. This is important to verify, as the digital filtering should not miss any of the events seen by the standard electronics. In the lower left corner of the spectrum, a group of events that are not interpreted in the same way by the standard electronics and the offline treatment of the pulses are seen. Those are the events interpreted by the standard electronics as pulses with very low energy, but according to the filter, the energies are higher. These events can be, for example, events that were just above the threshold of the standard electronics, and whose energies are strongly overestimated by the simple filter.

In the bottom spectrum in Figure 4.17, there are no conditions at all on the events. In this spectrum all the events that had no energy according to the standard electronics show up along the y-axis. The events that have somewhat higher energies in the filter than the threshold of the standard electronics are expected, due to the overestimation of the energy using the simple energy filter. However, the events that had nothing in the standard electronics but energies of several MeV in the digital filter are unexpected, as they might seem to imply that the standard electronics is missing some of the events.

Traces that corresponded to a high energy according to the filter but not according to the standard electronics were examined. Some examples of these traces are shown in Figure 4.18. These traces are clearly not from detection of particles, but contain just noise with very high amplitudes. These events are obviously rejected in the standard electronics, but not in the simple energy filter. This shows that the first energy filter is not an acceptable method for extraction of the energies.

The performances of the other energy filters with respect to this feature were investigated by counting the number of events in a strip that corresponded to an energy of above 5 MeV in the digital energy filter but had zero energy according to the standard electronics. For the first version of the filter there were 114 such events. For the second energy filter, which uses an average for the baseline, only 7 of those remain. In the case of the third version with the filter, there are no events of that kind left, indicating that those choices are much better in the perspective of excluding high-amplitude noise.

The distributions of energies in the peaks from the α particles as seen in Figure 4.17 are narrower in the x-direction than the y-direction, illustrating once more the less good energy resolution of the first version of the energy filter as compared to the standard electronics. In Figure 4.19, the first and the third

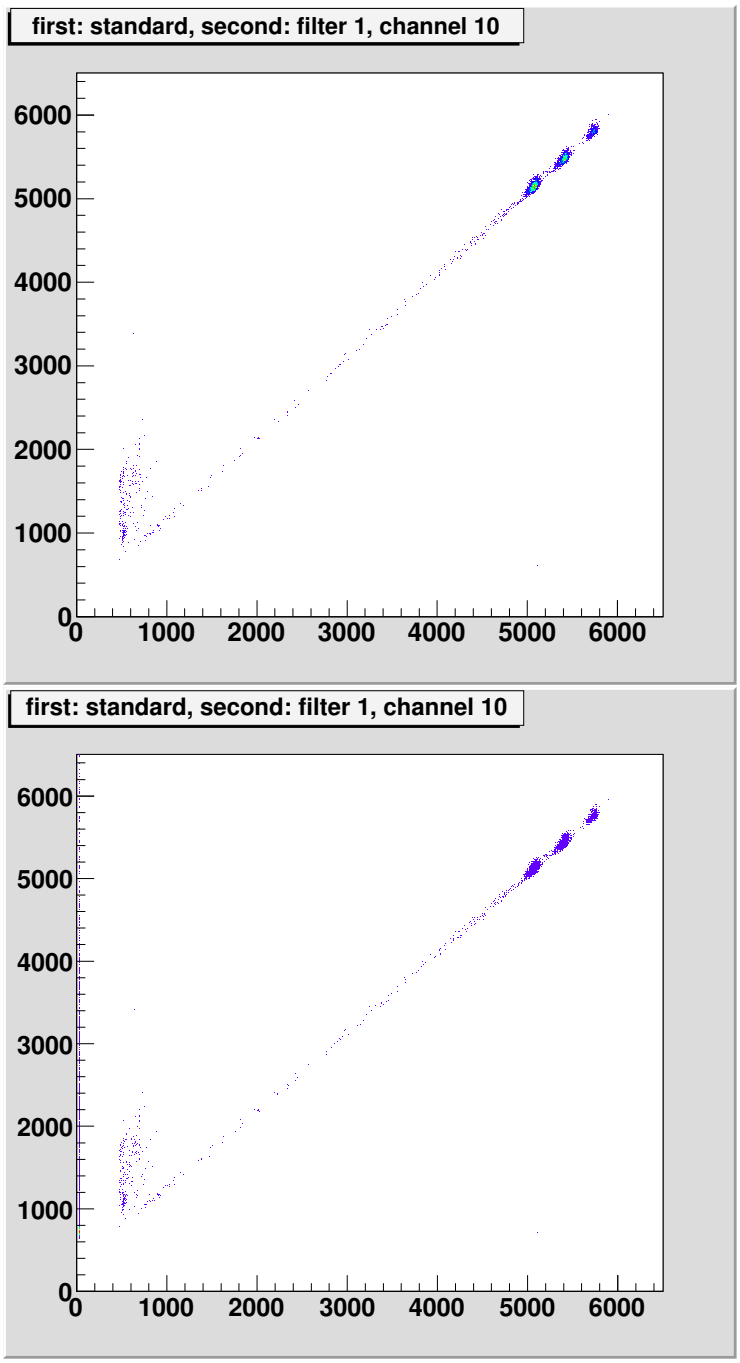

Figure 4.17: *Top: Spectrum showing the energy from the standard electronics on the x-axis and the energy from the first version of the energy filter on the y-axis. The events are from one strip only, and the only events that are displayed are those that had a non-zero energy from the standard electronics. Bottom: Same spectrum as above, but showing all the events from that strip, regardless of whether there the standard electronics detected anything or not.*

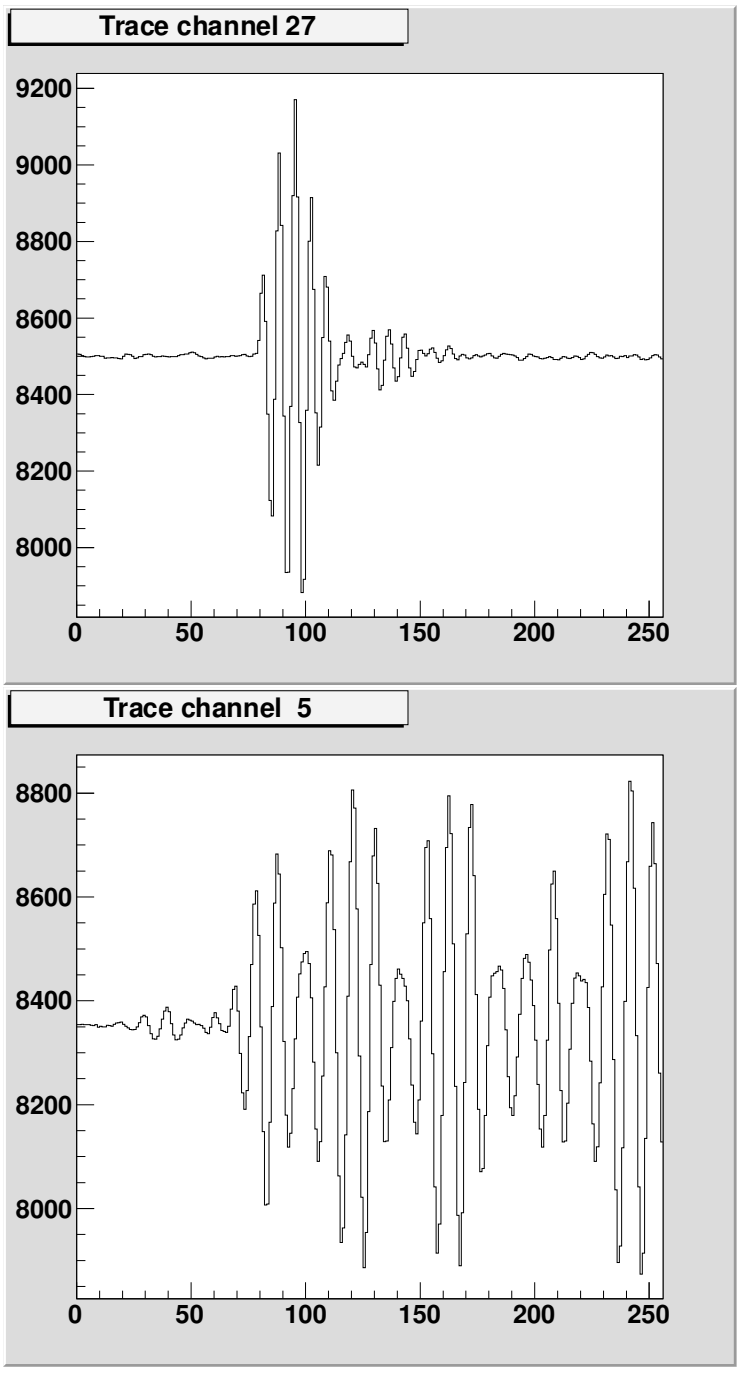

Figure 4.18: *Traces of events that yield high energies in the first filter, E_1 but zero energy in the standard electronics. The energies according to energy filter 1 are above 5 MeV.*

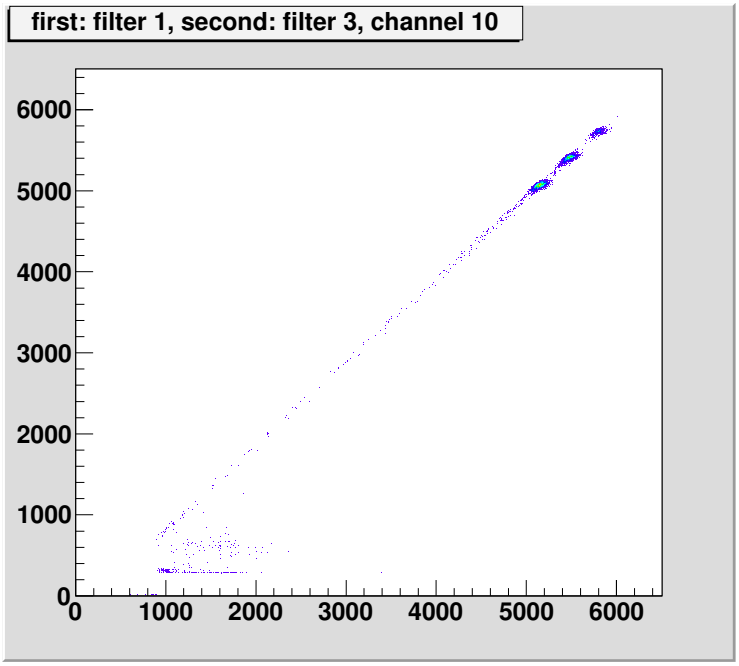

Figure 4.19: *Spectrum showing the energy from the first filter on the x-axis and the energy from the third version of the energy filter (with fixed slope) on the y-axis. The events are from one strip only, and the only events displayed are those with a non-zero energy from the standard electronics.*

energy filter are compared. The requirement imposed on the events is that the standard electronics must have a non-zero energy in the strip. The peaks from the α particles are clearly more separated in the y-direction than in the x-direction, due to the improved resolution of the third energy filter. The off-diagonal events are most likely the same events as those that were off-diagonal in the top spectrum of Figure 4.17; they do not give any energy in the standard electronics, but according to the first energy filter they have energies of up to about 2 MeV. When these events are analysed by the third energy filter, the energy is once more found to be smaller than what the first filter indicates. The sharp lower cut-off is because of the energy filter 3 not being employed unless energy filter 1 was above a certain lower limit.

4.3.2 Resolution

The resolution of the different energy filters were compared by fitting Gaussian functions to the α peaks, and the FWHM was calculated as FWHM $= 2.35 \cdot \sigma$. The resulting resolutions, for two different strips - one on the p-side and one on the n-side, are summarised in Table 4.2.

The resolution of the energy filters is gradually improving as the methods are refined, when going from the first and simplest version of an energy filter to the version which included the fitting of a function to the exponential slope. The further developments of the last method included a fixing of the parameter

Energy filter	Peak 1, p	Peak 2, p	Peak 3, p	Peak 1, n	Peak 2, n	Peak 3, n
Standard	61	59	61	63	63	61
Filter 1	99	96	89	85	89	89
Filter 2	82	82	78	80	78	78
Filter 3	66	63	63	68	68	68
Filter 3, fixed slope	61	-	61	61	-	61
Filter 3, fixed slope, smooth	61	59	59	61	61	61
MWD, best parameters	61	59	61	-	-	-

Table 4.2: *Energy resolution of the different versions of digital filtering of the traces, compared to that of standard electronics. "Peak 1" refers to the first and highest peak in the histograms with an energy of 5070 keV (from the ^{240}Pu), "Peak 2" refers to the middle peak with an energy of 5410 keV (^{241}Am) and "Peak 3" refers to the last peak at 5730 keV (^{244}Cm). "p" and "n" refers to the side of the detector. The resolution is given as the FWHM of the pulse in keV.*

of the exponential slope, and this version has a resolution that is as good as the one of standard electronics, which shows that it is possible to achieve at least as good resolution using sampling ADCs as standard electronics. In a last version of this filter, an averaging of the function was made before the fit was made. This did not change the resolution significantly.

The first attempts to use the MWD algorithm gave an energy resolution that was comparable to that of the second version of the energy filter, but using a longer part of the exponential decay enabled both a better determination of the time constant of the preamplifier, and a better resolution about the same as that of the standard electronics. This illustrates clearly that the parameters used in the MWD algorithm need to be finely tuned in order to get a good resolution. Possibly, the resolution can be even better if the parameters were further optimised. However, the similarities in the processes that are employed in the last version of the "offline" energy filter and the MWD algorithm, indicate that most likely the resolution should not be very different for the different methods. As the resulting resolutions for the two methods agree very well, it seems likely that the resolution from the MWD cannot be improved very much more by fine tuning the parameters. What could, however, improve the resolution is the length of the exponential tail that is considered. For this experiment, only about 1.5 μs of the tail was recorded. By operating on the real data stream from the detectors, this period can be prolonged, which could possibly enhance the resolution.

The tests performed show unambiguously that the same resolution can be achieved for sampling ADCs as for standard electronics, using either an offline analysis of the data or by applying the MWD algorithm with carefully optimised parameters to the stream of data from the detector. This means that it is indeed possible to replace the standard electronics for the DSSSD of the TASISpec setup with sampling ADCs without any loss of energy resolution.

Chapter 5

Experimental Results: Implications for New Opportunities

New possibilities, besides the prospects of improved energy resolution, open up with the use of sampling ADCs. Access to the pulse shape may yield information about the formation of the pulse, which, in turn, may transform into information about the detected particle. This new aspect will be investigated in this chapter.

5.1 n-side/p-side rise time

If there is any relevant information in the pulse shapes, besides energy and time, it resides within the rise of the pulse. The measurement with the α source was used for characterisation of different methods to parametrize the rise of the pulse, and then the methods were applied to the in-beam data in order to investigate the possibilities of particle identification.

5.1.1 Fitting of a straight line to the rise

The first attempt to characterise the rise of the pulse was made by fitting a linear function to a small portion of the middle of the rise. In order to determine what region to use, the derivative of the function was constructed. The difference between two subsequent samples was calculated and used as the derivative. Two pulses, one positive and one negative, and their derivatives, are shown in Figure 5.1. The position of the pulse can be taken as the maximum of the derivative. This gives a more accurate positioning than, for example, by using the the maximum of the trace itself. This is due to the noise; even in cases of a real pulse being detected, the maximum of the pulse is not necessarily positioned directly after the rise since noise on top of the pulse may shift the maximum, whereas the derivative is most likely large only for the rise of the pulse.

The linear function was fitted to a small region around the bin with the highest value of the derivative, using the data from the α source. Figure 5.2 shows the result of the fit for two of the traces, one positive and one negative.

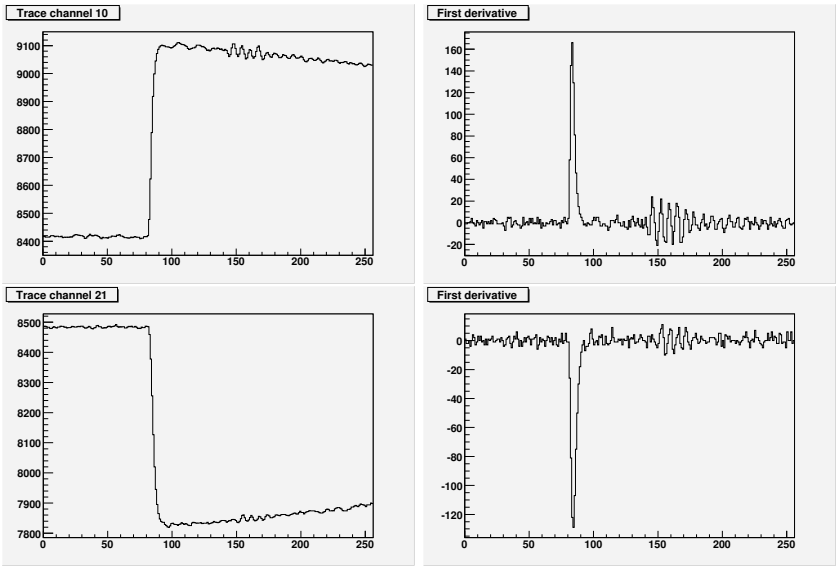

Figure 5.1: *The same traces as displayed in Figures 4.4 and 4.5, now together with their derivatives. The derivatives were calculated as the difference between two consecutive samples.*

The rise itself is not a linear function except for the middle of the rise where a line is a reasonable approximation, and hence this method may be unstable, as it depends strongly on exactly which region is chosen. The parameter from the fit which describes the slope is shown in Figure 5.3 as a function of energy for two strips. Most of the events end up along a line with a well-defined slope, and the three α peaks are seen to end up on this line. The spread of the values is not very large along this line, which indicates that this simple method is, in fact, rather reliable. The fact that the slope depends linearly on the energy for the α particles, means that the rise time is a constant, while the slope varies in order to give different energies. In order to verify the linear dependence of the slope on the energy, the slope was normalised with the energy of each event. The results for the p-side strip is shown in Figure 5.4. The slope normalised with energy shows similar distributions for the three different peaks, which shows that the slope is indeed linearly dependent on the energy for the same type of event. However, it should be noted in the spectra that the normalised peaks are not in the same positions for the p- and n-side. The normalised slope on the n-side is a little smaller than the one from the p-side, which indicates that the rise time is somewhat longer for the n-side. This is due to the longer time it takes for the charge cloud to travel to the n-side of the detector, which allows for more diffusion to take place. However, the figures indicate that this does not affect the linearity in energy, but just causes the slopes to be smaller.

The points in Figure 5.3 that are not on the main line may seem like a worrying feature. However, it turned out that they all originated from events with multiplicity higher than one. Figure 5.5 shows the events with a total multiplicity of one for each side, that are recorded in a strip on the p-side. In

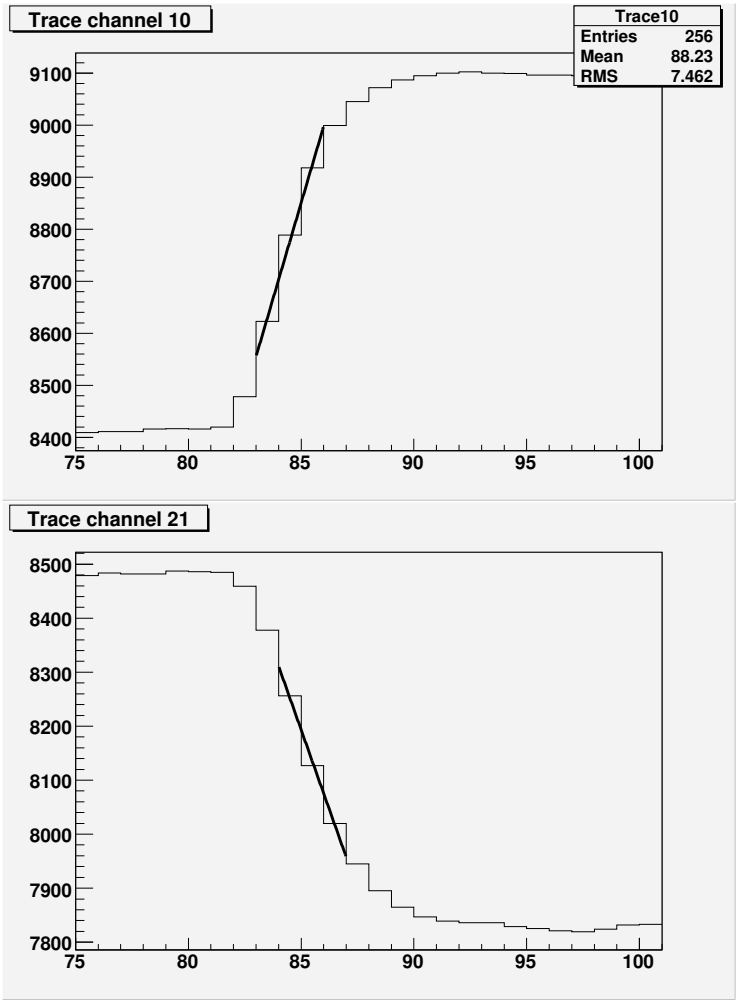

Figure 5.2: *Illustration of the fitting of a linear function to the middle part of the slope. The region for the fits goes from bin* $b_1 = b_c - 1$ *to bin* $b_2 = b_c + 2$ *where* b_c *denotes the extremum bin of the derivative.*

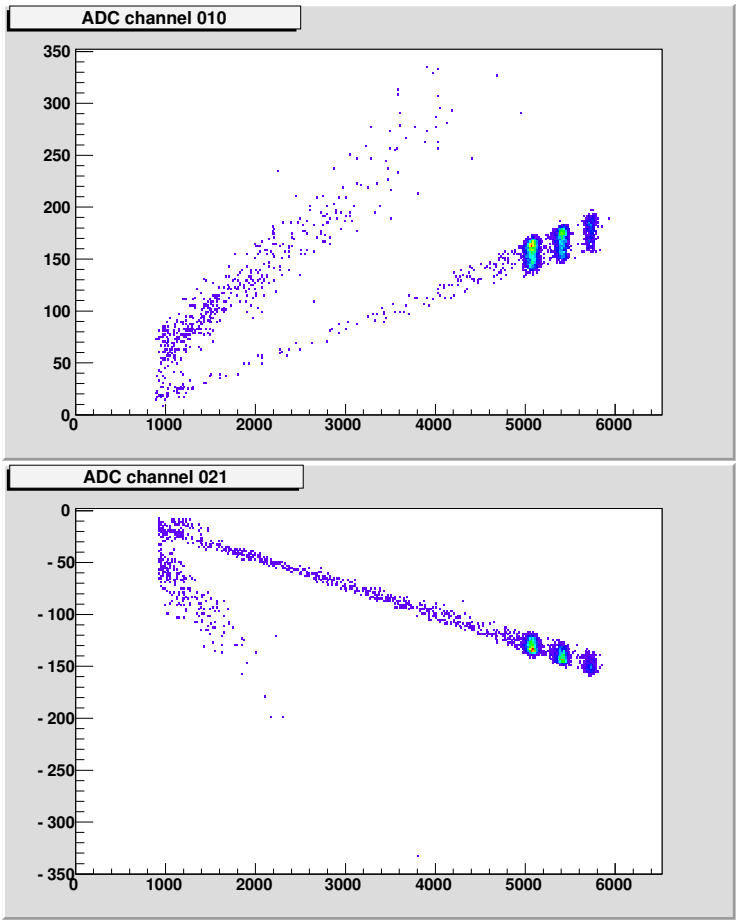

Figure 5.3: *Slope found from fitting a linear function to the central part of the rise as a function energy for two strips. The region to which the fit was made extended from bin $b_1 = b_c - 1$ to bin $b_2 = b_c + 2$ where b_c denotes the extremum bin of the derivative. Only those events having an energy in excess of $\sim$0.8 MeV in the third energy filter are displayed.*

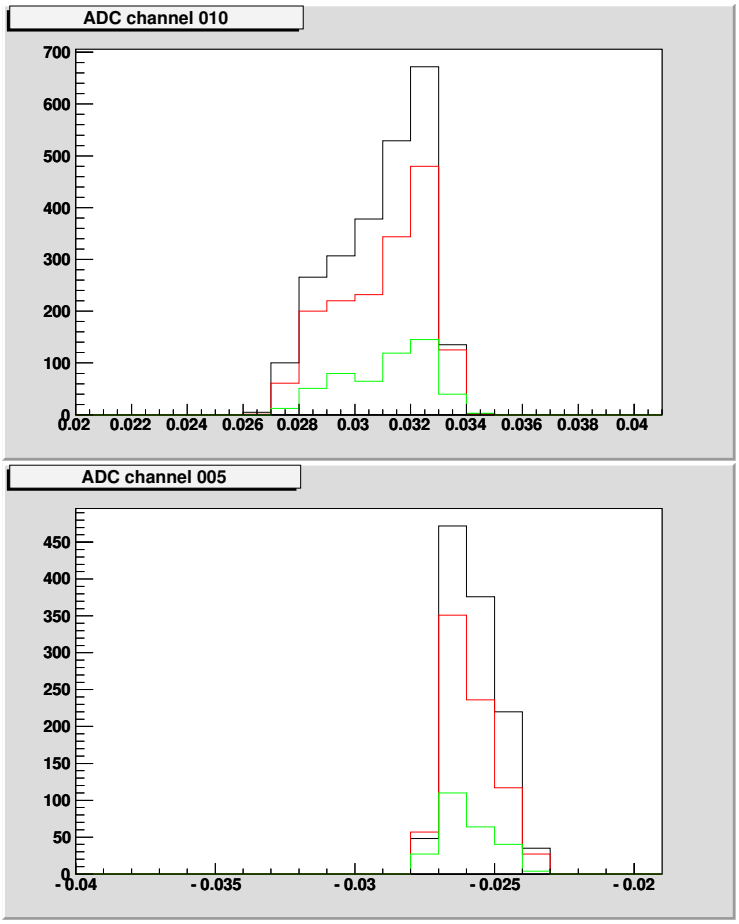

Figure 5.4: *Distributions of slopes divided by the energy of the pulse, for a p-side and an n-side strip. The black curve corresponds to the peak with the lowest energy, the red to the one with intermediate energy and the last to the peak with the highest energy. The data displayed is from the same strips as the previously displayed data.*

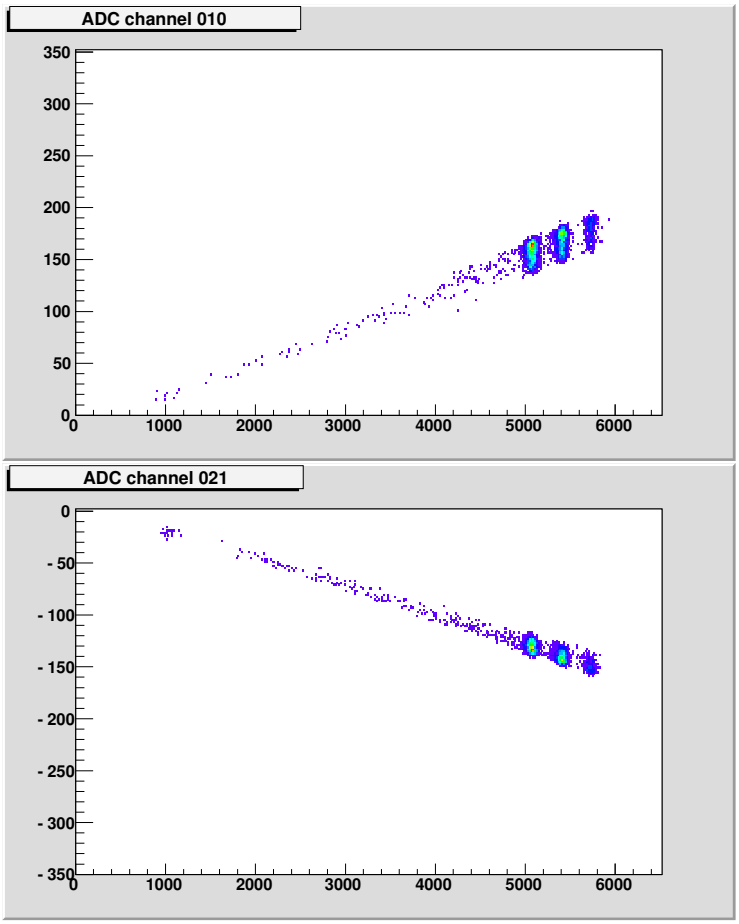

Figure 5.5: *Slope as a function of energy, for a strip on the p-side and one from the n-side. The events are restricted to contain only those that have multiplicity 1 in both p-and n-side.*

this spectrum, the events all end up on the same line. The multiplicity being 1 means that the strip which is considered contains one and only one well-defined pulse of a height that corresponds to about 0.8 MeV or more. As these are the events of interest to examine, the analysis of the slope will from now on be concentrated on those events that have multiplicity 1 in both sides only.

In principle, there may be some differences in the response of the detector as a function of position. To investigate this, the events from one pixel only were investigated. Figure 5.6 shows the distribution of slopes divided by the energy for each of the three α peaks. The distributions are very similar to those from the entire strips, as seen in comparison to Figure 5.4. This indicates that there is no large difference between different parts of the detector from a point of view of the slope of the rise. The use of the slope for possible particle identification will be discussed later in this chapter.

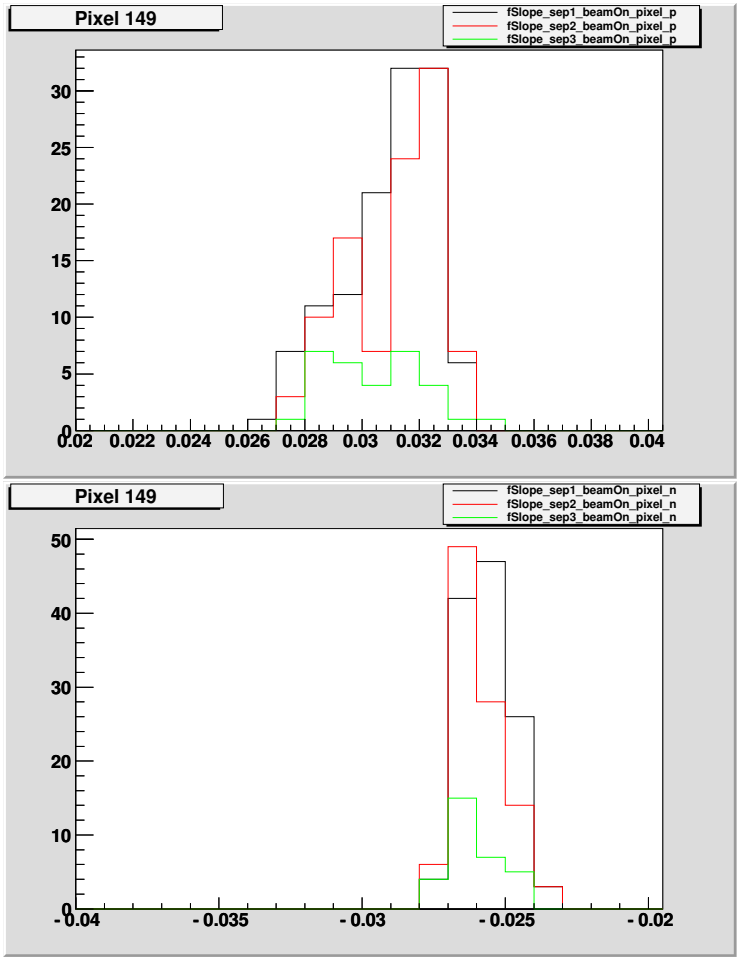

Figure 5.6: *The distributions of slopes for the p-side (upper) and n-side (lower), separated into the different α peaks.*

5.1.2 Calculation of time and width of the derivative

Another approach for the parametrisation of the pulse shape was tried as well. This uses the features of the derivative; the mean value of the derivative is taken as the time for the arrival of the pulse (also used for the last versions of the digital energy filter in section 4.2.2). Also an attempt to characterise the rise time using the width of the peak of the derivative of the pulse (cf. Figure 5.7) was made. The mean bin value, denoted by T (for time) is calculated as

$$T = \frac{1}{N} \sum_{i=b_1}^{b_2} i \cdot |N_i|, \tag{5.1}$$

where the sum goes over a chosen interval $[b_1, b_2]$ of bins around the rise of the pulse. N_i is the contents of bin i and N is the normalisation constant

$$N = \sum_i |N_i|. \tag{5.2}$$

The width of the rise is taken as the standard deviation of the peak on the derivative, calculated as

$$\sigma = \sqrt{\frac{1}{N} \sum_{i=b_1}^{b_2} (i - T)^2 \cdot |N_i|}, \tag{5.3}$$

where T is the mean bin.

Calculation of the time

A first attempt, in which the time was calculated using the derivative itself and not the absolute value, gave inconsistent results due to the varying signs of the weights; the mean value was sometimes found to be outside of the range over which it was calculated. If those events that had multiplicity one, i.e. those that for sure contained an event at the self-trigger time which is inside the range that was used for calculating the mean value, the mean values were all found within the range. In principle, the only events investigated in this section are those with multiplicity one, since they are the events where the time of the arrival is approximately the same, but the inconsistency in the results points towards a problem with the method which should be fixed in order to have a stable algorithm. Therefore, the absolute value of the derivative is considered for the determination of the weights used in the calculation of the time. This also gives a more consistent way of treating pulses from either side of the detector.

Figure 5.8 shows the time as a function of energy, for all events with multiplicity 1 in both p- and n-side, for one strip on the p-side and one on the n-side. The interval chosen for the calculation of the mean value covers the range $[b_1, b_2] = [65, 100]$ as indicated in Figure 5.7. The region extends approximately 10 units to both sides of the peak itself. Most events have similar times; for the events on the p-side, the average time is slightly below 83, and for the n-side, the average time is slightly higher. This is consistent with expectations; the detector is exposed to radiation close to the p-side, so the time it takes for the charge carriers to drift to the p-side is shorter than the time for the drift to

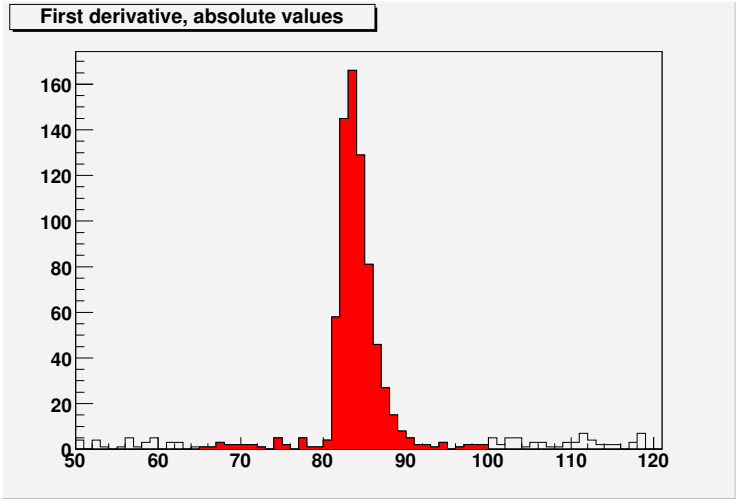

Figure 5.7: *The derivative from the same trace from the p-side as shown previously, but with absolute values of each bin begin displayed instead of the real value for the derivative. The region over which the mean bin was calculated is marked in red.*

the n-side. Of course, the differences in time depend also on the cable length, which could, in principle, shift the positions in time.

The distributions of the times divided into the three different α peaks is shown in Figure 5.9. In the upper part, the distributions from a strip on the p-side of the detector is shown, and the lower part shows a strip from the n-side. The distributions are clearly very similar for all signals detected on either side of the detector, independently of the energy. The average time from the strip on the p-side is determined to be approximately 82.7 and on the n-side the corresponding value is approximately 83.4. The difference between those values, 0.7 bins, corresponds to 7 ns.

A smaller region over which the mean value is calculated, $[b_1, b_2] = [75, 90]$, was tried as well. The results from the two regions are compared in Figure 5.10, where the distributions of times for the peak with the highest intensity are shown. The strong similarity of the two distributions is a good indicator of that the method is stable, at least in the sense that it does not depend critically on the chosen interval. Due to the larger possibility of accommodating also pulses that are not in self-trigger position in the largest interval ($[65, 100]$), it was decided to use this interval for the calculation of the time.

The importance of extracting the time for the arrival of the pulse, from the perspective of particle identification, is to be able to see possible differences between the p-and n-side of the detector, and how this changes with type of event. For the chosen method ($[b_1, b_2] = [65, 100]$), the distributions of time from the peaks with the highest intensity from one p-side strip and one n-side strip are shown in Figure 5.11. The difference between the mean value of the two distributions is approximately 5 ns.

So far, it has been shown that the calculation of the time does not depend on the chosen interval, and that the calculations do not give very large variations.

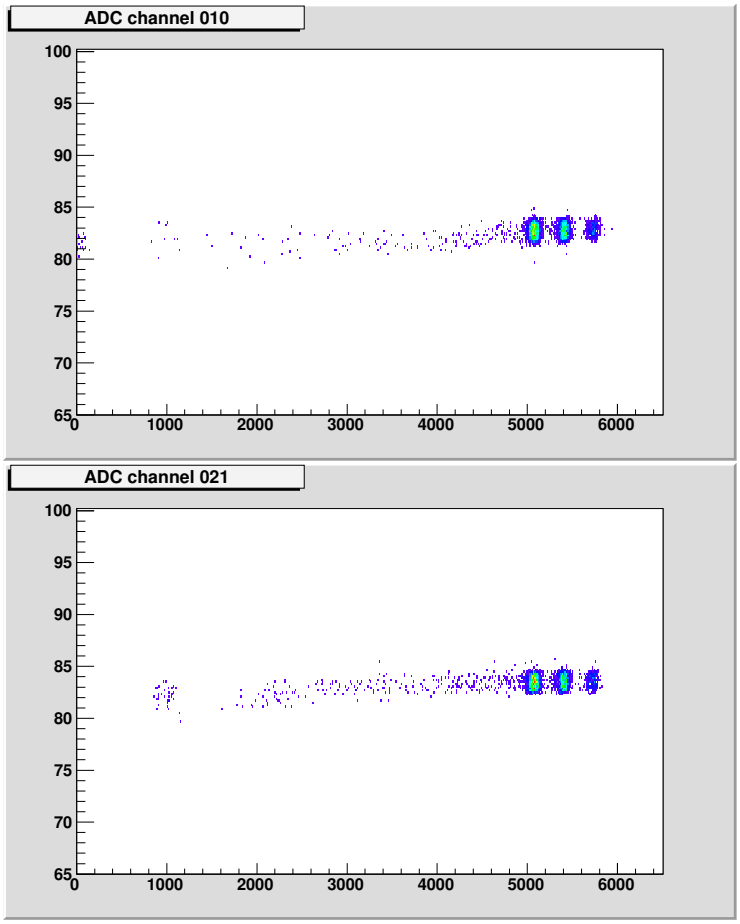

Figure 5.8: *The time as a function of energy for all events with multiplicity 1 in both p- and n-side, calculated as the mean bin in an interval* $[b_1, b_2] = [65, 100]$.

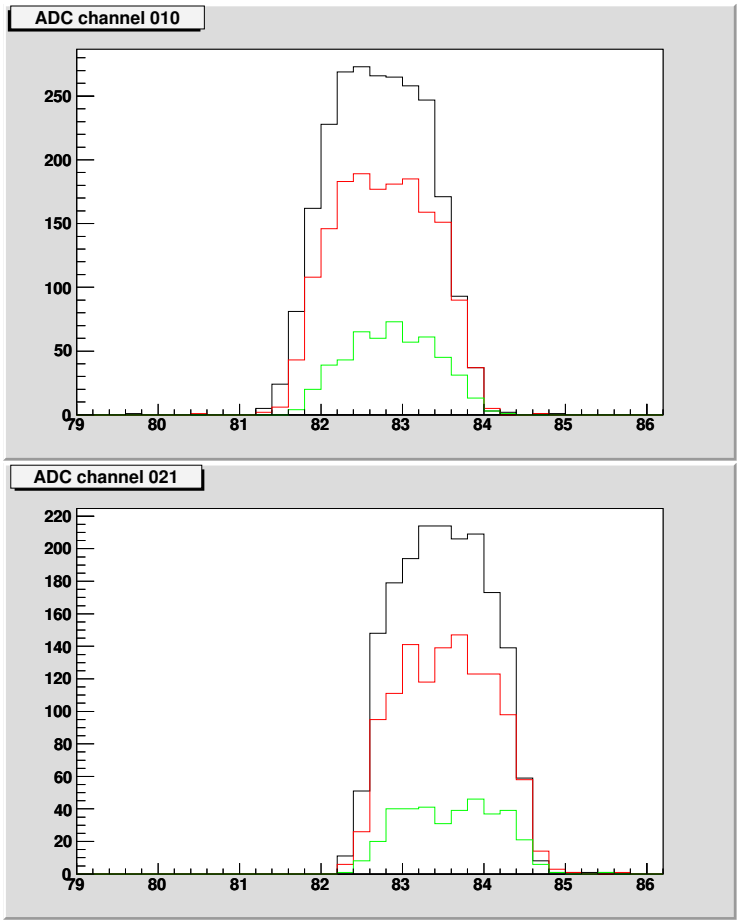

Figure 5.9: *The distribution of times divided into into different energy regions; the distributions shown in black are from the peak with the lowest energy, the red ones are from the middle peak and the green ones are from the peak with the highest energy. The upper part is from a strip on the p-side and the lower part is from a strip on the n-side.*

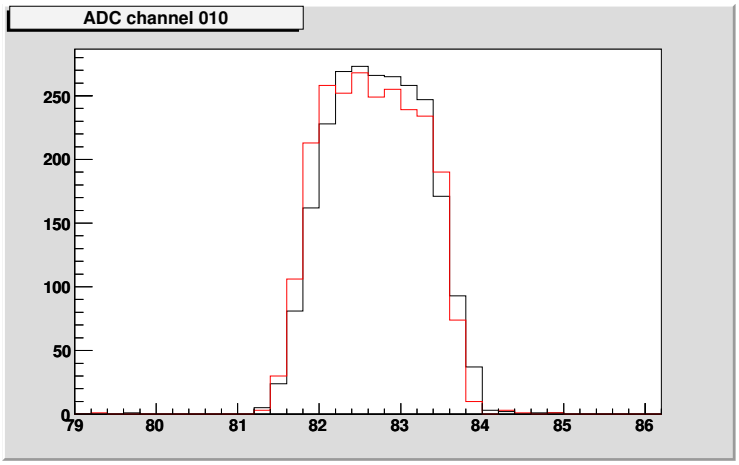

Figure 5.10: *The distributions of times from the peak with the highest intensity, shown for the larger region ($[b_1, b_2] = [65, 100]$) in black and for the narrower region ($[b_1, b_2] = [75, 90]$) in red.*

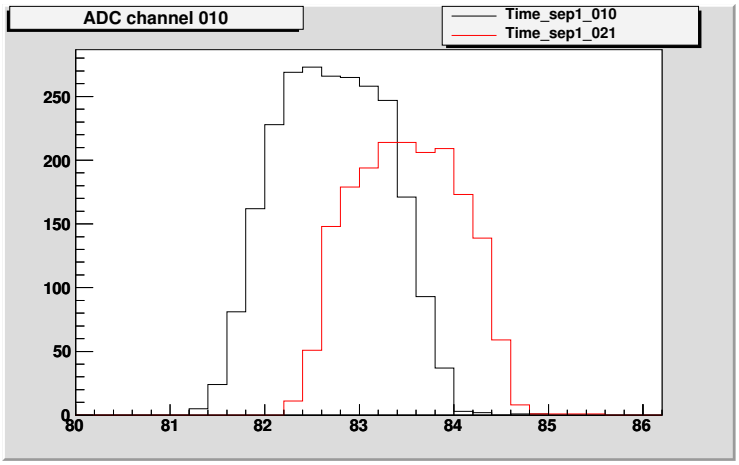

Figure 5.11: *The distributions of times for the peak with the highest intensity for the p-side (black) and the n-side (red).*

The variations in the times that persist are due to either (i) instability in the calculation or (ii) time jitter in the electronics system or (iii) that the pulses actually do arrive at the preamplifier/trigger system in such way that their relation in time is different from event to event. Since the physical situation is such that the difference in time between p- side and n-side should be fixed for a certain type of events if they happen within one pixel, the spread should most likely be due to one of the first two options. From Figure 5.11, it is a plausible assumption that the signal from the p-side always comes before the one from the n-side, but there is no explicit proof for it. In order to resolve these questions, the signals from one pixel were investigated.

Figure 5.12 shows the distribution of times for the three different α peaks from one pixel only. The pixel that is displayed here is the one that contains the two strips that the previous pictures are constructed from. The distributions of times are approximately as wide as for the full strips (see Figure 5.9), which indicates that the spread in time does not depend on variations between different parts of the detector.

The time as a function of energy for each side of the pixel is shown in Figure 5.13 together with the difference in time between the p-side and n-side for each event. The lower part of the figure shows that the signal from the p-side does not always come before the signal from the n-side. Even though this may appear a little odd, the absolute time difference is of no importance. A more worrying feature is that the spread of the values is rather large. Actually, it is larger than the spread of the values from the separate sides, as can be seen by comparing the three spectra in the figure. This is disappointing from the perspective of particle identification. One possible explanation for the large spread in the values in the figure would be that the method for calculating the time is instable. This was tested by visual inspection of sets of pulses from the outermost parts of the distribution of the time difference. Two such sets of pulses are shown in Figure 5.14; one in which the calculation gave a positive difference (p-side comes before n-side) and one which gave a negative difference. In the first set of traces, it indeed looks like the p-side signal comes first, and the other way around for the second set. This indicates that this unexpected feature does not originate from the calculation but is an inherent feature of the data.

This means that even though the calculation of the time can be done in a way that apparently is stable, the difference in time between the pulses is still rather large. This might be caused by the use of an external trigger, created in the analog electronics. The fact that the times differ rather much can make particle identification using this feature of the pulse a difficult task. The question of whether it is possible or not, will be addressed in the last part of this chapter. Other methods for extracting the time of the arrival of the pulse will be considered in the following sections.

Calculation of standard deviation

The calculation of the standard deviation was investigated in a similar manner as the time. At first, plots showing the standard deviation as a function of energy gave results that seemed reasonable. Figure 5.15 shows the standard deviation as a function of energy in the case when the absolute values of the derivative are used as the weights, and the region that is considered goes from bin 65 to bin 100. The standard deviation is seen to depend on the energy.

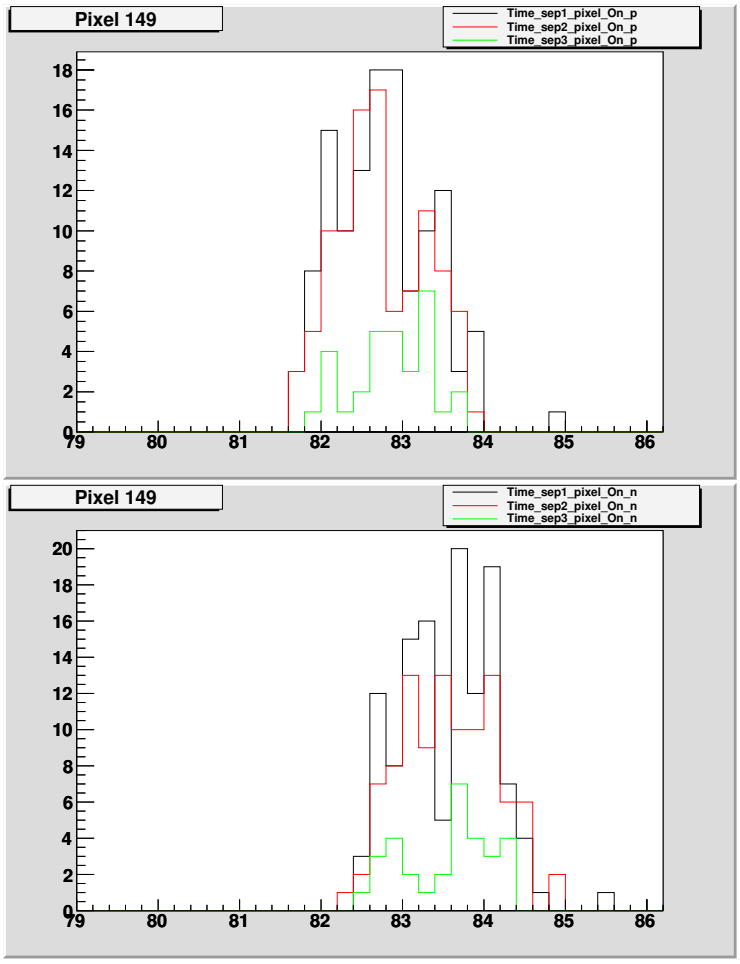

Figure 5.12: *The distributions of time for the three different α peaks from one pixel only. The upper spectrum is from the p-side and the lower spectrum is from the n-side. The separation into the different peaks is done such that the requirement for being part of either distribution is that both p- and n-side has an energy that is in the chosen interval for the respective peak.*

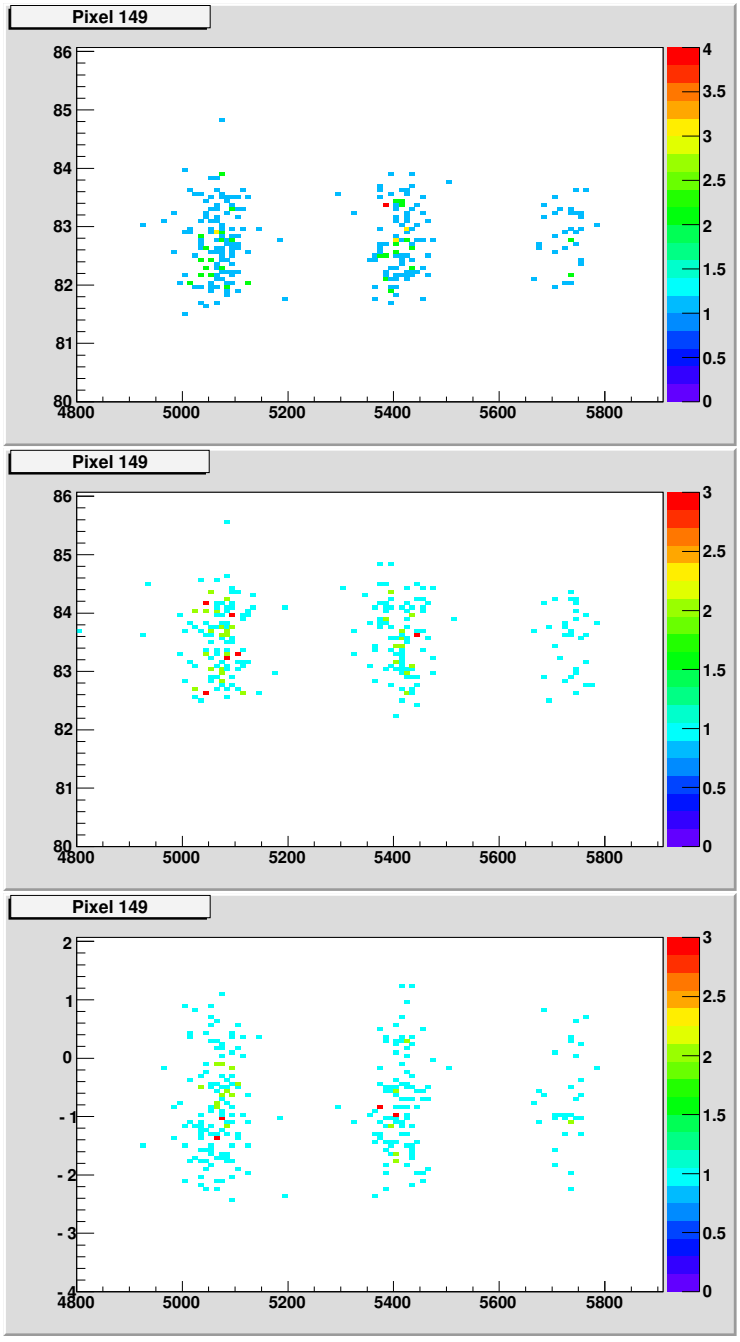

Figure 5.13: *The time for each event in the p-side (top) and n-side (middle) from one pixel, and the difference in time between those for each event (bottom) as a function of energy. Note that a multiplicity of 1 is required for both p-side and n-side, which ensures that the signals originate from the same event.*

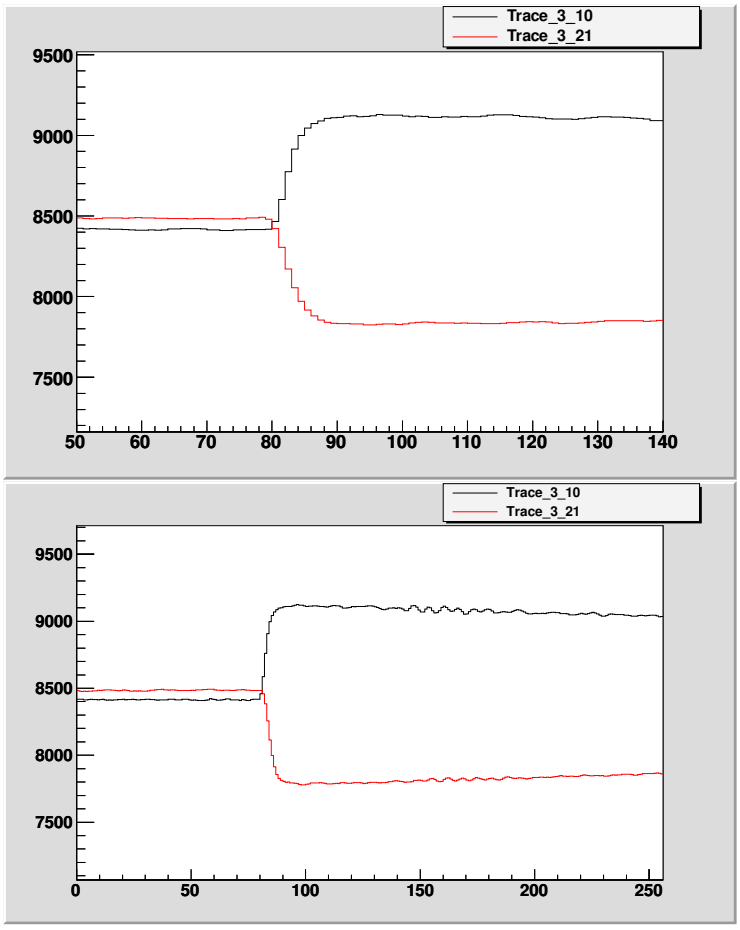

Figure 5.14: *Top: Traces from one event, for which the calculated time for the n-side is earlier than that from the p-side. Bottom: Traces from an event for which the calculated time showed a large time difference between the p-side and n-side, with the p-side coming first. Note that the scale on the x-axis is different in the two histograms.*

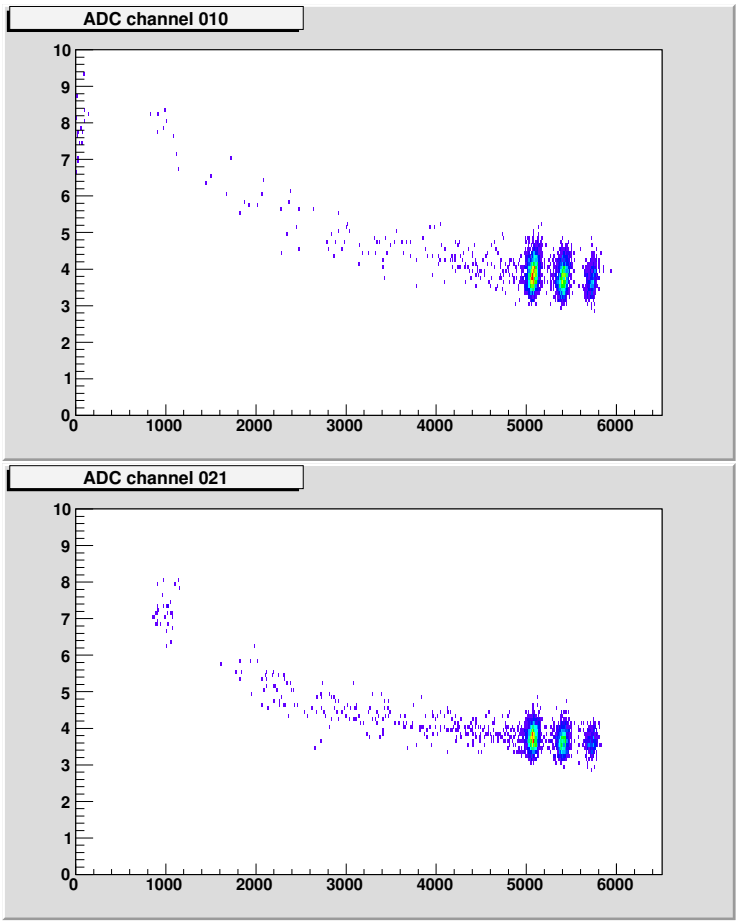

Figure 5.15: *Standard deviation calculated according to Eq. 5.3 as a function of energy, for one strip on the p-side (top) and one strip on the n-side (bottom).*

However, it does not seem to depend on whether the pulses are from the n-side or the p-side. Figure 5.16, in which the standard deviation is divided into the different α peaks, shows more explicitly the behaviour of the energy dependence. The higher the energy, the lower is the standard deviation. The expectation is that the rise time - and hence the calculated standard deviation - should not depend on the energy, as the slope has been shown to depend linearly on the energy. However, this is not necessarily inconsistent with the energy dependence observed for the width: Even if the rise time is equally long for all pulses, the height of the peak in the derivative will be higher for the pulses with high energy, and this affects the standard deviation of the pulse in the way that is seen in the spectra.

In order to investigate the method of determining the standard deviation further, the region over which it was calculated was varied. For a region between bin number 75 and 90, the result is quite different than for the larger region. The standard deviation as a function of energy is shown in Figure 5.17 for a

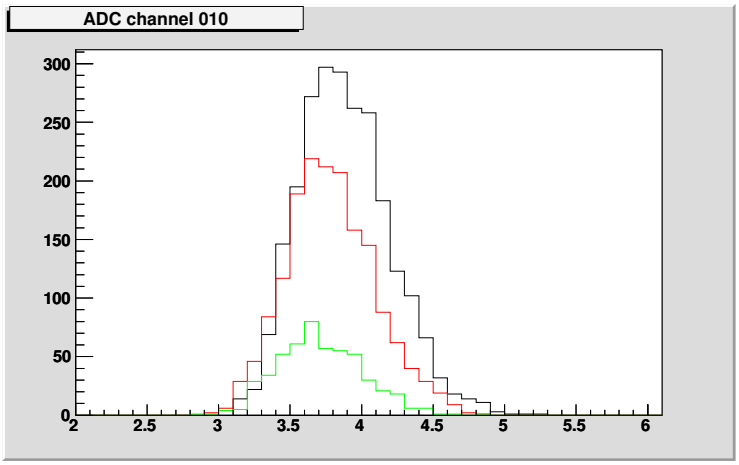

Figure 5.16: *Distributions of the standard deviation for the different peaks, shown for a strip on the p-side of the detector. The black is from the peak with lowest energy, the red is from the middle peak and the green is from the peak with the highest energy.*

p-side strip. The energy dependence is smaller in this case. However, the major difference is that the standard deviation is now distributed around values of 2 instead of values around 4, as for the larger interval. This dependence on the chosen interval is a worrying feature, which indicates that this method may actually not be very useful.

An even smaller interval, which goes from bin number 79 to 86, was investigated as well. Figure 5.18 shows the distribution of the standard deviation from the peak with the highest intensity for the different regions over which the standard deviation was calculated. The shape of the distribution varies a lot when going from the largest interval to the intermediate one, and the average standard deviation is also much larger for the larger interval. This dependence on the chosen interval shows that the method cannot be trusted, and it will not be considered further.

It should be noted that this does not imply that the width of the distribution is a quantity that is not useful, only that the method discussed in this section is not suitable for extracting this parameter. The dependence on the chosen region originates from the events far from the mean value of the distribution. Even though they are few, they obviously still affect the calculations significantly. Other methods for extraction of the widths will be considered in the next sections.

5.1.3 Using a Gaussian function to fit the derivative

Another possible method to extract the time and the rise time is to fit a function to the derivative and use the fitting parameters as measures of these quantities. A Gaussian function was fitted to the derivative, as illustrated for one trace in Figure 5.19. The parameter which gives the center of the distribution was taken as a measure of the time, and the width of the distribution was used as measure

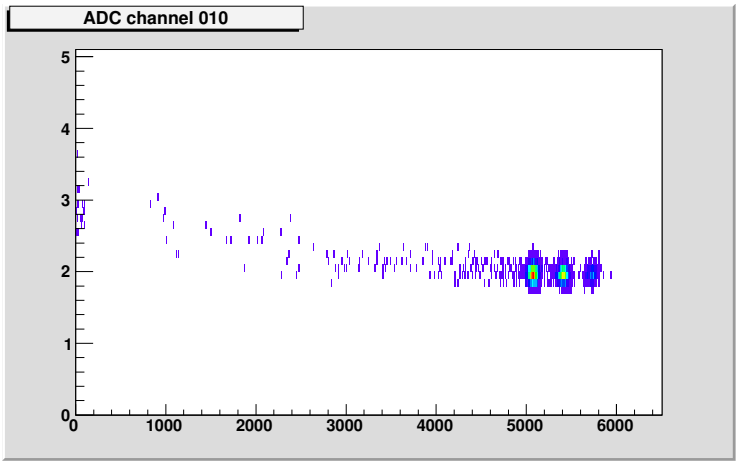

Figure 5.17: *Standard deviation as a function of energy for a p-side strip. The region over which the standard deviation is calculated is bin number 75 to 90.*

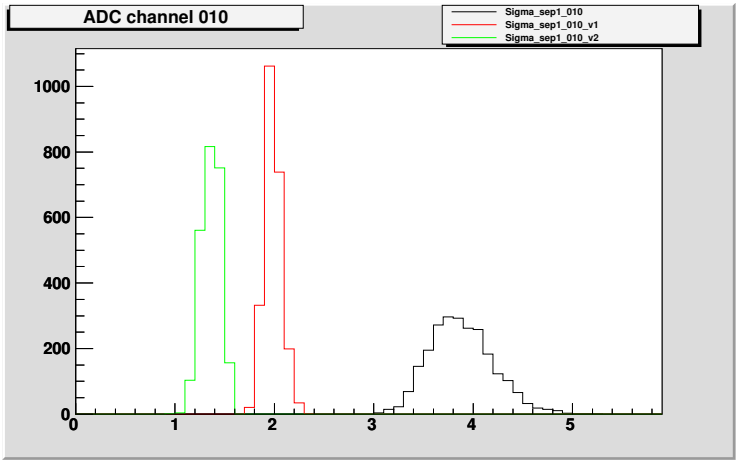

Figure 5.18: *Distribution of calculated standard deviation for the peak with the highest intensity, for different regions. The black curve shows the distribution that results from a calculation from bin number 65 to 100, the red curve corresponds to an interval of bin 75 to 90 and the green curve to an interval from 79 to 86 (see Figure 5.7 for a comparison of the intervals). The data is from a p-side strip.*

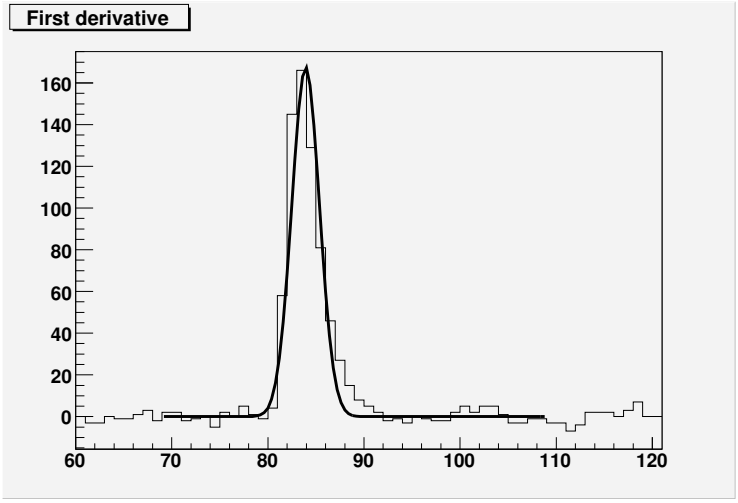

Figure 5.19: *Fitting of a Gaussian function to the derivative. The function was fitted over an interval* $[b_{min},b_{max}] = [b_c\text{-}15,b_c+25]$ *where* b_c *is the bin with the largest contents.*

of the rise time. Obviously, a Gaussian function does not represent the true form of the derivative, but nonetheless, it can provide a usable quantisation of the properties of the trace.

The resulting distributions of the time for the events from one pixel are shown in Figure 5.20 as functions of energy. The distributions for the time shows similar features as those calculated as the mean of the derivative (see Figure 5.13). The spread of the values is approximately the same for the different methods, which indicates that the spread is a feature of the data itself. The reason for the somewhat different position of the center of the distribution between the two cases is partly due to the fact that the Gaussian function does not agree with the peak due to the "tail" to the right, which pushes the centroid to the right as seen in Figure 5.19, and partly due to a different numbering of the bins of the derivative, which causes a shift of one channel between the different methods.

The widths of the fitted Gaussians are shown in Figure 5.21 as a function of energy for the same pixel. The distributions clearly show that the traces from the p-side have a shorter rise time than those from the n-side, as the sigma is smaller for the p-side. Also in this case, the distributions are well defined but wide.

5.1.4 Using two Gaussian functions to fit the derivative

To get a better fit to the peak than the simple Gaussian function employed in the previous section, a sum of two Gaussian functions was fitted to the derivative as illustrated in Figure 5.22. This clearly gives a better fit, however the parameters may be less straightforwardly connected to the features of the trace. The time for the pulse was taken as the centroid of the left Gaussian function, and the distributions of times as functions of energy are shown in Figure 5.23. Also in this case, the distributions are as wide as for the original method. Compared to

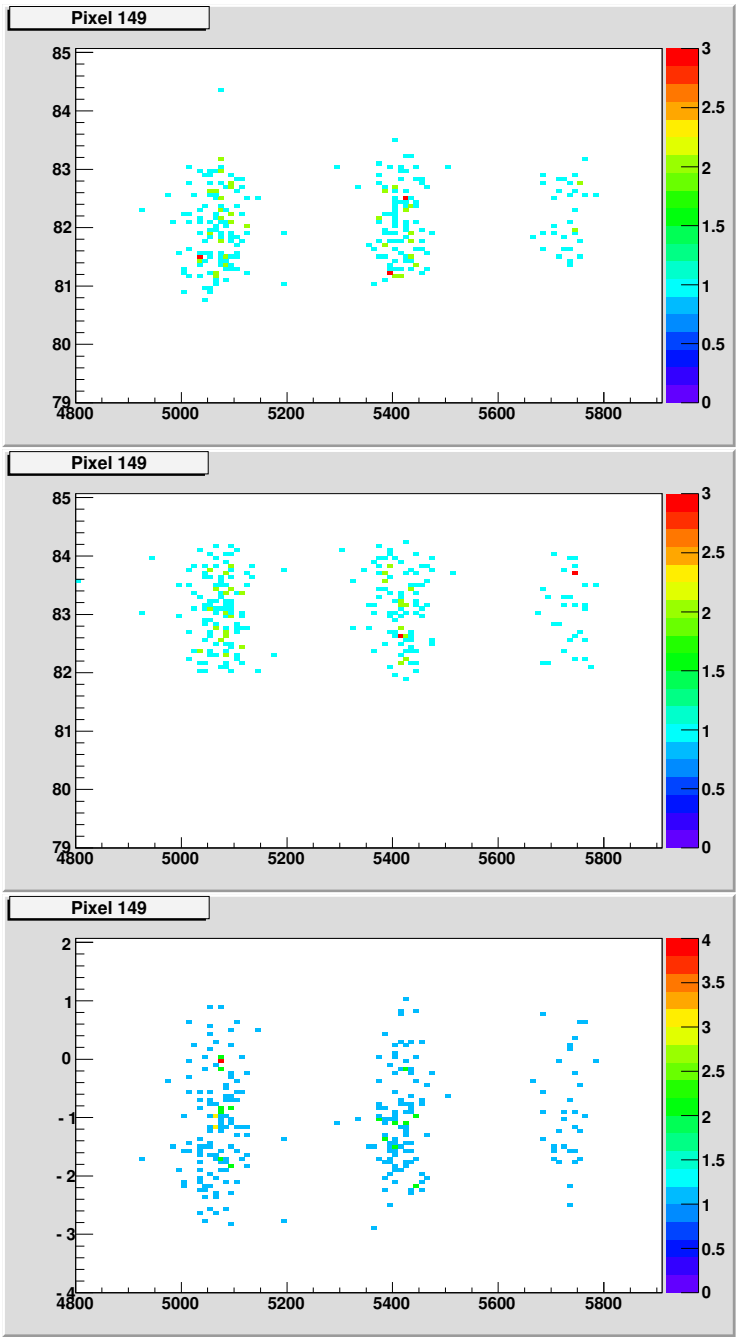

Figure 5.20: *Time as a function of energy for p-side (top), n-side (middle) and the difference in time between the two sides (bottom). The time is extracted by fitting a Gaussian to the function and using the centroid as the time. Note that the scale is the same as in Figure 5.13, although shifted with one unit, so that a direct comparison of the distributions can be made.*

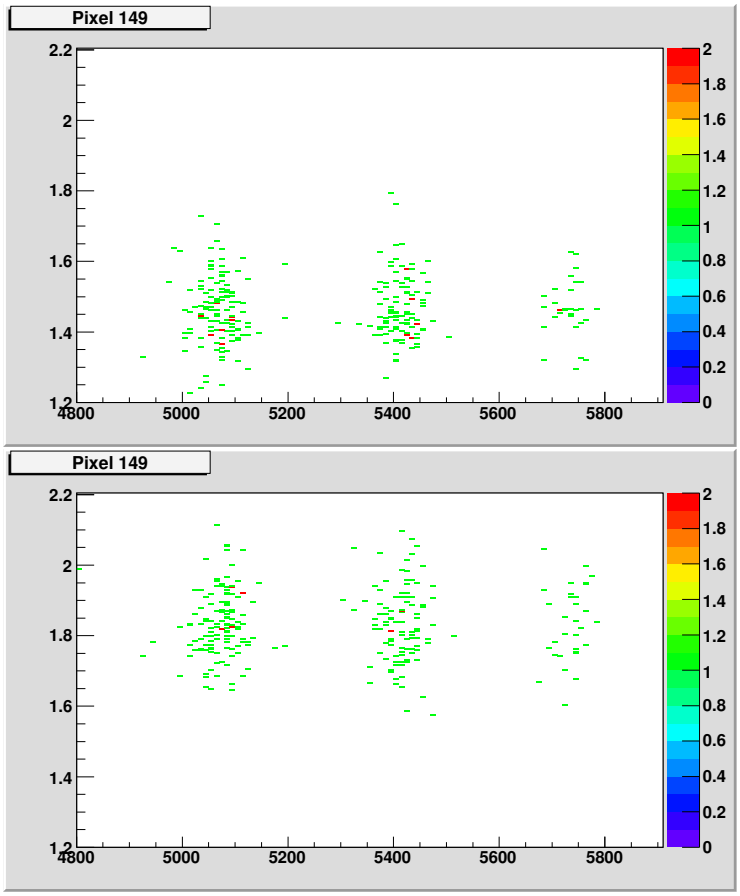

Figure 5.21: *Sigma of the fitted Gaussian functions as a function of energy for p-side (top) and n-side (bottom).*

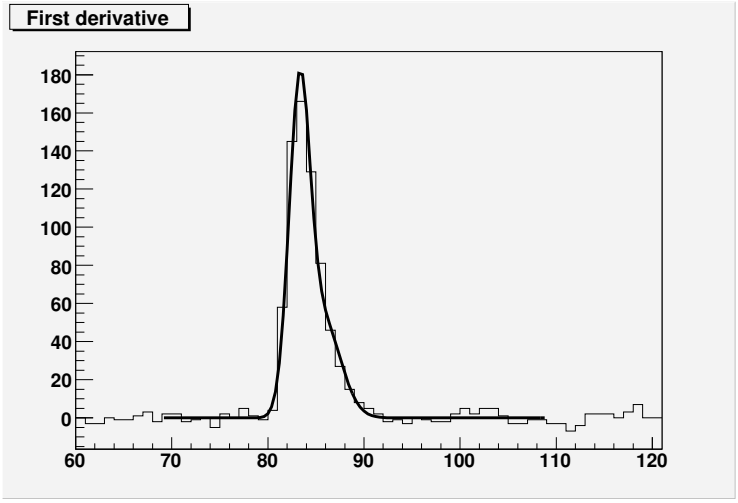

Figure 5.22: *Fitting of a sum of two Gaussian functions to the derivative. The function was fitted over an interval* $[b_{min}, b_{max}] = [b_c\text{-}15, b_c\text{+}25]$ *where* b_c *is the bin with the largest contents.*

the previous fit with just one Gaussian function, the distributions are centered around somewhat lower values, as could be expected from the illustrations of the methods. However, the distributions of the time difference stays approximately the same.

In a first attempt, the width of the left Gaussian function was taken as the width of the derivative. The results are shown in Figure 5.24. For both p-side and n-side, the values are lower then when fitting a single Gaussian (see Figure 5.21). These results are expected since the tail of the derivative is now accommodated in the second Gaussian function, and the left one covers only the peak itself, which has a smaller width. Another noticeable feature is that the distributions from the p-side and the n-side are not as much separated in this case, however, they are still different. The fact that they are less separated than in the case of fitting just one Gaussian function, indicates that only a part of the differences between the traces resides within the first part of the derivative, and that most of it is found in the very last part of the rise time.

The sigma of the second Gaussian function is shown in Figure 5.25. What is surprising is that both distributions are centered at around approximately the same values, which indicates that the width of the second Gaussian in itself does not provide a very good quantification of the risetime, since it is known from previous investigations that the rise time is longer on the n-side. Even more surprising is that the spread is significantly smaller on the n-side than on the p-side, which cannot be easily explained.

Figure 5.26 shows the difference in position between the two Gaussian functions. The difference between these values gives more narrow distributions than any previously tested measure of time. Hence, this may be a quantity that can be used for particle identification, which will be discussed later in this chapter.

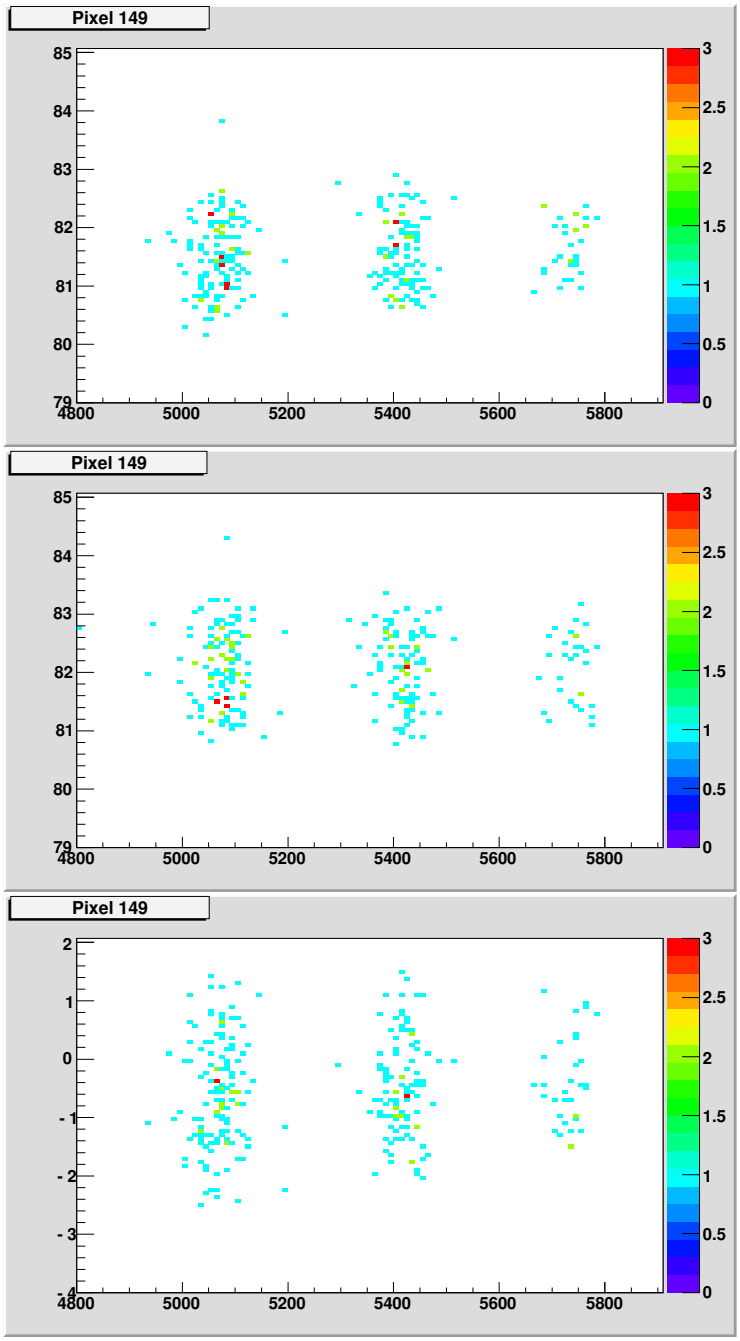

Figure 5.23: *Time as a function of energy for p-side (top), n-side (middle) and the difference in time between the two sides (bottom). The time is taken to be the centroid of the left Gaussian function.*

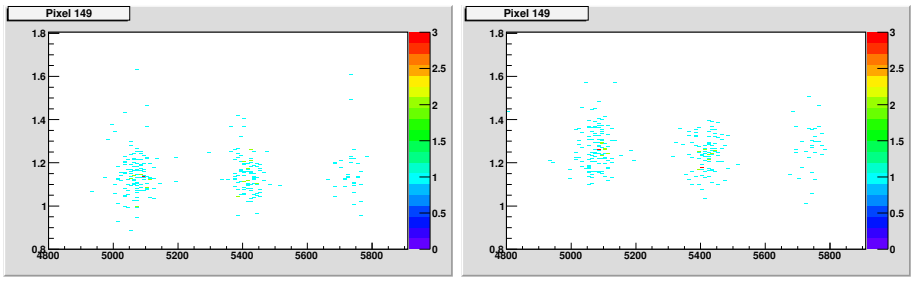

Figure 5.24: *Width of the peak as a function of energy for p-side (left) and n-side (right). The measure of the width is the sigma of the "left" Gaussian function that was fitted to the derivative.*

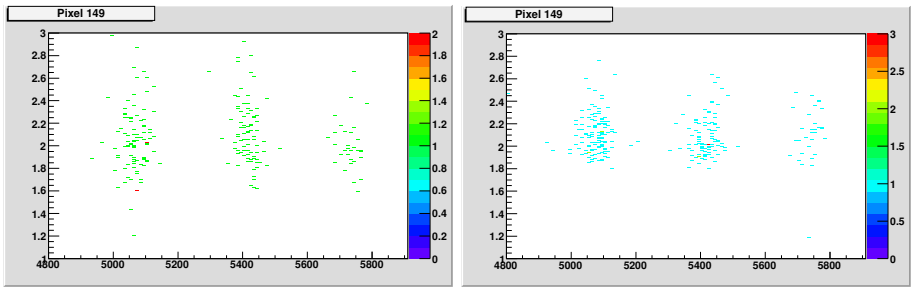

Figure 5.25: *Same as Figure 5.24 but for the sigma of the "right" Gaussian function.*

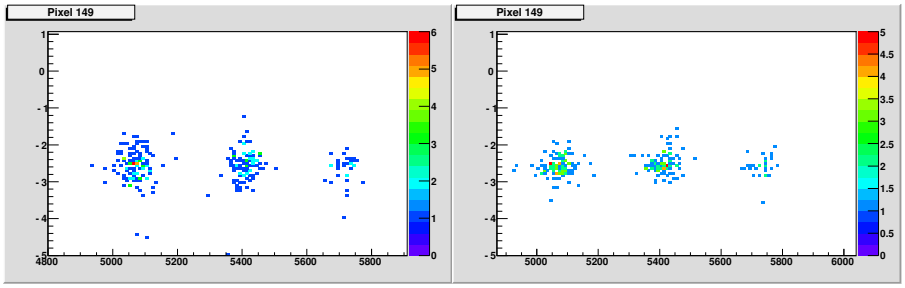

Figure 5.26: *Difference in time between the centroid channels of the two Gaussian functions that were fitted to the derivative, as a function of energy for p-side (left) and n-side (right).*

5.1.5 Integration of peak and tail of derivative

By placing the derivatives of many traces on top of each other, some general features of the pulses could be distinguished. Figure 5.27 shows the derivatives of all the traces from one pixel that has energies in excess of 4 MeV, separated according to whether they originate from the measurement with the α source or from the in-beam measurement.

The region marked with an arrow in the figure indicates a region where the summed derivative from the α particles is clearly separated from the derivative of the (almost exclusively) implanted ions from the in-beam experiment in the pulses from the p-side. On the n-side, no corresponding feature was found. Some single derivatives from the p-side were investigated, and most of them contained the same features as the summed derivative, however not always as pronounced as they are seen for the summed derivatives. In order to quantify this aspect of the derivatives, the derivative was integrated over the region where the large separation between the different kinds of events was seen, and divided by the integral of the peak of the derivative. The two regions to be used were determined individually for each trace by using the maximum bin of the derivative and defining regions with respect to this. The ratio of the two integrals will be referred to as the "tail-to-peak" ratio.

This ratio was calculated for each trace, and the result for the α source measurement is provided in Figure 5.28. The tail-to-peak ratio is shown as a function of energy for both p-side and n-side. The values of the tail-to-peak ratio are similar for the p-side and n-side, however more stable for the n-side. The relative difference between the sides indicates that the spread in the values for the p-side actually does originate from a larger difference between the pulse shapes from the p-side, because if it had been due to solely instability in the method, the same spread would probably have been found on the n-side. A comparison with the results from the same calculations applied to the in-beam data will be presented in the following section where the possibilities of particle identification will be explored.

5.2 Possible particle identification

5.2.1 Raw data from ^{253}No

In order to investigate whether the developed methods for extracting information from the pulse shapes can be used for particle identification, the methods were applied to the in-beam data. The total energy spectra for the p-side and n-side from the in-beam experiment are shown in Figures 5.29 and 5.30. The energy spectra on top show those events that were recorded while the beam was on (5 ms of each cycle), and the bottom spectra show the data from when the beam was off (15 ms of each cycle). Clearly, most events take place during the irradiation of the target. Those events consist of both implanted Nobelium nuclei, background from beam-like and target-like reaction products, and decay products of the radioactive nuclei that have been implanted in the detector.

The peaks in the lower parts of the beam-on spectra (top) are from various low-energy events, such as He atoms from the gas in TASCA being scattered into the detector. The smooth distribution of events over the rest of the energy spectra are from the implanted reaction products. The energy of the nobelium

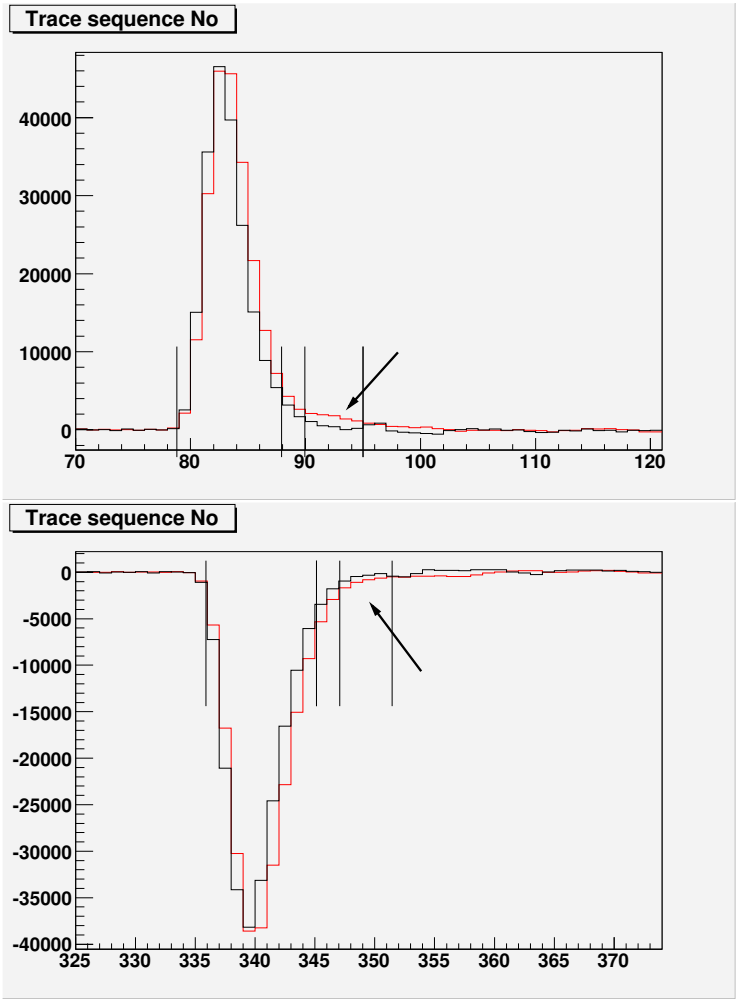

Figure 5.27: *The summed derivatives from all events in one pixel from the p-side (top) and n-side (bottom). The black curves shows the α particles and the red curve shows the data (mainly implanted ions) from the in-beam experiment. The arrow is pointing to a region that differs substantially between different sorts of events on the p-side. The effect is much less pronounced in the n-side. The vertical lines show the approximate limits for the regions that were chosen for the integration of peak and tail, respectively.*

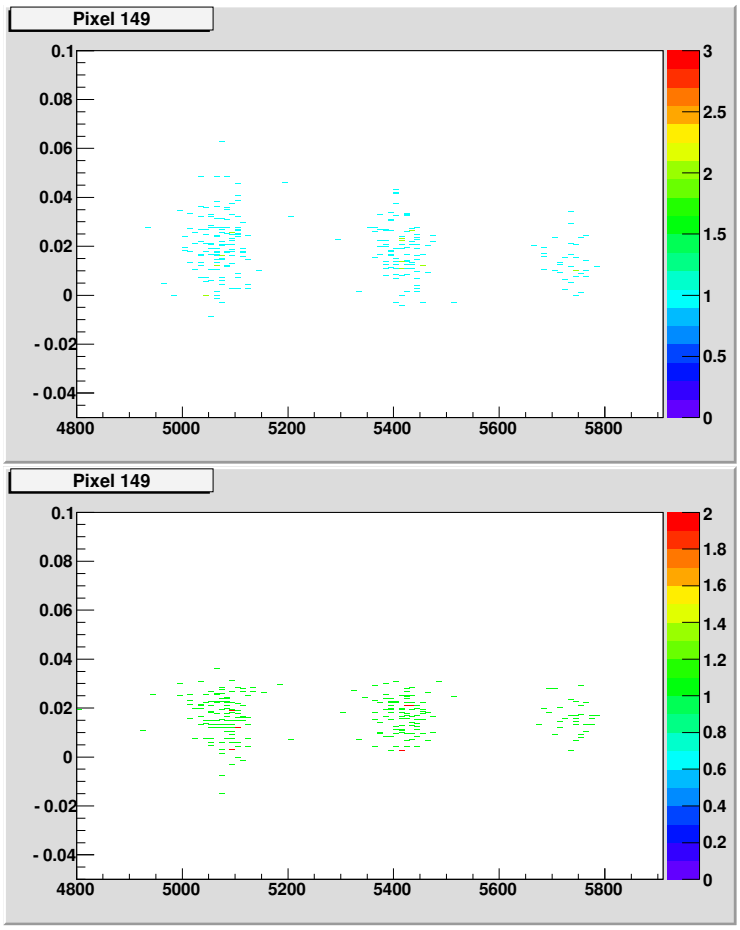

Figure 5.28: *The tail-to-peak ratio as a function of energy for p-side (top) and n-side (bottom). The peak itself is defined as the interval* $[b_{min},b_{max}] = [b_c\text{-}3,b_c+5]$ *and the tail is defined as the interval* $[b_{min},b_{max}] = [b_c+8,b_c+14]$ *where* b_c *is the bin with the largest contents in the derivative of the trace.*

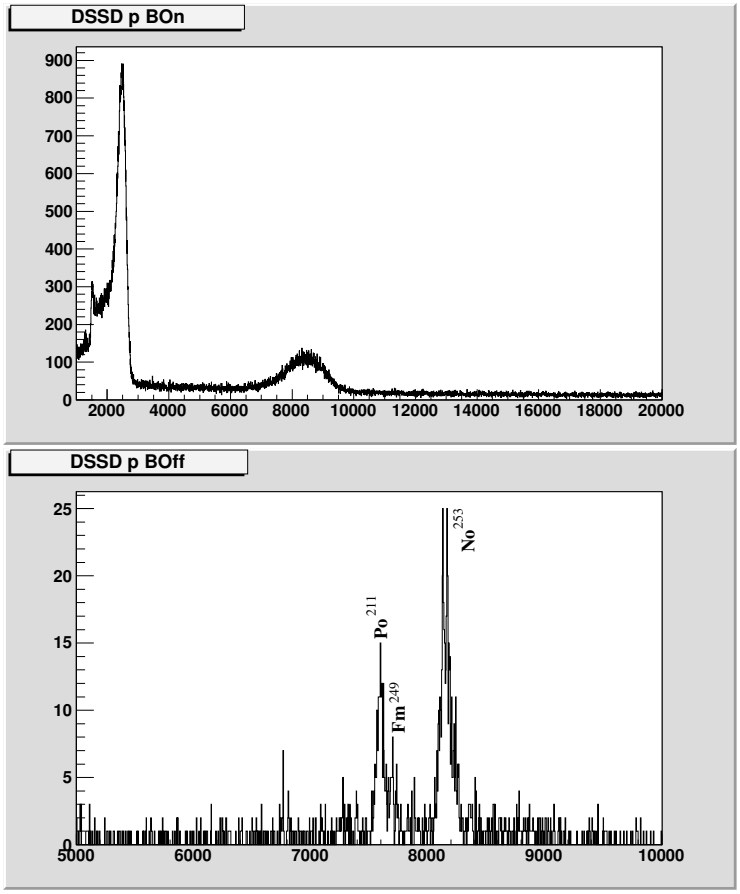

Figure 5.29: *The summed energy spectra from all the strips of the p-side collected during the target irradiation (top) and during the periods when there was no irradiation (bottom).*

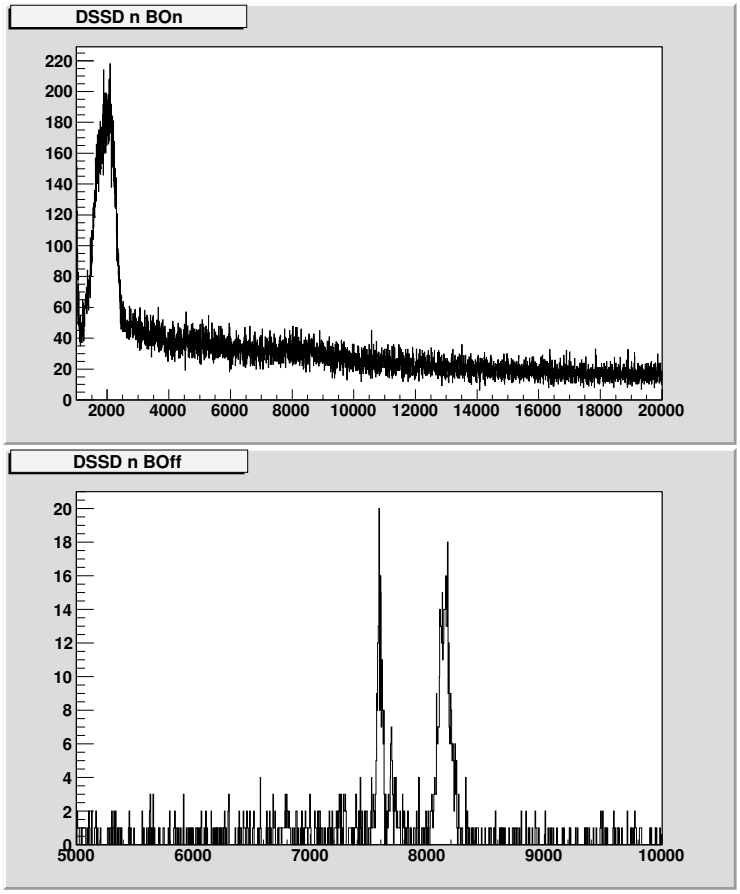

Figure 5.30: *The summed energy spectra from all the strips of the n-side collected during the target irradiation (top) and during the periods when there was no irradiation (bottom).*

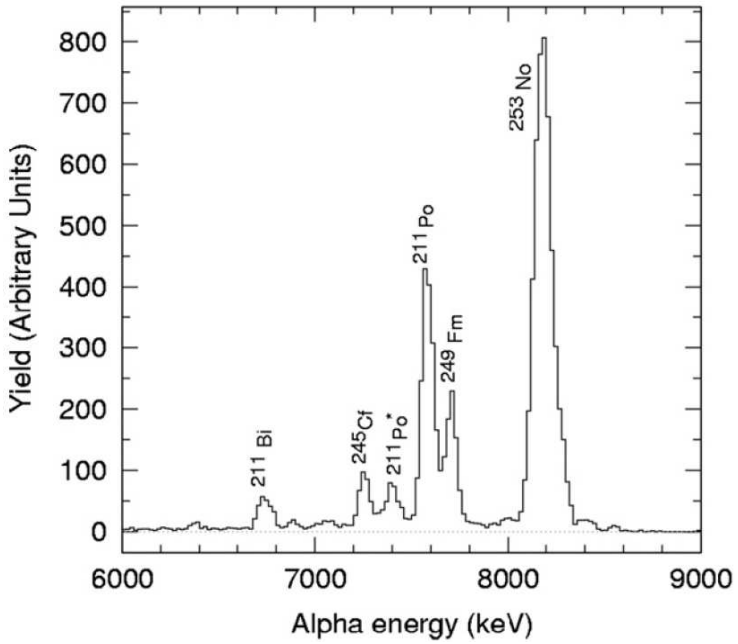

Figure 5.31: *Alpha spectrum recorded using TASISpec under basically the same conditions as in this experiment, but with more statistics. Figure from [17].*

isotopes that are implanted is about 30 MeV but the measured energy is less due to the higher recombination of electron-hole pairs and the different energy loss mechanisms that start to play a large role for heavier particles. These effects cause them to have relatively broad distributions of detected energies. The other reaction products will also be spread out in energy, producing a mostly smooth background. The wide peak around 8 MeV on the p-side originates from three malfunctioning strips, and is not of relevance for the analysis, as those strips are excluded in the detailed analysis.

The spectra from the periods without irradiation of the target are shown in the lower parts of the two figures. Since there are (ideally) no implantations during this period, the only signals are from the decays of the implanted nuclei. On the p-side, the resulting α peaks can be identified by comparing with the spectrum presented in Figure 5.31, which was also recorded using the TASISpec setup but with significantly more statistics. The highest peak is from the α decay of ^{253}No into ^{249}Fm, in which an α particle of energies in the span 8.01 - 8.14 MeV (depending on the state to which is decays) is emitted. The half-life of ^{253}No is approximately 1.6 minutes. The decay of ^{249}Fm into ^{245}Cf with a half-life of 2.6 minutes can also be discerned in the spectrum.

The ^{211}Po that is implanted into the detector and whose α decay can be seen in the spectrum, is created when an α particle is transferred from a beam particle to a target atom and the target atom is knocked out of the target. The kinematics of this reaction makes it possible for the ^{211}Po to reach the detector. This, in combination with the short half-lives ($\sim$30 s for the isomeric state and $\sim$0.5 s for the ground state) makes the peaks from this pollutant relatively

intense.

The overall background in the beam-off spectra consists mainly of irradiation products. These should preferably be sorted into the beam-on spectrum, but the indication on whether the beam is on or off is slightly maladjusted in time, which means that some of the events that happen while the beam is on are wrongly sorted into the beam-off spectrum.

5.2.2 Application of methods to extract slope, time and rise time

Calculation of the linear slope of the trace

The method of fitting a straight line to the middle of the rise of each trace was applied to the in-beam data. The results from one pixel are shown in Figure 5.32. The upper part shows the distributions as functions of energy. These spectra can be compared to the spectra in Figure 5.5, which shows the results of the same calculation being applied to the data from the α source. The spectra show similar features; the energy dependences of the slopes are similar and the spread in the values from the p-side is larger than the spread in the data from the n-side in both cases.

The middle and lower set of figures show the slope normalised with energy, for three different energy regions. The left part of the figures show the beam-on data, which consists mainly of implanted ions. From this figure, the conclusion that there is no pronounced difference between different energy regions can be made. This allows for a direct comparison between the spectra from the different types of particles. The figures shown here are analogous to those in Figure 5.6 for the α data. The distributions from the in-beam data and the α particles are, to a large extent, overlapping. There could be a slight shift towards lower numbers on the p-side and towards higher numbers on the n-side when going from the α data to the implanted ions, but this effect is very small and does not allow for an identification if the particles.

This is confirmed by a comparison between the beam-on data (left) and the beam-off data (right). Only three events are seen in the beam-off spectra in an energy region ranging from 6.5 MeV to 8.5 MeV (only these are displayed in the figure). Those events most likely arise from the α decays of implanted ions. The energies of the three particles are approximately 6.8 MeV, 7.5 MeV and 8.2 MeV, respectively. A comparison with Figure 5.31 shows that they originate from regions where α particles are expected, which gives a strong indication on that they are likely α particles. Two more particles were detected during the beam-off period, but they had energies that were very high, which implies that they are implants that were wrongly labeled. These particles are not displayed in the figure.

If successful particle identification could be made using the described method, the likely α particles from the beam-off periods would exhibit values for the slope that would be outside the distributions achieved by analysing the implants. As seen in Figure 5.6, the three α events are not separable from the rest of the distributions.

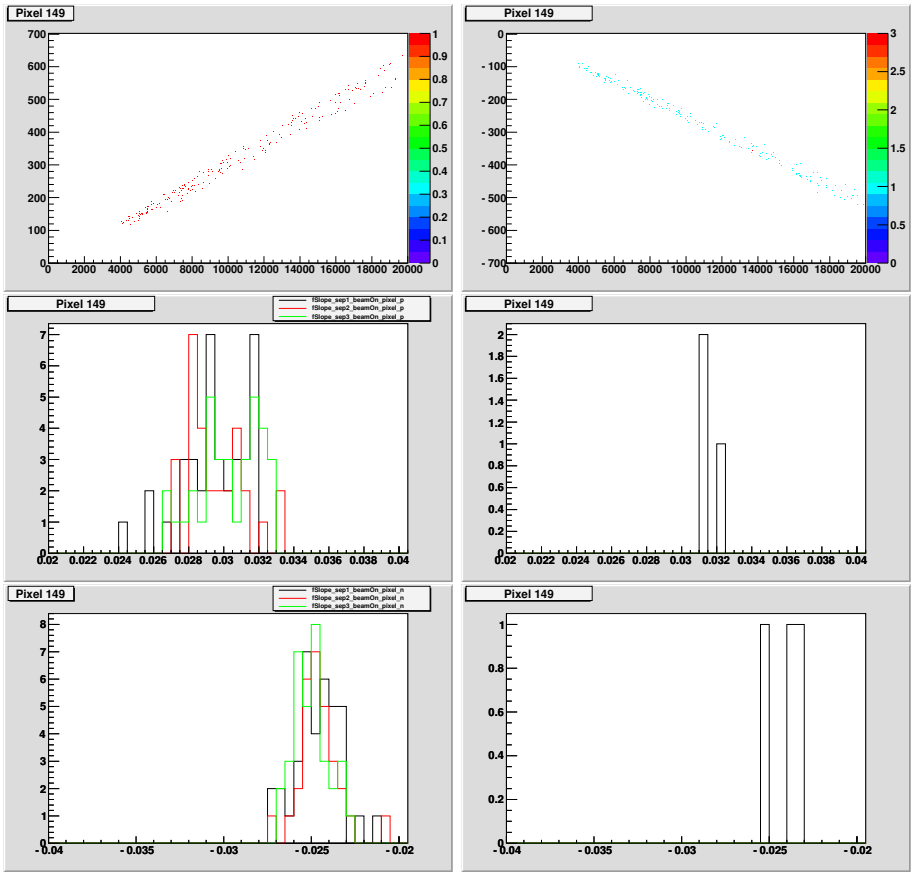

Figure 5.32: *Linear slope for the in-beam experiment. Top: The slope as a function of energy for p-side (left) and n-side (right) for the beam-on data from one pixel. Middle: The distribution of slopes (normalised with the energy of each event) divided into different energy regions for the p-side for beam on (left) and beam off (right). The energy regions are such that the first (black) is from 6.5 to 8.5 MeV, the second is from 5.0 to 6.5 MeV (red) and the last one is from 8.5 to 10 MeV (green). Bottom: Same as previous, but for the n-side of the detector. The three events displayed in the right part of the figures are likely α decays from a decay chain of ^{253}No.*

Calculation of time as average bin of derivative

The calculation in which the time was determined as the average of the derivative in a span ranging from bin number 65 to bin number 100 was applied to the in-beam data, and the result is shown in Figure 5.33. The energy span of the spectra cover both the same region where the α peaks from the source end up, and the region in which the decays of ^{253}No are found. The distributions should be compared to those in Figure 5.13, which are from the α source. For the p-side, the distribution is more narrow for the in-beam data than for the α data. However, the lower limits for the distributions are very similar so they still overlap. Also the difference in time between the p-side and n-side look the same as for the α data.

One feature of the in-beam data seen in the time distributions is the energy dependence. As seen in the figure, the times are, on average, slightly higher for the events with high energies. Since it is possible to apply a cut in the data that is energy dependent, an energy dependence could be used in order to get the best separation into different events. However, it can be deduced from a comparison of the figures form the different sorts of events that it does not help in this case; the distribution from the α particles, with energies in the very left part of the spectrum from the implants that is displayed in the figure, overlap with that of the implants also in the part of the spectrum that represent their energies.

A comparison with the beam-off particles, it turns out that two of them (the ones with highest and lowest energy of those displayed) are actually clearly separated from the distributions from the beam-on data, especially when comparing their values to the distribution at the relevant energy. However, they are also separated from the distributions from the α source, which is odd. It is also so that the particle with the intermediate energy ends up in the middle of the distributions of the implants, which implies that the method is not reliable for particle identification.

Fitting of a Gaussian function to the derivative

The method described in section 5.1.3, in which a Gaussian function was fitted to the derivative of each trace, was applied to the in-beam data. The results are shown in Figures 5.34 and 5.35. Starting from the beam-on data, the distributions of the time (Figure 5.34) can be compared to the times from the α source (Figure 5.20). The figures show the time that was extracted as the centroid of the Gaussian function as a function of energy. A comparison between the beam-on measurement and the data from the α source (see Figure 5.20) shows that the distributions are positioned in the same regions. For the p-side, the calculated times are between 81 and 83 for both cases, and for the n-side the corresponding numbers are 82 to 84. The distributions of time differences between the p- and n-side for each event seem to be somewhat smaller in the case of the in-beam data, but the distributions are centered around the same values, which makes it impossible to make any conclusion of particle type from the time difference between p- and n-side.

The right part of the figure shows the beam-off data, which confirms that there is no distinct difference between the timing of α particles and implanted ions. In all three cases (time for p-side, time for n-side and time difference

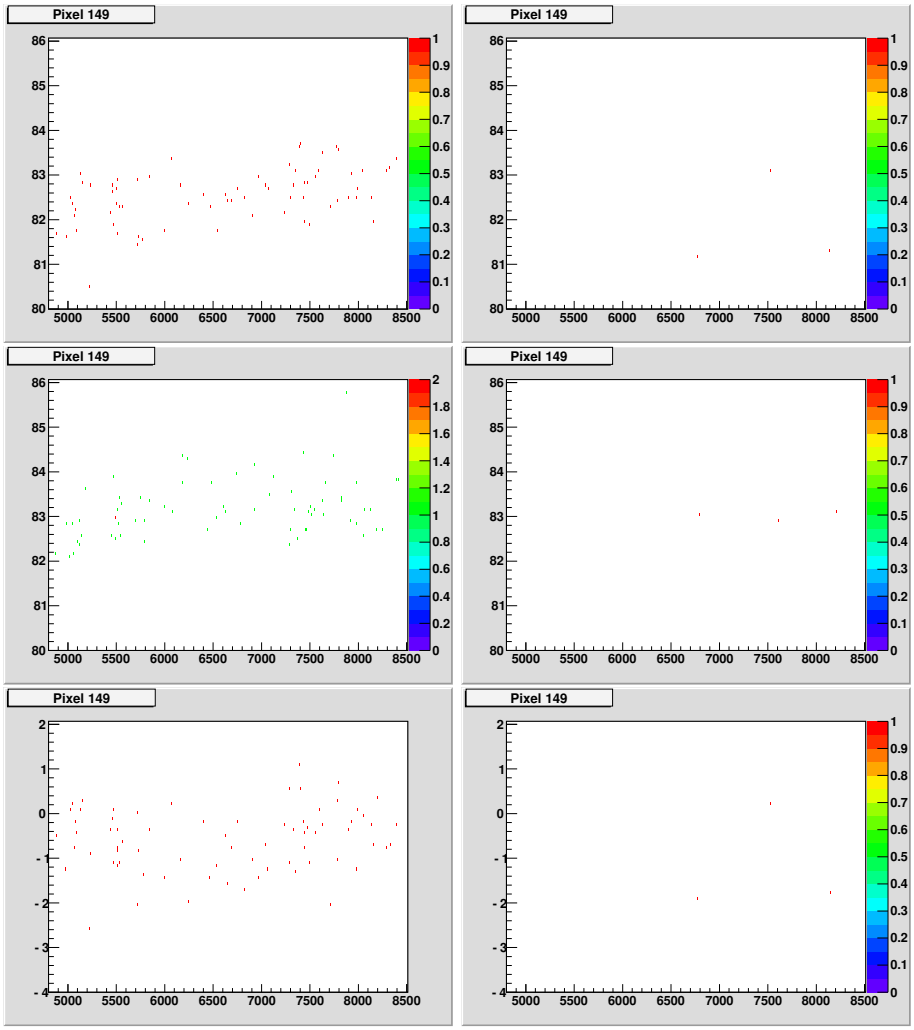

Figure 5.33: *The time as a function of energy for the in-beam data. The time is calculated as the average bin in an interval from 65 to 100. The upper spectra show the time for the p-side separated into beam-on (left) and beam-off (right). The middle spectra show the same data for the n-side, and the bottom spectra show the difference in time between those.*

between those), the particles that are detected during the beam-off periods, that are most likely from an α decay chain, are positioned such that they are spread out over the entire span of values from the implantation data.

The widths of the fitted Gaussian functions are shown in Figure 5.35. The widths and positions of the distributions from the beam-on data (left) can be compared to Figure 5.21, which shows the corresponding features of the α source. The distributions from the in-beam data seem to be somewhat more narrow than the ones from the α source, both in the case of the p-side and n-side. However, also in this case, the distributions are centered around the same value, and no distinct separation can be made.

Considering the α particles in the beam-off data (shown in the right part of the figure), their values for the width of the Gaussian function do not differ from the values achieved from the beam-on data, which indicates that no particle identification is possible from the procedure of fitting a Gaussian function to the derivative and considering the two parameters position and width.

Fitting of two Gaussian functions to the derivative

The method of fitting two Gaussian functions to the derivative was also applied to the in-beam data. The distributions of times for the left Gaussian function, the time difference between the p- and the n-side, and the sigmas of the functions turned out to be more or less the same as the the ones for the α sources. In some cases either particle type gave distributions that were somewhat smaller than the other, and in some cases the overlap was not complete, but the overall impression was a large similarity between the distributions from the different particles, just as was seen for the parameters of the fitting of one Gaussian function only. For some parameters, an energy dependence could be seen, but this did not allow for a better separation of the distributions. Also, the few likely α particles during the beam-off period could not be unambiguously separated from the distributions from implanted ions. In some cases, two of the three particles were outside the main distributions from the implants, but there was always one that could not be separated from the implants. If it had always been the same particle, it could have been a reason for claiming that maybe it is not an α particle after all, but it was not always the same particle that fell within the main region from the implants.

In section 5.1.4, where the method was described, it was noted that the difference in time between the centroid channel of the two Gaussian functions gave rather narrow distributions. Also this parameter was investigated for the in-beam data, but although the distributions are narrow, they still overlap. This time difference is shown in Figure 5.36 for the p-side. The distribution stays rather narrow also in the case of the in-beam data. However, the distribution overlaps completely with the one from the α particles (see Figure 5.26). Also, the α particles in the spectrum to the right are also accommodated in the same region. Another attempt in which the time difference between the two centroid values was weighted with the heights and widths of the two functions was tried as well, but this also gave overlapping distributions.

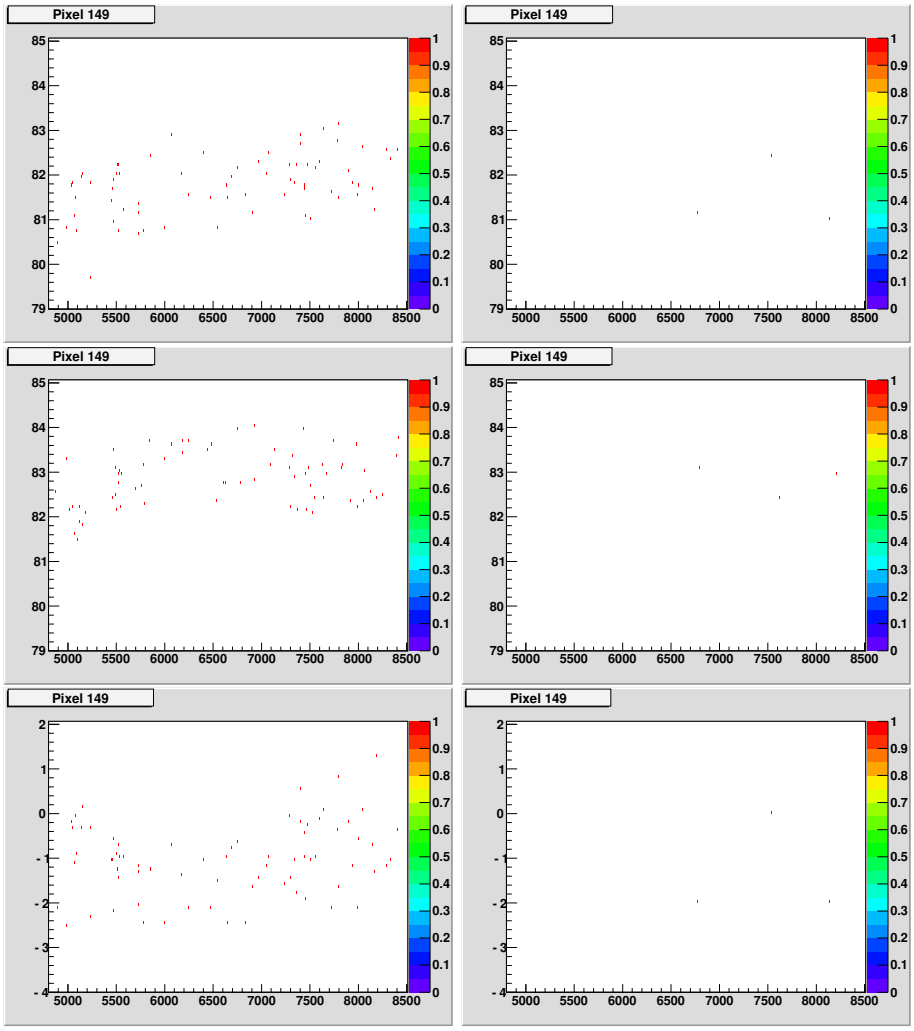

Figure 5.34: *Time as a function of energy for the in-beam data, separated into beam-on and beam-off. The value for the time is the centroid of a Gaussian function that was fitted to the derivative of each trace. The beam-on spectra are in the left column, and the beam-off spectra are in the right column. The p-side is shown in the top spectra, the n-side in the middle spectra and the difference between those are shown in the bottom spectra. Note that the scale on the y-axis is the same as for the corresponding spectra from the α particles (Figure 5.20), so that a direct comparison can be made.*

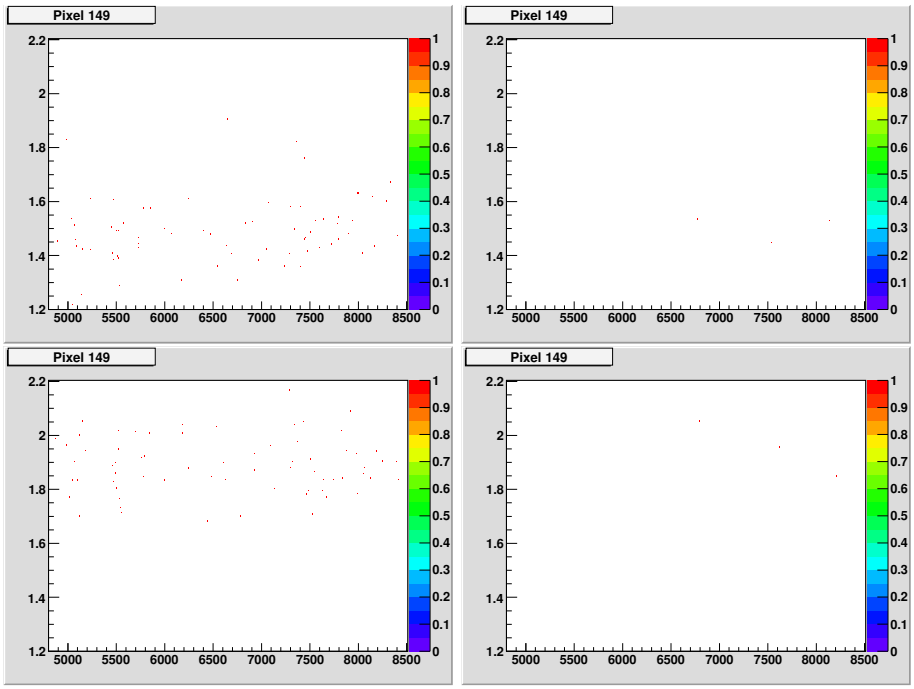

Figure 5.35: *The width of the derivative as a function of energy for the in-beam data, separated into beam-on (left) and beam-off (right). The width is extracted as the sigma of a Gaussian function that was fitted to the derivative of each trace. The top spectra shown the data from the p-side while the bottom spectra show data from the n-side. Note that the scale on the y-axis is the same as for the corresponding spectra from the α particles (Figure 5.21), so that a direct comparison can be made.*

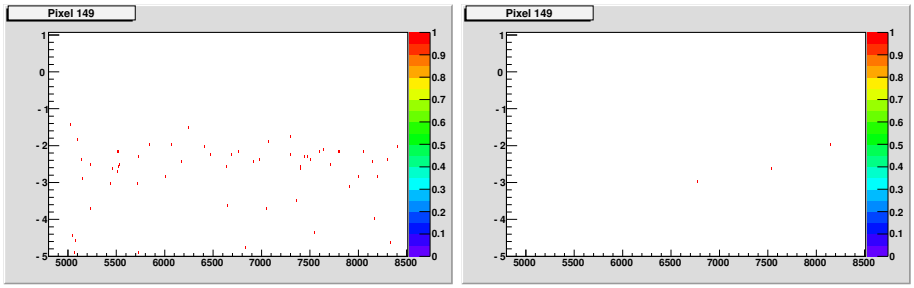

Figure 5.36: *The difference between the centroid channel of the two Gaussian functions whose sum was fitted to the derivative, as a function of energy. The data originated from the p-side of the detector. The data from the beam-on periods is shown in the left spectrum and the data from the beam-off periods is shown in the right spectrum.*

Tail-to-peak ratio of the derivative

The tail-to-peak ratio, which was defined in section 5.1.5, was calculated for the in-beam data. This ratio, as a function if energy, is shown in Figure 5.37. For the n-side, the tail-to-peak ratios from the α source (see Figure 5.28) overlap with the ones from the implanted ions to a large extent. The main fraction of the α particles have a tail-to-peak ratio in the region that reaches from 0 to 0.025, and the implants are distributed mainly from 0 to 0.040. Therefore, the tail-to-peak ratio from the n-side will not be considered further.

The tail-to-peak ratio from the p-side is more interesting: The α particles are distributed in a region reaching from 0 to 0.04, whereas the implanted ions are distributed mainly from 0.025 to 0.06. This indicates that there is a difference between different particles in terms of the tail-to-peak ratio, that can maybe be exploited for particle identification. Even though the different distributions are not completely separated, it may be possible to use the tail-to-peak ratio either as a first step to identify particles or as a method to refine the data from the beam-on periods to contain not exclusively, but mainly, α decays.

In order to get a better view of the available data, the distributions of the tail-to-peak ratio for all events with energy in excess of 4 MeV for both the α source and the in-beam data was plotted, as shown in Figure 5.38. The α data is shown in red and the in-beam data is in black. The distributions are distinctly different; the α particles have, in general, lower values than the in-beam data, as was expected (see Figure 5.27). They do not separate completely, but a limit of around 0.033 can be set as a first, preliminary separation of the two distributions.

The lower part of the figure shows the tail-to-peak ratio from the particles in the beam-off periods. The three leftmost particles are the ones that are most likely α particles, while the other two are probably mislabeled particles from the beam-on periods. If the limit between the two distributions is set at 0.033, all three particles will be within the "α region", whereas the two particles that are implanted ions will be sorted into the other category. This indicates that it may be possible to separate the in-beam data into α particles and implanted ions based on this ratio. It should be noted that the calculation of the tail-to-peak ratio is a quantity that can be easily calculated, and that this calculation could relatively easily be implemented in the FPGA of a sampling ADC.

One aspect of the tail-to-peak ratio that could be used in order to improve the method, is the energy dependence of the ratio. As seen in Figure 5.28, the ratio seems to drop somewhat for higher energies. This indicates that it could be possible to define a better limit for separating the particles. For higher energies, the separation limit can maybe be set to a lower value than for lower energies. However, the likely α particles from the in-beam data do not follow the expectations - although they have energies higher than the ones from the α source, they have tail-to-peak ratios on the upper limit of fitting into the distribution from the α particles. Therefore, a change of the limit would not give a better result in this particular case. A further development of the method should take into account a larger number of events for the determination of a suitable limit between the distributions, and possibly the best separation is achieved using an energy dependent limit. For the current analysis, such an energy dependence will not be considered further.

The current method which has been discussed for particle identification was

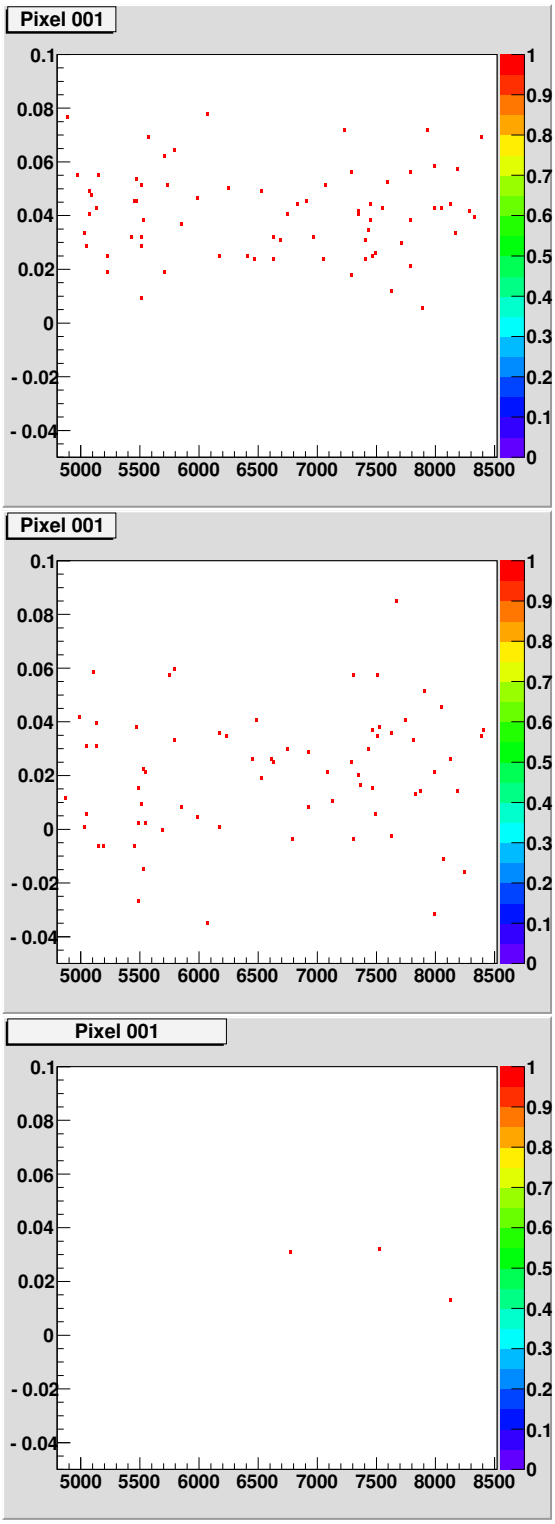

Figure 5.37: *Tail-to-peak ratio as a function of energy for the in-beam run during the time the beam was on for p-side (top) and n-side (bottom), and from when the beam was off for the p-side (bottom). The data is from the same pixel as was used for the previous pictures.*

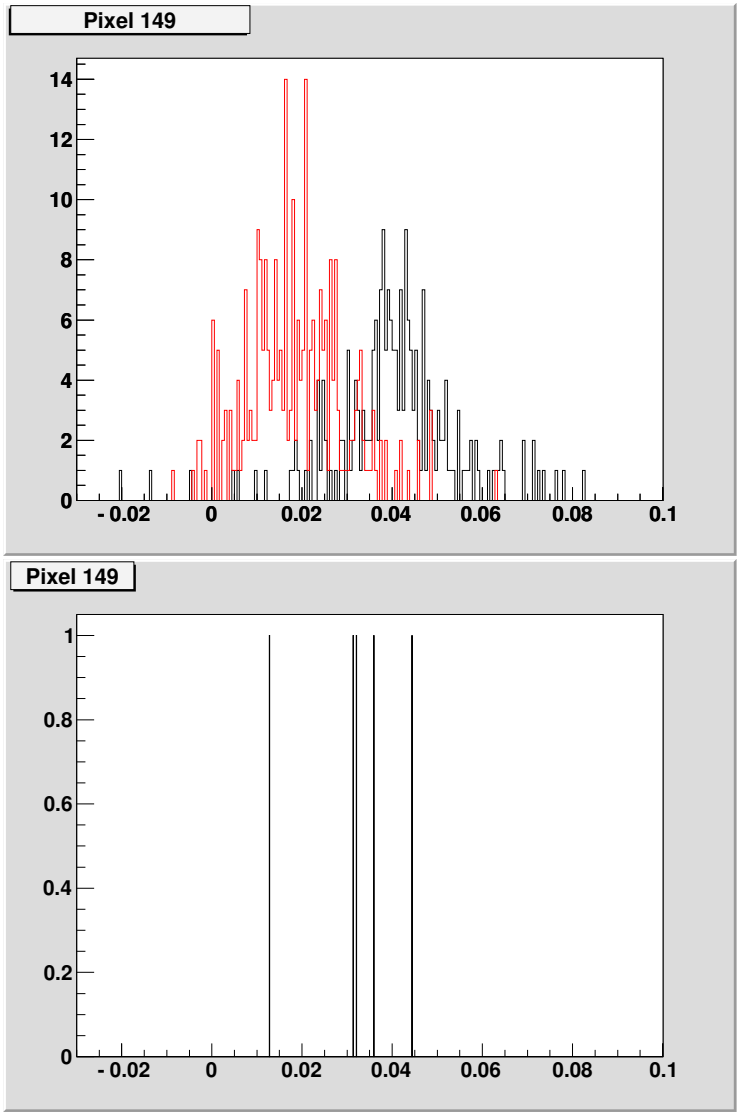

Figure 5.38: *Top: The distributions of the tail-to-peak ratio from the alpha source (red) and from the beam-on data from the in-beam run. The events displayed are those with multiplicity equal to 1 in both sides and that have energies in excess of 4 MeV in both sides. Bottom: The tail-to-peak ratio of the 5 events found during the beam-off periods of the in-beam run. The three events furthest to the left are most likely α particles, while the other two are particles that arrived while the beam was on but were labeled wrongly. Note that the data originates from one pixel only.*

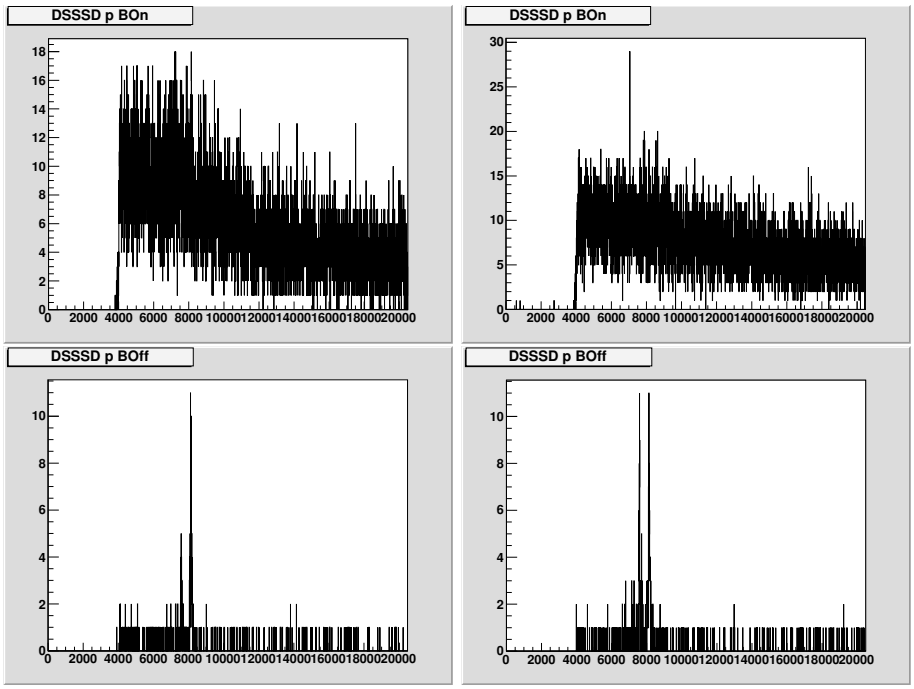

Figure 5.39: *The in-beam data from the entire p-side of the detector separated into beam-on (top) and beam-off (bottom) and according to whether the tail-to-peak ratio is over 0.033 (left), which should imply that the particles are implanted ions, or if the ratio is below 0.033 (right), which should imply that the particles are α:s.*

applied to the in-beam data in order to see if particle identification can be achieved by applying the condition that α particles should have tail-to-peak ratios of below 0.033 and implants should have values that are above 0.033 to all the data from the in-beam run. The resulting separated spectra from the beam-on and beam-off periods are shown in Figure 5.39. In the ideal case, the upper figure which contains the beam-on data, should now be separated into implanted ions (in the left part of the figure) and α particles (in the right part of the figure). However, there are approximately as many counts in both spectra, and the peaks from the α decays are not visible in either of the spectra. If the separation had worked, there would be clear peaks in the spectra to the right. The lower part of the figure, showing the beam-off data, also indicates that the separation is not working properly; if it had, then the right spectra would be considerably cleaner because the particles that were wrongly labeled should be removed from the α spectrum. At the same time, the peaks in the left spectrum should disappear as no α particles should be left in that spectrum. This first version of the particle identification obviously did not succeed.

An obvious development of the method is to carefully test and optimise the parameters used in the calculation. It might well be so, that the region over which the tail is integrated is not optimal. Another aspect, which could be very important, is regional variations between the different pixels. This first

version of a particle identification method was developed using the data from one pixel only. Possibly, the methods needs to be customised for each pixel, for instance by applying a different separation limit for different pixels. A short investigation of this aspect showed that there is indeed a difference between the different pixels that needs to be carefully studied.

Although more complicated, it is certainly feasible to apply different limits to the data from different pixels. If the regions over which the different parts of the pulse are integrated need to be optimised for each pixel in order to achieve particle identification, it would give a difficult situation as the data needs to be processed in each channel separately on the sampling ADCs, and before it is known what pixel the event originates from. However, such modifications are probably possible to apply on a strip-to-strip basis, which means that as long as the same regions work for each strip, the method can still be implemented.

In order to get a functioning particle identification, the algorithm must be developed further. It is not obvious from the study that it is possible to achieve particle identification in the TASISpec DSSSD using the available electronics, but the clearly different distributions in Figure 5.38 prove the point of particle information being present in the rise of the pulse.

Chapter 6

Summary and Outlook

The analysis of the present data has shown that the same energy resolution can be reached using sampling ADCs and standard electronics. The last version of the offline filter, which uses curves that are fitted to both baseline and exponential slope, gave a resolution comparable to that of standard electronics. It was also possible to make an averaging of the traces before the fitting was made, with an unchanged resolution.

The MWD algorithm, that was applied to the artificially concatenated traces, also gave a resolution comparable to standard electronics. The different tests that were made showed clearly that the parameters need to be carefully optimised. Possibly, a better resolution can be achieved by fine tuning the parameters, but the similarity between the last version of the offline filter and the MWD algorithm implies that the resolutions of these two methods should be rather similar. This is also the case for the current versions and parameter settings. In turn, this implies that the resolution that can be achieved from the available data can probably not be improved very much further.

The data at hand is, however, strongly limited in the sense that only a small fraction of the exponential tail of each event was recorded. When operating on the real data stream, where a longer fraction of the tail can be considered in the energy determination, the resolution can possibly be improved further.

From this experiment, it can be concluded that the standard electronics that handle the data from the DSSSD can be exchanged with sampling ADCs without any loss of energy resolution, but the question of whether the resolution can even be improved using the new electronics or not, remains.

A future experiment, which is needed in order to resolve this question, is to do new measurements where a larger period of the tail is kept. The modules can be easily configured to read out longer traces than were made in this experiment. The cost of this will only be longer read-out times and that storing of the data will be more space consuming. The developed offline energy extraction code can be applied more or less directly to the data, and this should give an immediate answer to the question. The MWD algorithm needs fine tuning before it can be applied to the data, as the parameters have to be optimised in order to take full advantage of the longer traces, but this only means small adjustments to the current LabVIEW code. Such an experiment can be easily done in the detector laboratory using a radioactive source, and should not comprise very many days of work.

A subsequent step in order to make the transition from standard electronics to sampling ADCs in the TASISpec setup, is to program the FPGA on the sampling ADC so that the MWD algorithm can be done already on the ADC. Of course it is possible to read out the entire pulse shape as was done for this experiment, but this gives large amounts of data and longer dead times for the system. In principle, it has been shown in this work that it is possible to average the data already before the fitting of the functions is made, which could be used for decreasing the amount of data that is needed to store for the energy determination, but still it will be more advantageous in a future data acquisition system to minimize the amount of data further by doing the processing directly on the sampling ADC. The programming of the FPGA can still be done only with support from the company CAEN, which manufactures the available modules, which makes this part of the project a somewhat more complicated process that cannot be done at any time.

The attempts to characterise the rise of the pulse in order to pave the way for particle identification, were only partly successful. The characterisation of the rise by fitting a straight line to the slope showed that it is indeed possible to fit a linear function to the slope around the center of the peak of the derivative and get a reasonably stable algorithm. However, when the same method was applied to the in-beam data, the distributions from the α particles and the in-beam data overlapped, which implies that no information of particle type is present in the slope of the rise.

Several other methods were tried as well, such as calculating the time of the arrival of the pulse as the average bin of the derivative and fitting Gaussian functions to the derivative, but none of these methods gave distinctly different distributions for the different particle types.

The most successful attempt of particle identification was to integrate a certain part of the "tail" of the derivative of the trace, and divide by the integral of the main part of the derivative. For the data that was investigated, the distributions of this ratio were distinctly different for α particles and implanted ions, however not completely different. It is possible that the ratio between different parts of the derivative of the traces can be used for a particle identification algorithm, but the regions to use for optimal separation of the distributions must be optimised. Also, there are indications on local variations between different pixels. This issue needs to be properly addressed as well.

The experiment has shown that there is indeed information about particle type in the pulses, that can be used in an identification process. However, it is not obvious that it will be possible to construct a sufficiently good algorithm. A particle identification system using TASISpec and the available electronics needs more work before completion.

Bibliography

[1] Yu. Ts. Oganessian. Heaviest nuclei from ^{48}Ca-induced reactions. *J. Phys.*, **G34**:165, 2007.

[2] Yu. Ts. Oganessian *et al.* Synthesis of a new element with atomic number Z = 117. *Phys. Rev. Lett.*, **104**:142502, 2010.

[3] R.-D. Herzberg and P. T. Greenlees. In-beam and decay spectroscopy of transfermium nuclei. *Prog. Part. Nucl. Phys.*, **61**:674, 2008.

[4] K. Hauschild *et al.* GABRIELA: A new detector array for γ-ray and conversion electron spectroscopy of transfermium elements. *Nucl. Instr. Meth.*, **A560**:388, 2006.

[5] R. D. Page *et al.* The GREAT spectrometer. *Nucl. Instr. Meth.*, **B204**:634, 2003.

[6] G. Pausch *et al.* Particle identification in solid-state detectors by exploiting pulse shape information. *Nucl. Instr. Meth.*, **A322**:43, 1992.

[7] M. Mutterer *et al.* Particle identification with time-of-flight and pulse-shape discrimination in neutron-transmutation-doped silicon detectors. *Nucl. Instr. Meth.*, **A608**:275, 2009.

[8] G. Pausch *et al.* Limitations of the pulse-shape technique for particle discrimination in planar Si detectors. *IEEE Transactions on Nuclear Science*, **44**:1040, 1997.

[9] W. R. Leo. *Techniques for Nuclear and Particle Physics Experiments.* Springer-Verlag, 1994.

[10] G. F. Knoll. *Radiation Detection and Measurement.* John Wiley & Sons, Inc., 2000.

[11] G. Pausch *et al.* Particle identification in solid-state detectors by means of pulse-shape analysis - results of computer simulations. *Nucl. Instr. Meth.*, **A337**:573, 1994.

[12] Henning Schaffner GSI. private communication, 2010.

[13] www.caen.it, 2010.

[14] V. T. Jordanov and G. F. Knoll. Digital synthesis of pulse shapes in real time for high resolution radiation spectroscopy. *Nucl. Instr. Meth.*, **A345**:337, 1994.

[15] J. Eberth et al. Encapsulated Ge detectors: development and first tests. *Nucl. Instr. Meth.*, **A369**:135–140, 1995.

[16] G. Duchene *et al.* The Clover: a new generation of composite Ge detectors. *Nucl. Instr. Meth.*, **A432**:90, 1999.

[17] L.-L. Andersson *et al.* TASISpec - a highly efficient multi-coincidence spectrometer for nuclear structure investigations of the heaviest nuclei. *Nucl. Instr. Meth.*, **A622**:164, 2010.

[18] www.mesytec.com, 2010.

[19] A. Semchenkov *et al.* The TransActinide Separator and Chemistry Apparatus (TASCA) at GSI - optimization of ion-optical structures and magnet designs. *Nucl. Instr. Meth.*, **B266**:4153, 2008.

[20] K. E. Gregorich *et al.* Attempt to confirm super-heavy element production in the $Ca48 + U238$ reaction. *Phys. Rev. C*, **72**:014605, 2005.